Fabrication, Characterization and Performance of 3D-Printed Sandstone Models

by

Kevin Hodder

A thesis submitted in partial fulfillment of the requirements for the degree of

Doctor of Philosophy

in

Materials Engineering

Department of Chemical and Materials Engineering
University of Alberta

Abstract

Due to the natural heterogeneity of rock there exists a large variance between samples in geomechanical engineering testing. Additionally, the number of samples available for testing that meet the screening requirements for grain size, mineralogy, bedding orientation and moisture content can reduce the number of samples even further. Specifically, the unconfined compressive strength (UCS) and Young's modulus, E, can vary considerably, making the repeatability of geomechanical experimental work questionable.

3D-printed model sandstone has been shown to be a viable prospect in minimizing the variance between geomechanical laboratory samples by providing a method of fabricating multiple samples with similar mechanical properties. However, although the macroscopic mechanical properties have been studied, the micromechanical properties governing the macroscopic behavior of 3D-printed sandstone is relatively unknown. Through a research paradigm encompassing processing, structure, properties and performance, 3D-printed sandstone was characterized on a microstructural level and the results reported herein.

3D-printed sandstone was compared and contrasted to Berea sandstone via ultra-violet (UV) fluorescence microscopy where it was found that 3D-printed sandstone contains higher porosity and a two phase organic/inorganic particle coupling that is unlike the crystallized bonds of natural sandstone. Due to the porosity of the samples and the binder jetting technique used to fabricate 3D-printed sandstone, a binder volume fraction limit was discovered via a thermogravimetric technique and a dimensional control study. It was found that samples containing more than 8 vol. % of binder were subject to bleeding through capillary action and pooling through gravity.

Through determination of the binder volume fraction limit, the UCS of 3D-printed sandstone was increased by 77 % without any apparent loss of dimensional stability. Additionally, an innovative use of silane coupling agents (SCA) is described that provides a novel prospect of further increasing the UCS of 3D-printed sandstone.

The results of a combination of atomic force microscopy (AFM) and nanoindentation techniques are described that present the Young's modulus of the 3D-printed binder between sand grains, which may be used as a vital parameter in finite element analysis (FEA) modelling of geomaterials. As far as the author knows, the quantification of a micromechanical property between the particles of a geomaterial, although 3D-printed, is a novel prospect. Through quantification of the micromechanical properties of geomaterials, new opportunities for increasing the accuracy of FEA simulations and decreasing the burden on sampling from natural formations may be achieved.

By using the information gathered from the processing, structure, property and performance-related studies described herein, the performance in UCS and Young's Modulus of 3D-printed sandstone was improved and the micromechanical property relationships between binder volume fraction and macroscopic properties is presented.

Preface

Some of the research contained with this thesis contains portions from a manuscript entitled "Process Limitations of 3D Printing Model Rock" that has been accepted for publication in Progress in Additive Manufacturing as of September 1, 2017. The manuscript was co-authored by Dr. John Nychka and Dr. Rick Chalaturnyk, who aided in the concept formation and manuscript composition. The publication contains my original experimental work of Chapter 3, specifically Sections 3.2, 3.3 as well as the results of Chapter 4, Sections 4.1 – 4.3 and 4.6.

Sections 2.2.1 – 2.2.7 are from a term paper submitted for credit on April 14, 2016 titled "A Review on Furfuryl Alcohol Polymerization" in CME 694 at the University of Alberta, instructed by Dr. João Soares.

Dedication

This work is dedicated to Joel, Jeanette, Ashley, Dawn and Larysa.

Thank you for everything.

Acknowledgements

First and foremost I would like to acknowledge my supervisor, Dr. John Nychka, for which this project would have a vastly different outcome without his guidance and expertise. His patience, kindness and calm demeanor contributed greatly to the success of this thesis. I am fortunate to have had the opportunity to learn alongside such a great teacher.

I am also appreciative to have worked alongside another great leader, Dr. Rick Chalaturnyk. His innovation, intelligence and unwavering support has helped me forge my own path during this study and the amount of freedom he has provided cannot be thanked enough.

Next, this project would not have been possible without the miraculous feats performed by Mrs. Terry Runyon. Her constant encouragement, knowledge and vast amount of contacts made her a crucial part of every aspect of this study.

An acknowledgment is also in order for my supervisory committee Dr. João Soares and Dr. Hongbo Zeng for their efforts in expediting my success, as well as Dr. Ehsan Toyserkani for agreeing to be a part of this adventure.

Additionally, I must thank Dr. Nathan Deisman, for developing and instructing me in the use of the Virtual Lab Assistant. Without his help, a large portion of this study would be incomplete.

A special thank you to Dr. André McDonald, for which his guidance, training and overall support through my studies over the years has attributed greatly to the success of this project.

I am also thankful to all the staff, students and industrial partners of Materials at the Interface, RG^2, Foundation CMG and NSERC for which this project would not have been possible without their generous support.

I would also like to thank my family for their love and support over the course of this journey. Particularly, my father, Joel, my mother, Jeanette and my two sisters, Ashley and Dawn. Whether it was to celebrate my accomplishments or provide counselling on my defeats, I could always count on them to be there for me.

Last, but not least, a special thank you to Larysa Pochodaj, for your love, support and understanding. For always believing in me and providing a light at the end of the tunnel, я тебе люблю.

Table of Contents

List of Figures

List of Tables

List of Abbreviations

3D:	Three-dimensional
ABS:	Acrylonitrile Butadiene Styrene
AFM:	Atomic Force Microscopy
AM:	Additive Manufacturing
APTMS:	(3-Aminopropyl)trimethoxysilane
ASTM:	American Society for Testing and Materials
BPM:	Bonded Particle Method
BSC:	Benzene Sulfonyl Chloride
DDTES:	Dodecyltriethoxysilane
DIC:	Differential Interference Contrast
DIUF:	Distilled Ultra-filtered Water
DOF:	Degrees of Freedom
DSC:	Differential Scanning Calorimetry
FA:	Furfuryl Alcohol
FAD:	Furfuraldehyde
FDM:	Fused Deposition Modeling
FEA:	Finite Element Analysis
FTIR:	Fourier Transform Infrared Spectroscopy
GPC:	Gel Permeation Chromatography
GPTMS:	(3-Glycidoxypropyl)trimethoxysilane
HIPS:	High Impact Polystyrene
HMDS:	Hexamethyldisilizane
MJM:	Multi-Jet Modeling
NMR:	Nuclear Magnetic Resonance Spectroscopy
OPA:	O-phosphoric Acid
PAI:	Polyamide-imide

PE:	Polyethylene
PEEK:	Polyether-ether-ketone
PF:	Paraformaldehyde
PFA:	Poly-furfuryl Alcohol
PFC:	Particle Flow Code
PMMA:	Poly(methyl-methacrylate)
PP:	Polypropylene
PTS:	P-toluenesulphonic Acid
PTSC:	P-toluene Sulfonyl Chloride
RFC:	Rock Mass Classification
SA:	Sulphamic Acid
SCA:	Silane Coupling Agent
SEM:	Scanning Electron Microscope
SLA:	Stereo Lithography
SLS:	Selective Laser Sintering
TFA:	Trifluoroacetic Acid
UCS:	Unconfined Compressive Strength
UV:	Ultra-violet
VLA:	Virtual Lab Assistant
WPG:	Weight Percent Gain
XPS:	X-ray Photoelectron Spectroscopy

List of Symbols

Symbol	Description	Unit
$^{\circ}$	Degree	-
α	Cantilever-tip constant	-
α_o	Constant for Sneddon's elastic contact	-
A	Cantilever sensitivity	-
A_o	Projected area of elastic contact	$[\text{nm}^2]$
a	Contact radius of indenter tip	$[\text{nm}]$
C_f	Load frame compliance	$[\text{m/N}]$
C_s	Sample compliance	$[\text{m/N}]$
d_h	Shear displacement	$[\text{m}]$
d_{hp}	Peak shear displacement	$[\text{m}]$
d_{hr}	Residual shear displacement	$[\text{m}]$
dP/dh	Slope of load versus displacement curve	$[\text{mPa/nm}]$
E	Elastic modulus	$[\text{GPa}]$
$\bar{E}_c$	Cement (parallel bond) elastic modulus	$[\text{GPa}]$
E_i	Elastic modulus of indenter	$[\text{GPa}]$
E_r	Reduced elastic modulus	$[\text{GPa}]$
E_{IT}	Indentation elastic modulus	$[\text{GPa}]$
F	Applied force	$[\text{N}]$
h	Indentation tip depth penetration	$[\text{nm}]$
h_c	Indenter contact depth	$[\text{nm}]$
h_f	Indentation tip final depth	$[\text{nm}]$
h_{max}	Indentation tip depth penetration (max)	$[\text{nm}]$
H_{IT}	indentation hardness	$[\text{MPa}]$
HV_{IT}	Vickers Hardness	$[\text{Vickers}]$
K	Slope of unloading curve for AFM	$[\text{um/V}]$

k_n	Normal stiffness	[Pa/m]
k_s	Shear stiffness	[Pa/m]
$k_n/d\delta_n'$	Stiffness characteristic	[mm^{-1}]
k_n/k_s	Stiffness ratio	-
v	Poisson's ratio	-
v_i	Poisson's ratio of indenter	-
m	Constant for Sneddon's elastic contact	-
m_b	Mass of binder	[g]
M_n	Molecular weight (number average)	[g/mol]
P	Load	[MPa]
P_{max}	Load at maximum indentation	[MPa]
ρ_b	Density of binder	[g/cm^3]
σ	Strength (bond)	[MPa]
σ_n	Normal stress	[MPa]
S	Unloading stiffness	[mPa/nm]
τ	Shear stress	[MPa]
V_b	Volume fraction of binder	[%]
V_b^{calc}	Volume fraction of binder calculated	[%]
V_f^{set}	Volume fraction of binder set	[%]
V_j	Normal displacement	[m]
V_m	Maximum joint closure	[m]

1   Introduction

1.1   Motivation

Experimental geomechanical studies rely heavily on test specimens cut from reservoir cores from which hydraulic and geomechanical properties of the rock are of primary interest (e.g., flow dynamics, porosity, flaws, unconfined compression strength). Obtaining multiple identical samples for these testing programs is, however, nearly impossible given the natural heterogeneity of the geological formations and thus leads to scatter in test results and uncertainty regarding fundamental relationships that may exist (e.g., interrelationships between flow properties and geomechanical behavior). Additionally, coring procedures introduce extrinsic defects, such as cut marks and micro fractures, that may be detrimental to future testing [1]–[3]. An example of geomaterial cores can be seen in Figure 1.1.1. To avoid the problem of coring multiple samples, numerical modelling has been used to reduce the number of physical samples required and estimate the geomechanical behaviour of rock masses.

Figure 1.1.1: Photograph of multiple rock cores showing variation in texture and color depending on where the sample was extracted [4].

Due to the variance in strength of natural rock due to grain size [5]–[7], number of grain contacts [6], [8]–[10], mineralogy [6], cementing type [11], moisture content [8], [12] and bedding orientation [13], [14], the repeatability of experimental work in geotechnical engineering is often questioned. Measures may be put in place to screen samples for the strength determining factors mentioned previously, but with no apparent solution to identical sampling the high variance in geological samples is largely accepted [15]. Numerical modelling may be used to simulate geological tests through calibration via laboratory testing of natural rock in order to increase the number of samples, however, even more questions may be raised about the validity of the data acquired.

Since the early 1970's, numerical modelling for jointed rock masses has been based on estimated values of shear and normal stiffness of the bonded joints (which dominate the elastic deformation of a rock mass). For the purpose of this thesis, a jointed rock mass is defined as a mass of rock comprised of "interlocking angular particles or hard brittle material separated by discontinuous surfaces which may or may not be coated with weaker materials" [16]. However, it has been stated that there is an "inverse proportionality between test dimension and shear stiffness for a given normal stress" [17], suggesting that there is a scaling issue for experimental testing that has yet to be addressed. Additionally, increasingly sophisticated finite element analysis (FEA) was reviewed by Barton [17] where he reviewed the work of various experts in rock mechanics [18]–[21], but the fundamental problem of "realistic input data" was not addressed (due to the scaling issue mentioned previously) resulting in analysis that fell far from reality. It was suggested that the problem may be solved by large scale in-situ testing, but costing and efficiency make that suggestion unattractive [17], [22].

It was also suggested by Barton [17] that the issue of scaling can be addressed by fabricating model materials that first scale the properties of the intact rock. Intact rock are the "pieces" (igneous, metamorphic or sedimentary) that make up a rock mass, which is usually the geomechanical area of interest. Rock masses contain "discontinuities", such as joints faults and bedding planes that can alter their deformation behaviour [23]. Barton's [17] suggestion of proper model material of intact rock to mimic discontinuous properties was monumental for the time, since it had been difficult up until that point in time to quantify elastic, discontinuous behavior.

Barton's [17] methodology of producing intact rock models was dependent on two, very key criteria. The first being that the models must have "unstable" behaviour, meaning that there is a marked drop in peak strength after small displacements, leading to a lower residual strength. If there is no drop in residual strength (i.e. the rock continues to increase in strength during shear) then the model is not applicable to natural materials. A schematic contrasting the differences between the two behaviours described earlier is shown in Figure 1.1.2. Secondly, the artificial model must be practical. If the method of fabrication is onerous, then it is meaningless, as multiple samples need to be fabricated for statistical importance. In Stimpson's [24] review of several physical rock modelling procedures, the most widely accepted method was creating casts from smooth molds, allowing for different materials to be placed between two blocks in order to increase the friction angle during a shear test. A friction angle of up to 46° was reported, but it produced a "stable" joint with no residual shear strength after large displacements [25].
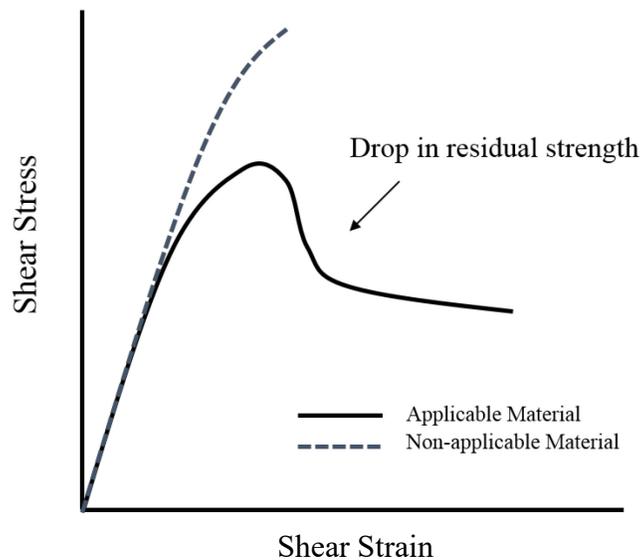
Figure 1.1.2: Schematic of shear stress versus shear strain curves for model geomaterials showing a marked drop in strength after small displacements (applicable material) and one without (non-applicable material).

The aim of the artificial geomaterials mentioned earlier was to determine the elastic discontinuous properties of intact rock, which would then aid in FEA to describe the behaviour of rock masses in geomechanical studies. In particular, the elastic discontinuous properties are required when scaling from the micro-scale to the basin-scale for FEA modelling and dominate

the mechanical behaviour of the material. The terms "normal stiffness" (k_n) and "shear stiffness" (k_s) were introduced by Goodman et al. [21] in 1968 and helped describe the elusive property of elastic discontinuous behaviour of intact rock joints. Paraphrasing Bandis et al. [26], both k_n and k_s describe the rate of change of normal stress (σ_n) with respect to normal displacements (V_j) and of the shear stress (τ) with respect to shear displacement (d_h), respectively. The above quantities combined with peak (d_{hp}) and residual (d_{hr}) shear displacement, as well as maximum joint closure (V_m), allow for computation of joint contribution to the total displacement of a rock mass. Additionally, the term "stiffness characteristic" was introduced by Evans et al. [27] in 1992, which describes the normal stiffness behaviour of a fracture (discontinuity) by multiplication of the effective normal stress.

Although it is difficult to compile all values of k_n and k_s used in numerical modelling studies (since only the default k_n/k_s ratio of 2.5 is reported), in 2008 a large amount of data was compiled by Zangerl et al. [28] in order to provide the stiffness characteristic, $dk_n/d\delta_n'$, for various types of granite rock. The data compiled by Zangerl et al. [28] is shown below graphically in Figure 1.1.3, where it is clear that there is no simple correlation between datasets for geomaterials. For clarity, a portion of the article is provided below in order to define $dk_n/d\delta_n'$ further:

> "Fracture normal stiffness, k_n, is defined as the instantaneous slope of the effective normal stress versus fracture aperture change curve, and has dimensions Pascals per metres. For the semi-logarithmic closure law, the predicted change in mechanical aperture, Δa_m, resulting from a change in effective normal stress from an arbitrary reference value σ_n^{ref} to a value σ_n' is given by
>
> $$-\Delta a_m = \frac{1}{dk_n/d\sigma_n'} \ln(\sigma_n'/\sigma_n^{ref})$$
>
> where $dk_n/d\delta_n'$ is a constant that will be referred to as the 'stiffness characteristic' [27]"
> [28, p. 1501].
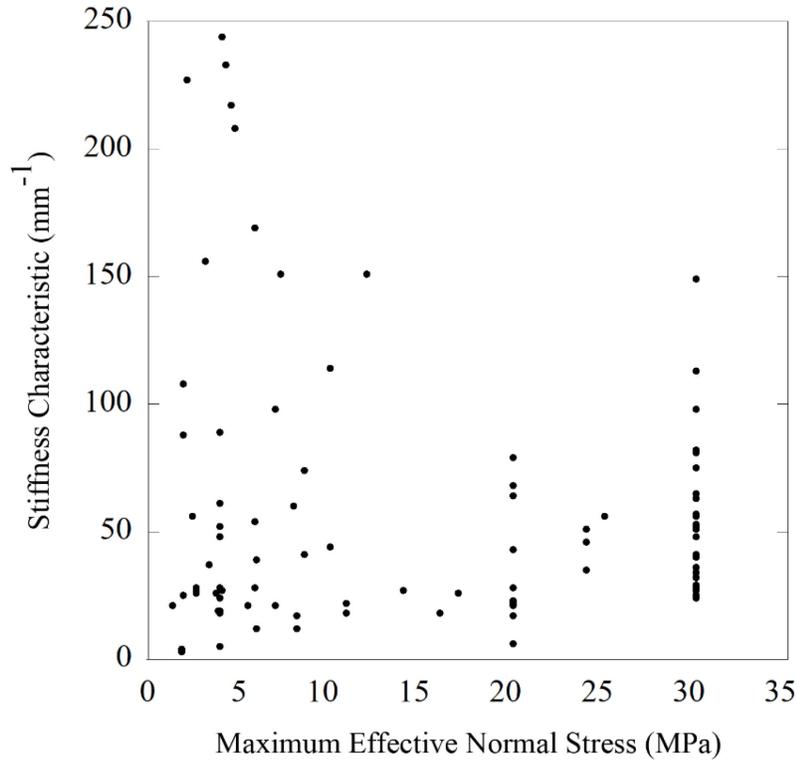
Figure 1.1.3: Compilation of laboratory and in-situ testing of rock fractures showing the changes in stiffness characteristics from samples of various origin and sizes originally published in Zangerl et al. [28]. Contains data collected from [29]–[43].

Therefore, although data is available, selecting a sample that mimics the behaviour of a specific geomechanical formation or rock mass is daunting. Rock is heterogeneous in nature, which amplifies the problem of assigning material properties such as Young's modulus, since there are no pre-defined mechanical properties for any rock mass, nor any direct methods available for micromechanical property determination.

However, recent advances in additive manufacturing have been presented that offer new methods of producing synthetic geomaterials [44]–[46]. More specifically, Osigna et al. [47] presented 3D-printed sandstone fabricated using binder jetting technology. By using furfuryl alcohol and silica sand, the repeatability limit of unconfined compressive strength (UCS) tests of 3D-printed sandstone was improved from 15.8 MPa to 2.14 MPa when compared to Berea sandstone [2], [3], [47]. Additionally, the Young's modulus of 3D-printed sandstone had a repeatability limit of 1.19 GPa versus 3.37 GPa when compared to Berea sandstone [2], [3], which

5

is unprecedented in rock mechanics [47]. Additionally, Primkulov et al. [15] published a study where the standard deviation of UCS tests for 3D-printed sandstone is just 1.1 MPa, which is remarkably low when compared to commonly used geomaterials such as Berea sandstone (17.9 MPa), Red Jacket sandstone (23.5 MPa) and Island Creek sandstone (36.9 MPa) [48] .

3D-printed sandstone has been proven as a consistent method for fabricating geomaterials, but current testing has been limited to macroscopic testing such as UCS and Young's modulus [15], [47]. However, in order to enhance the capabilities of 3D-printed sandstone, the fundamental material property relationships must be explored, especially at the microscopic level. For example, the micromechanical properties of individual bonds and how the Young's modulus of the binding material compares to that of the overall sample. Another question yet to be answered is how far can we currently push the limits of binder jetting technology? Is there a limit to the volume fraction of binder in 3D-printed sandstone? Only by characterizing 3D-printed sandstone at the microscopic level can we begin to answer these questions.

1.2   Contributions

To address the problem of heterogeneity in laboratory-tested rock, additive manufacturing has been shown as a viable method to produce model sandstone and follows Barton's criteria of unstable behaviour and ease of fabrication [17], [47]. The 3D-printing process selected in this study along with the tight size distribution of silica sand feedstock provides a controlled method for producing model sandstone with repeatable macroscopic properties [15], [47].

Regardless of the style of laboratory testing or FEA modelling used, natural rock is heterogeneous in nature and the scaling effects of bonded joints in rock have yet to be fully addressed [49]. However, with the rise in the amount of artificial rock being produced via additive manufacturing from materials such as thermoplastics and ceramics [44], [45], [50]–[52], the heterogeneity of analogue rock is being reduced as more controlled methods of fabrication are explored.

Figure 1.2.1 contains an illustration of the research paradigm that encompasses the current thesis of fabricating, characterizing and improving the performance of 3D-printed sandstone, where a few key contributions are outlined. By combining studies of structure, processing,

properties and performance, we can begin to understand the material-property relationships and increase 3D-printed sandstone performance for use in future geological studies.

PERFORMANCE
Improvement of UCS through the use of a SCA

PROPERTIES
Quantify the Young's modulus of the binder between sand grains

PROCESS
Calibration of binder volume fraction
Determination of binder volume fraction limit

STRUCTURE
Comparison of 3D-printed sandstone to Berea sandstone

Characterization of binder necks through microscopy
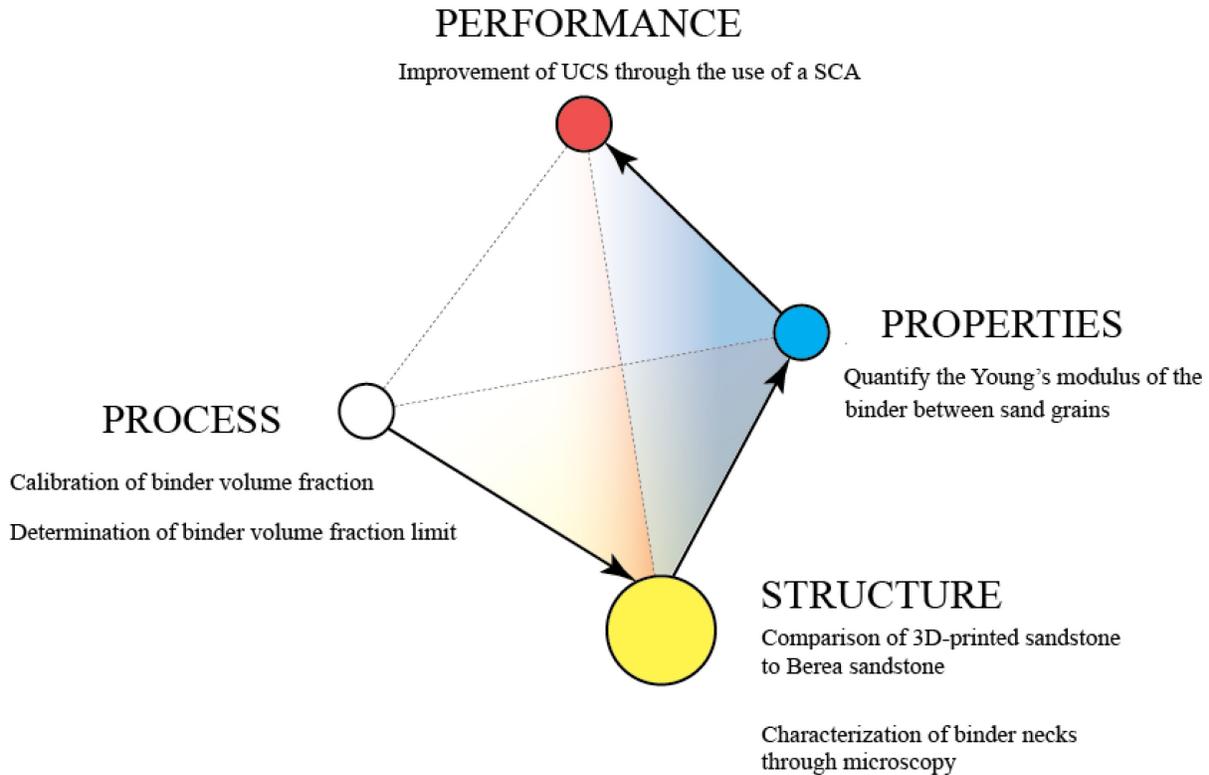
Figure 1.2.1: Illustration of the research paradigm encompassing the contributions of the thesis in the areas of performance, properties, processing and structure with key contributions outlined. Figure adapted with permission from John Nychka and Glenn Hibbard.

In terms of processing, the 3D-printed binder volume fraction limit was determined through a calibration study via thermogravimetric techniques, where it was found that there was a mismatch between the binder set point (programmed on the 3D-printer) and the actual binder volume fraction within the sample, thus a formula was developed to aid in fabrication of samples. It was also found that there is a limit to the amount of binder that can be jetted into 3D-printed sandstone of ~8 vol. %. Exceeding this limit results in loss of dimensional control of printed samples through bleeding by capillary forces and pooling via gravity. An innovative use of silane coupling agents (SCA) also provided a new prospect of increasing the UCS of 3D-printed sandstone.

For structure-related studies 3D-printed sandstone was compared to Berea sandstone where their microstructures were compared and contrasted. 3D-printed sandstone was examined via microscopy where ultra-violet (UV) light and fluorescent dye was used to capture images of single binder necks. Atomic force microscopy (AFM) was used as well to provide topographic 3D images of binder necks in detail.

A combination of AFM and nanoindentation techniques are provided that present the Young's modulus of the 3D-printed binder between sand grains, which may be used as a vital parameter in FEA modelling. As far as the author knows, the acquisition of a micromechanical property between the particles of a geomaterial is a novel prospect. It is hoped that the quantification of micromechanical properties of geomaterials begins to increase the accuracy of FEA simulation and will be discussed in a later section.

By using the information gathered from the processing, structure and property-related studies, the performance of 3D-printed sandstone could be improved. UCS testing was performed on 3D-printed samples with increased binder saturation and a two-fold increase in strength is reported within. Additionally, data gathered through studies involving SCAs (where an additional two-fold increase of strength was observed on cast samples is presented) with the intention of improving the strength of 3D-printed sandstone, further.

1.3   Research Objectives

Several research objectives were set for this study, separated into three main categories: fabrication, characterization and performance, which are presented below in Table 1.3.1.

Table 1.3.1: Research objectives of the study of 3D-printed sandstone.

Category	Objective	Chapter
Fabrication	• Fabricate 3D-printed model sandstone	3
Characterization	• Visualize 3D-printed sandstone microscopically	4
	• Characterize binder and silica sand materials	4
	• Calibrate amount of binder during printing	4
	• Determine UCS of 3D-printed model sandstone	4
	• Determine elastic moduli of 3D-printed binder necks	5
Performance	• Improve binder adhesion through SCAs to address the organic/inorganic coupling of 3D-printed binder and silica sand	6
Modeling	• Calculate and model elastic moduli of 3D-printed bonded joints	7

2   Background

2.1   Additive Manufacturing

Additive manufacturing (AM) has advanced over the past several decades and allows for complex parts to be fabricated, where traditional methods of fabrication such as casting or molding would prove difficult. Several different forms of AM are summarized in Table 2.1.1.

Table 2.1.1: Summary of additive manufacturing methods [53].

Method	Description
Vat Photopolymerization	Liquid photopolymer in a vat is selectively cured by light-activated polymerization
Material Jetting	Droplets of build material are selectively deposited
Binder Jetting	A liquid binding agent is selectively deposited to join powder materials.
Material Extrusion	Material is selectively dispensed through a nozzle or orifice.
Powder Bed Fusion	Thermal energy selectively fuses regions of a powder bed.
Sheet Lamination	Sheets of a material are bonded to form an object.
Directed Energy Deposition	Focused thermal energy is used to fuse materials by melting as they are deposited.

The unique task of creating 3D-printed sandstone removes several of the available AM methods as options. Several printing methods use some form of a polymer as the main building material, whether it is filament or resin, and are not compatible with ceramics due to their high melting point. Although powder bed fusion and directed energy deposition printing have the ability to work with metals, and in some case ceramics, the parts created are almost fully dense due to the material entering a molten state [54]. Therefore, the only viable option is binder jetting, a powder-based AM technology invented at the Massachusetts Institute of Technology in 1993 [55]. In binder jetting, a layer of sand (or other particulate media) is spread by rollers, followed by a print head "jetting" a binder phase onto the sand to create a single 2D image. The process repeats in a

layer-by-layer process until a 3D part is fabricated. A schematic of the procedure is shown below in Figure 2.1.1. The method used in this study is similar to Figure 2.1.1, but the overall process is more refined and the use of rollers has been replaced by a "recoater" that travels over the print bed while vibrating, allowing the silica sand to free-fall into place. A description of the 3D Printer used for this project can be found in Section 3.2. A similar printing process using sand has been utilized in a recent study, but the results focused mainly on the fracture surface of the material [56]. Examples of 3D-printed parts are shown below in Figure 2.1.2.
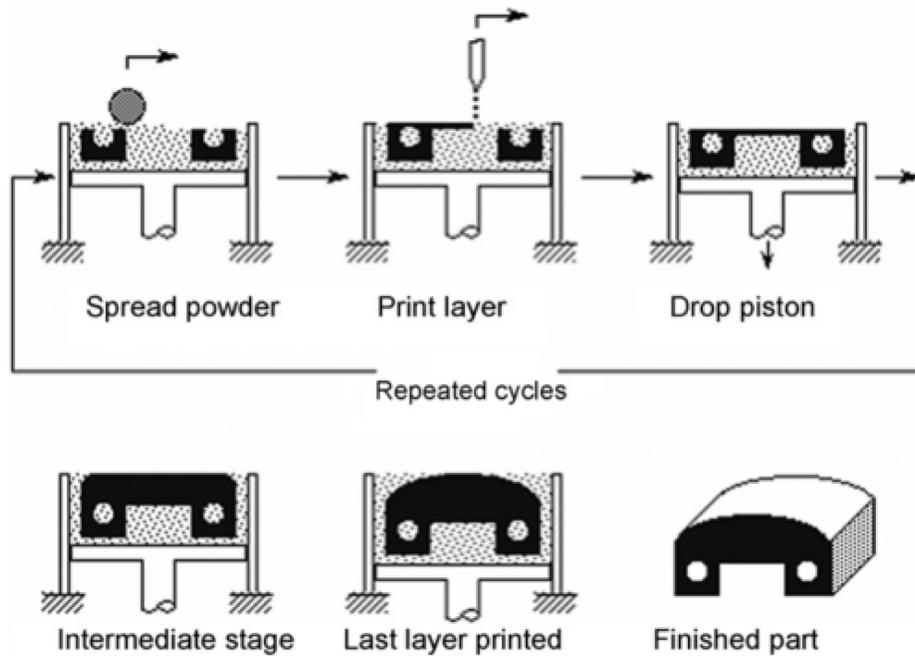
Figure 2.1.1: Schematic of the powder or binder jetting printing process. Reprinted with permission from Patirupanusara et al. [57] © 2017 Elsevier.

Figure 2.1.2: A photograph of a 3D-printed shear sample and tensile specimen, from left to right respectively, fabricated via the M-Flex Sand Printer.

With binder jetting, we gain the benefit of starting with one of the major constituents of sandstone: silica sand. By jetting a binder onto the sand, we are attempting to reproduce the way that sandstone is formed naturally. Sandstone is formed by groundwater containing dissolved minerals, such as calcite ($CaCO_3$), silica (SiO_2) and/or iron oxide (Fe_2O_3), permeating areas with fine gravel or sand. A chemical reaction takes place from either internal (feldspar-related) or external (mudrock-related) sources, leading to a stoichiometric replacement of feldspar ($2KAlSi_3O_8$) with a lower Si/Al ratio such as:

$$2KAlSi_3O_8 + 2H^+ + H_2O = Al_2Si_2O_5(OH)_4 + 4SiO_2 + 2K^+ \qquad (1)$$

or

$$3KAlSi_3O_8 + 2H^+ = KAl_3Si_3O_{10}(OH)_2 + 6SiO_2 + 2K^+ \qquad (2)$$
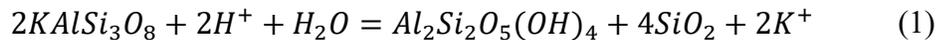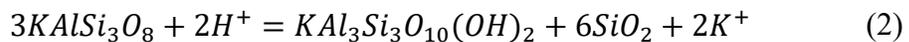
where the potassium rich feldspar is replaced by kaolinite ($Al_2Si_2O_5(OH)_4$), muscovite (($KAl_3Si_3O_{10}(OH)_2$) and quartz (SiO_2) [58]. In the case of binder jetting, we are permeating the sand deposit with a synthetic "cement", not unlike the way the earth creates sandstone, albeit at

a much faster rate. However, although the binder used in 3D-printed sandstone may be referred to as the cement holding sand grains together, the bond between particles is relatively poor compared to natural sandstone and will be discussed in detail later. In contrast, the ground water that infiltrates natural sand stone precipitates to form a crystalline material, bonding the sand grains chemically and creating a much stronger bond [59].

For the case of laser sintering or fused deposition modelling (AM), the parts are close to fully dense after fabrication and the importance of binding decreases as the part becomes monolithic [60]. However, for 3D-printed sand, the fabricated parts are not fully dense (to be comparable to sandstone) and the strength of the printed part relies heavily on the binder phase. During an unconfined compression strength test of a sample, the axis perpendicular to the direction of compressional force will experience tension. At this point the strength of the binder is critical, since the sample can no longer benefit from grain to grain contact for load bearing.

Although natural sand stone has increased particle packing due to pressure and time, the porosity of 3D-printed sandstone may be controlled by either increasing/decreasing the powder bed thickness, binder saturation or size distribution and shape of particles [61]–[64], allowing for controlled permeability of the sample; another reason why binder jetting is the AM method of choice for this project.

The 3D-printing process utilized in this thesis contains three key aspects: silica sand, binder (furfuryl alcohol) and activator (p-toluene sulphonic acid). Cross-linked or "activated" binder, will be termed poly-furfuryl alcohol (PFA). A review of the polymerization and properties of the binder is provided below.

2.2   The Binder – Furfuryl Alcohol

2.2.1 Polymerization

The ability for furfuryl alcohol (FA) to be binder-jetted in its liquid monomer form makes it ideal for fabrication of 3D-printed sandstone. FA is made from agricultural waste, which makes it an inexpensive alternative to other adhesives on the market and can even be found in processed food products and coffee [65]. Furan resins, made from FA and furfuraldehyde, are used extensively in the wood industry for bonding, the casting industry for binding molds and various

other adhesive based products [65]–[68]. Additionally, an alternative to construction cement (such as Portland cement) is a furan-based polymer cement, with increased resistance to water absorption, heat, acid and alkali attack and in some cases a higher compressive strength and lower setting time [68].

The kinetics of the polymerization of FA has been argued extensively [69]–[75] with two schemes generally accepted and originally proposed by Dunlop et al. [76] (Figure 2.2.1) where the alcohol group is condensed by a mobile hydrogen to give structure (1) or the linkage of two alcohol groups to give structure (2). Regardless, the polymerization reaction remains troublesome due to the C-5 position of the furan ring (Figure 2.2.2) spawning several side reactions leading to branching, coloring and cross-linking, that are difficult to selectively analyze [72].
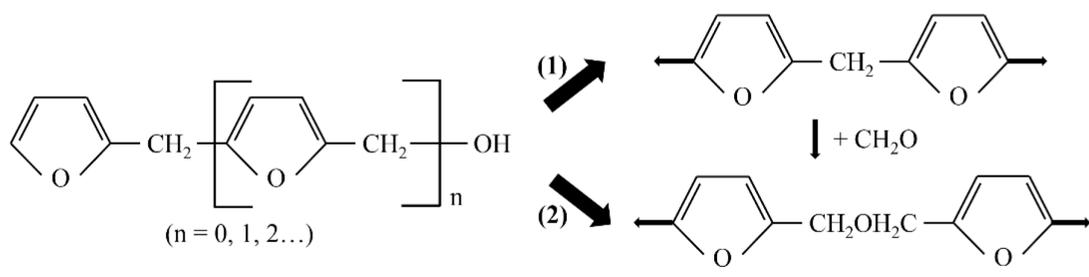
Figure 2.2.1: Polymerization scheme for furfuryl alcohol originally proposed by Dunlop et al. [26]. Figure adapted with permission from Choura et al. [11] © 2017 American Chemical Society.
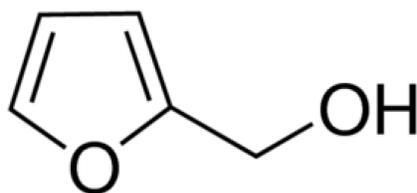
Figure 2.2.2: Chemical structure of furfuryl alcohol.

The properties of polymerized FA (PFA) have been studied since its discovery in the early 1950s, but the specifics of polymer property response with experimental conditions is most important for additive manufacturing, as the type of catalyst and temperature of the cure can be altered. Therefore, the following review explores the results from various authors concerning the

relationship between catalyst selection, adhesion promotion and temperature profile during curing of PFA.

2.2.2 Fourier Transform Infrared (FTIR) Spectroscopy

One of the largest problems with additive manufacturing of sandstone using PFA as the binder is the lack of adhesive strength between the silica sand and polymer phase. A scanning electron microscope (SEM) image is presented below in Figure 2.2.3, with labels indicating an adhesive bond and possible sites of poor adhesion (due to residual PFA from suspected pull-off). Whether failure is adhesive or cohesive is difficult to ascertain. Principe et al. [77] studied the effects of maleic anhydride additions on PFA adhesion for photoresist applications. By introducing carbonyl groups through the maleic anhydride, they were able to improve the formation of films and adherence onto copper surfaces. Two Fourier transform infrared spectroscopy (FTIR) spectra of PFA with and without maleic anhydride are shown below in Figure 2.2.4, respectively. The evidence of successful carbonyl formation can be seen by the increased intensity at $1700 cm^{-1}$, along with new peaks present at 1727 and 1767 cm^{-1}, which are typical for carboxylic anhydrides [77].
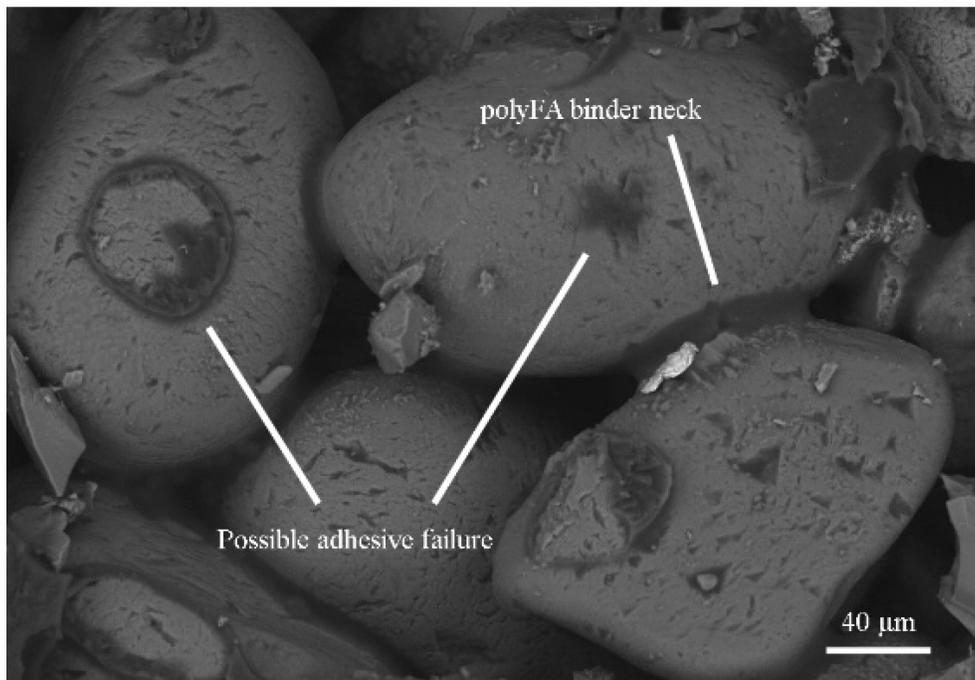
Figure 2.2.3: SEM image of 3D-printed sandstone showing possible polymerized furfuryl alcohol adhesive failure.
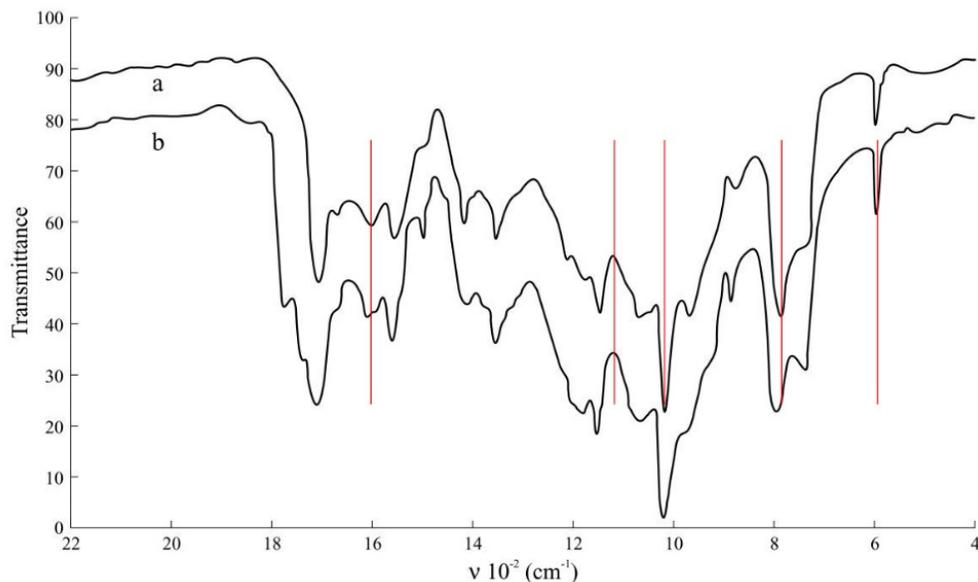
Figure 2.2.4: FTIR spectra of a) PFA and b) PFA reacted with maleic anhydride with characteristic furan ring signals highlighted in red (1600, 1150, 1020, 780 and 600 cm-[1]). Figure adapted from Principe et al. [77] under a Creative Commons Attribution License (Polímeros).

2.2.3 Differential Scanning Calorimetry (DSC)

In 2013, Herold et al. [78] published a series of differential scanning calorimetry (DSC) experiments on wooden veneer samples impregnated with PFA and varying concentrations of maleic anhydride. Figure 2.2.5 shows the first DSC thermogram showing a strong exothermic reaction beginning around 110 °C for FA mixed with 10 wt. % maleic anhydride. Conversely, a strong endothermic reaction takes place for 100 % FA, which is most likely due to evaporation of the solution [78].
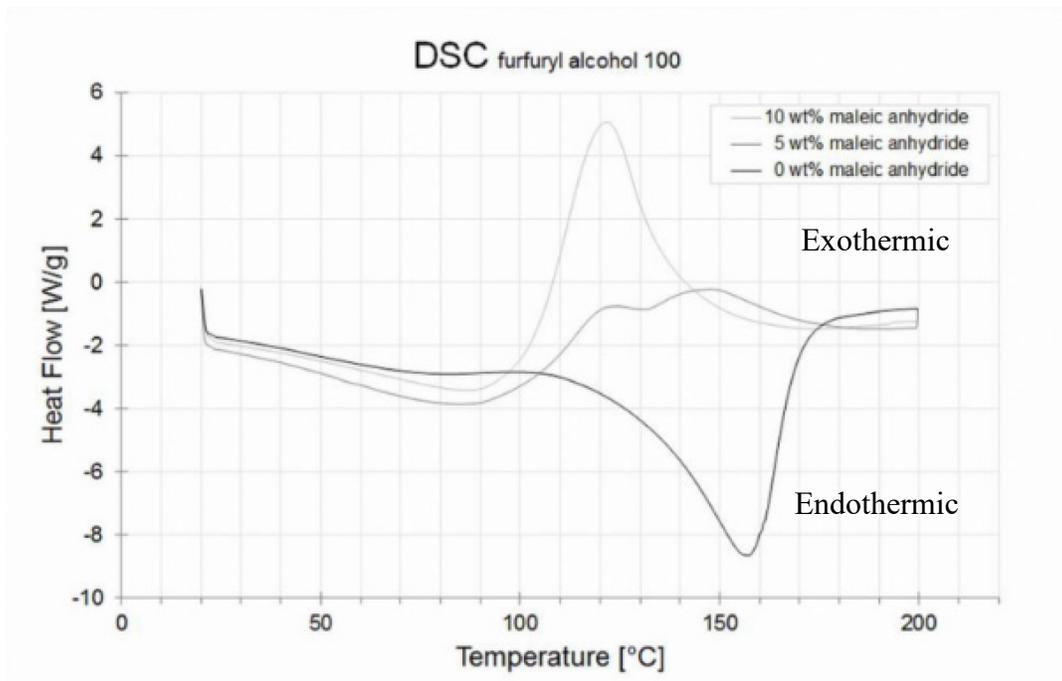
Figure 2.2.5: DSC thermogram with a heating ramp of 10°C/min; veneer sample impregnated with FA and varying amounts of maleic anhydride [78].

To test what effect reaction temperature has on polymerization, Herold et al. [78] ran DSC measurements during isothermal conditions, presented in Figure 2.2.6. In all cases, 10 wt. % maleic anhydride was used. The initial endothermic change in the thermogram for all cases is most likely due to evaporation of solvent during the initial 100 °C ramp up. Regardless, according to Figure 2.2.6, it seems that the run taking place at 140 °C was the only run high enough in temperature to provide enough energy for polymerization, signified by the exothermic peak around 1.5 minutes.
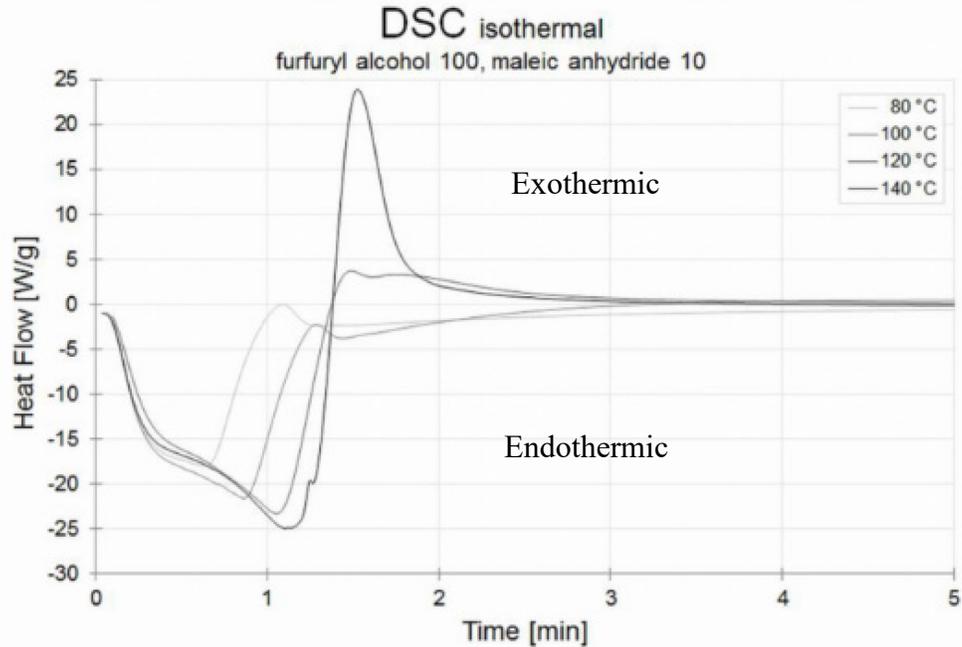
Figure 2.2.6: DSC isothermal temperature profiles of veneer samples impregnated with FA and 10 wt. % maleic anhydride with an initial heat ramp of 100ºC/min [78].

Additionally, Herold et al. [78] studied the weight percent gain (WPG) of veneer samples impregnated with FA and maleic anhydride, since it was found that at least 58 % of the unreacted FA was lost during the curing step, whether due to evaporation or water release during the condensation reaction [78]. Although the results presented below in Figure 2.2.7 show a general increase in WPG with increased maleic anhydride content, it would be misleading to state that the relationship is linear as suggested by the trend lines [78]. Regardless, maleic anhydride may be a probable solution to PFA retention during polymerization, meaning that an increase in adhesion strength for 3D-printed sand may be possible. However, through personal experience, the addition of maleic anhydride (a weak, organic acid) does not result in the same gelation as p-toluene sulphonic acid (a strong, inorganic acid), meaning that although the adhesive strength is increased, the strength and stiffness of the binder itself may be weaker as the amount of cross-linking is lower. Additionally, p-toluene sulphonic acid enacts an immediate color change of the PFA, while maleic anhydride has a slow gelation period of several hours.
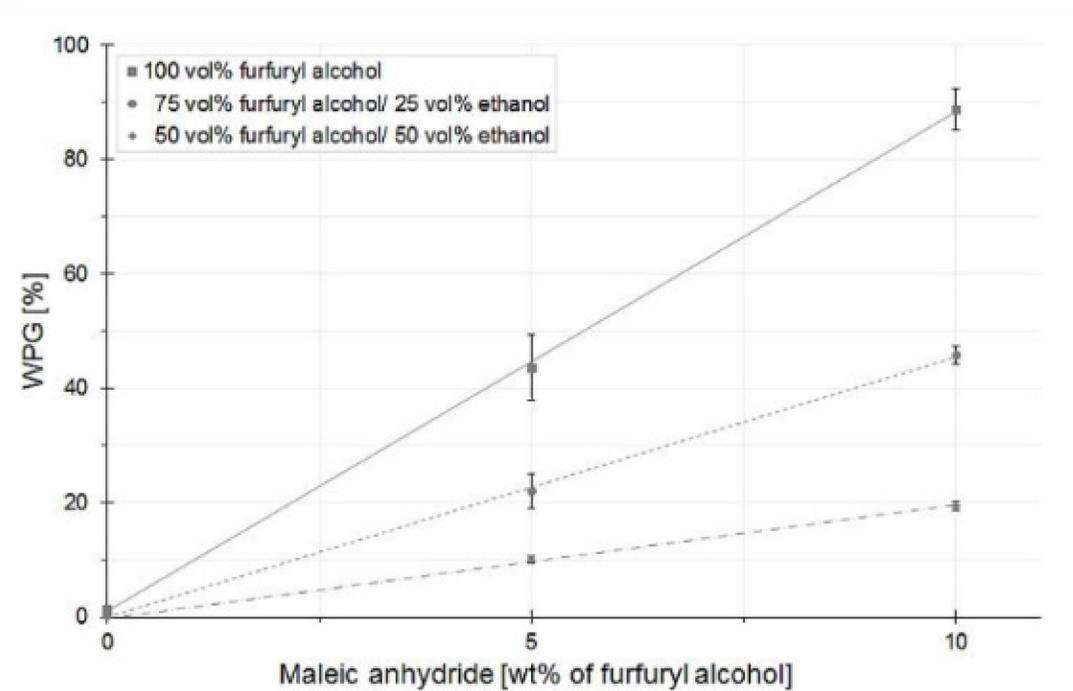
Figure 2.2.7: Weight percent gain (WPG) versus maleic anhydride content for wooden veneer samples impregnated with PFA blends (ethanol was used to test the effect of dilution on PFA) [78].

2.2.4 Nuclear Magnetic Resonance (NMR) Spectroscopy

Two different inorganic acid catalysts were used by Principe et al. [77] to polymerize FA: trifluoroacetic acid (TFA) and p-toluenesulphonic acid (PTS), followed by analysis using nuclear magnetic resonance (NMR) spectroscopy. The following results are interesting, as the 3D printing of sandstone for this study uses PTS as a catalyst. Figure 2.2.8 below presents the polymerization schemes mentioned earlier, with significant NMR signals attached. Figure 2.2.9 and Figure 2.2.10 show the NMR spectra of FA polymerized with TFA, showing no signals at $\delta = 4.50$ or 62.93 ppm, with a rather strong peak at ~28 ppm and a broad peak ~38 ppm suggesting the presence of both Scheme 1 and 3 from Figure 2.2.8. However, although not shown in the publication, it is stated that the NMR spectra for FA polymerized with PTS shows a strong signal at both $\delta = 4.50$ and 63 ppm, suggesting that FA polymerized with PTS is predominantly Scheme 2 from Figure 2.2.1 and

Figure 2.2.8, rather than Scheme 1 as for FA polymerized with TFA [77]. In other words, FA polymerized with TFA creates CH_2 bonding, while FA polymerized with PTS results in CH_2OCH_2 bonding.
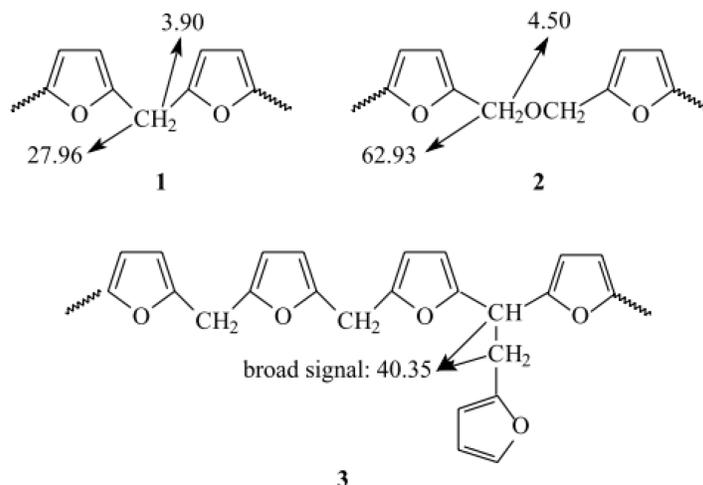
Figure 2.2.8: Typical NMR signals from different PFA polymerization products. Figure reprinted from Principe et al. [77] under a Creative Commons Attribution License (Polímeros).
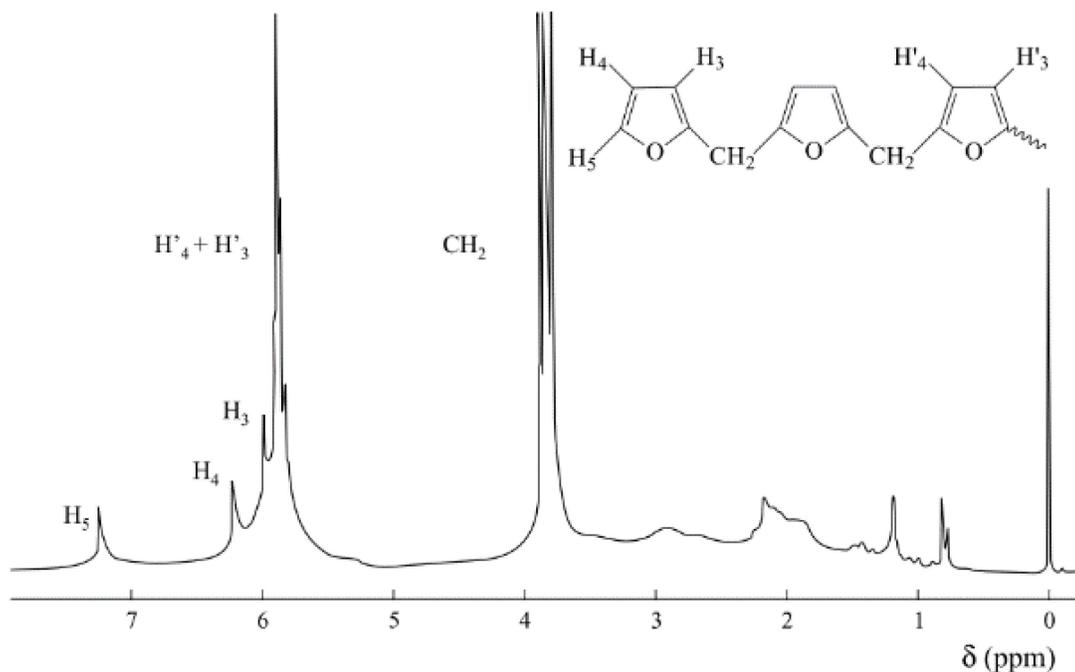
Figure 2.2.9: ^{1}H NMR spectrum (600 MHz) of PFA polymerized with TFA. Figure reprinted from Principe et al. [77] under a Creative Commons Attribution License (Polímeros).

20
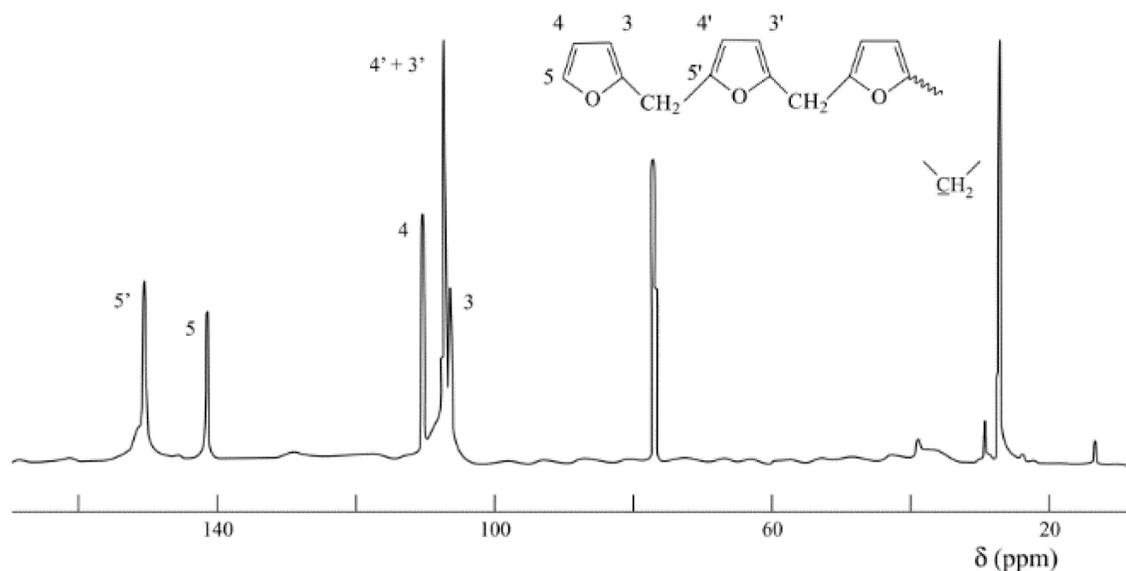
Figure 2.2.10: ^{13}C NMR spectrum (150 MHz) of PFA polymerized with TFA. Figure reprinted from Principe et al. [77] under a Creative Commons Attribution License (Polímeros).

2.2.5 Gel Permeation Chromatography (GPC)

In 1968, Wewerka [67] used GPC to characterize FA polymerized with three different catalysts. The first catalyst used was maleic anhydride, with the GPC curves shown below in Figure 2.2.11, where the change in molecular weight distribution can be accompanied with the change in viscosity. Although the initial polymerization of FA is pH dependent [67], [77]–[79], the reaction quickly becomes "more complicated once layers of higher molecular weight form out of bulk solution" [67]. Interestingly, Wewerka [67] repeated the experiment with ten times the amount of catalyst, with little change in molecular weight being reported (Figure 2.2.12). However, it has been reported elsewhere that an increase in catalyst merely increases the rate at which polymerization takes place and does not change the molecular weight distribution [77]–[79].
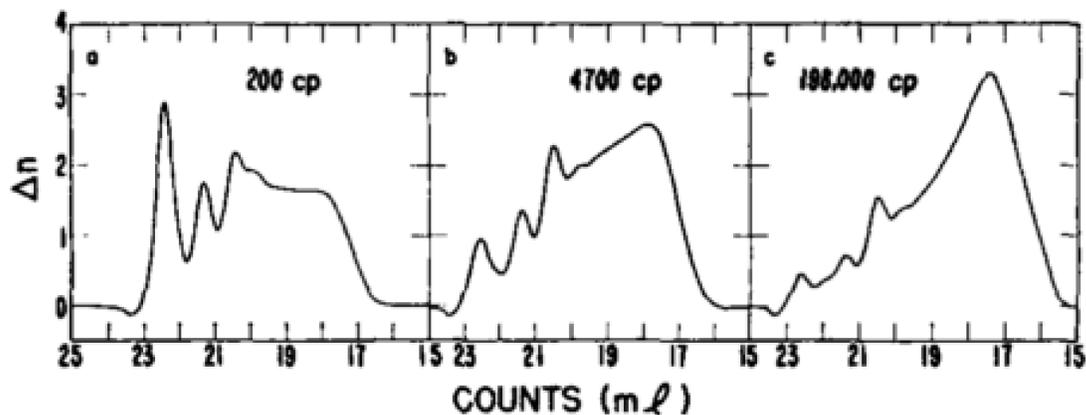
Figure 2.2.11: GPC curves of FA resins catalyzed with 1 g of maleic anhydride. Δn is the difference in refractive index, with elution volume set to 5 mL per count. Figure reprinted with permission from Wewerka [67] © 2017 John Wiley and Sons.
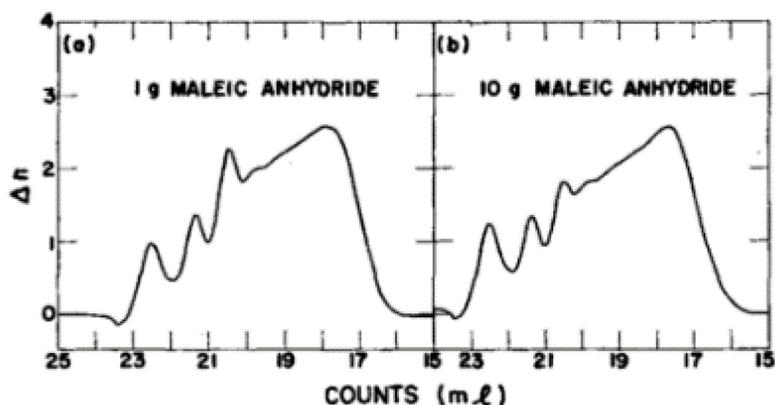
Figure 2.2.12: FA resins synthesized with *a)* 1 g and *b)* 10 g of maleic anhydride. Figure reprinted with permission from Wewerka [67] © 2017 John Wiley and Sons.

Wewerka [67] synthesized more FA resins with maleic anhydride and compared them with FA resins synthesized with phosphoric acid. A comparison of the data captured via GPC in Figure 2.2.13 shows that there is little difference between the catalysts in terms of distribution. However, it was suggested that although the distributions are the same (combined with the fact that no apparent catalyst concentration effect exists) the polymerization reactions are dependent on the concentration of active hydronium ions in solution and not on the specific acid used [67]. He postulates further that "within the areas studied, any complication of the rate law during the latter stages of reaction is independent of the catalyst type or concentration used" [67].
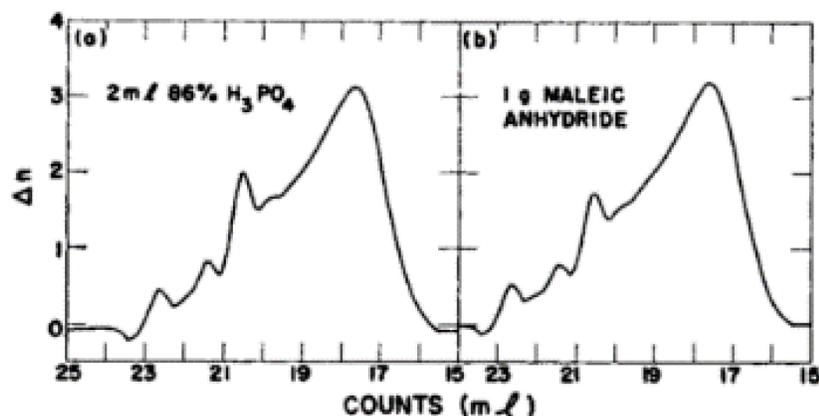
Figure 2.2.13: GPC curves of FA resins made by catalysis with 86% phosphoric acid and maleic anhydride (both resins had similar viscosities after synthesis). Figure reprinted with permission from Wewerka [67] © 2017 John Wiley and Sons.

The third catalyst Wewerka [67] used to synthesize PFA was γ-alumina. His main goal was to determine if there was any noticeable difference between PFA catalyzed via acid. The GPC data collected by Wewerka [67] is shown below in Figure 2.2.14, where the broadening of the peaks at lower molecular weight (higher elution volumes) can be seen when compared to the GPC curves of Figure 2.2.11, Figure 2.2.12 and Figure 2.2.13. He continues to summarize that the "lower molecular weight species of the alumina-catalyzed resins appear to remain in considerably higher concentration throughout the polymerization than do those of the acid-catalyzed resins" [67]. The increase in low molecular weight polymer suggests that the polymerization may be inhibited. He reports other differences with the alumina-catalyzed PFA include a darker color and "slightly burned" odor [67].
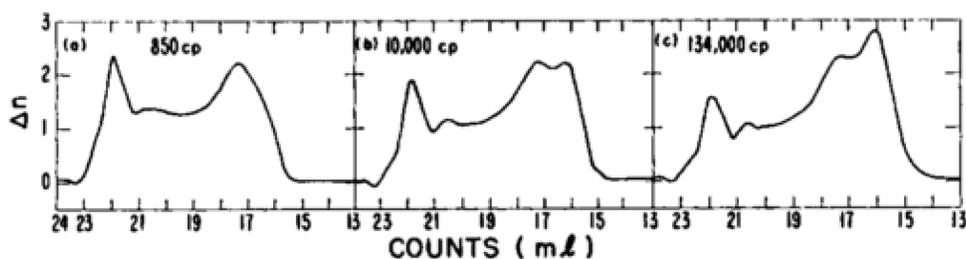
Figure 2.2.14: GPC curves of FA resins made by catalysis with γ–alumina. Figure reprinted with permission from Wewerka [67] © 2017 John Wiley and Sons.

2.2.6 Photo Cross-linking

The last area of review, although not an analytical method, was the cross-linking of FA via ultra-violet (UV) radiation. It has been stated that the "labile hydrogen atoms on carbon atoms are the most likely candidates" with regards to the initialization of photodegradation [72]. As shown below in Figure 2.2.15, UV radiation leads to the abstraction of the tertiary hydrogen of poly(2-vinylfuran), leading to a macro radical that may induce cross-linking [77]. Principe et al. [77] explain further that the major reaction pathways are either: "the attack on some olefin or dihydrofuran carbon atom of the polyunsaturated sequences" or "the addition to monosubstituted furan rings." Both sequences are shown below in Figure 2.2.16. Although able to be cross-linked via UV radiation, the "concentrations of polyunsaturated sequences is low", leading to long reaction times [77]. However, since only a thin film is applied to silica sand particles during 3D printing, it may be beneficial to test the adhesion strength of FA polymerized via UV light versus an acid catalyst. Although not completed in this study, UV curing may be a possible area of study in the future.
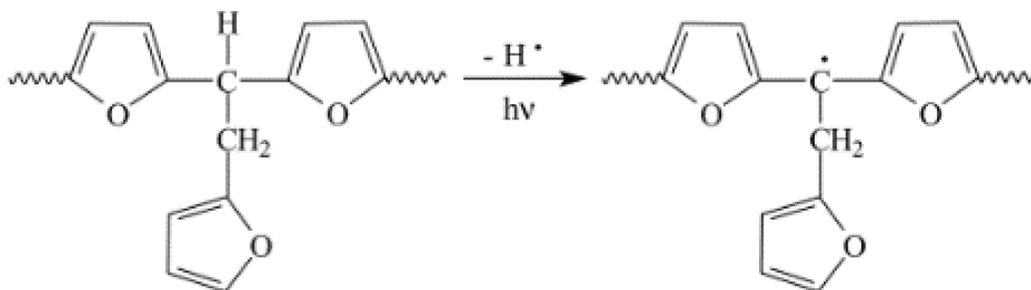
Figure 2.2.15: Photodegradation of a labile hydrogen atom on a carbon atom. Figure reprinted from Principe et al. [77] under a Creative Commons Attribution License (Polímeros).

a)

b)
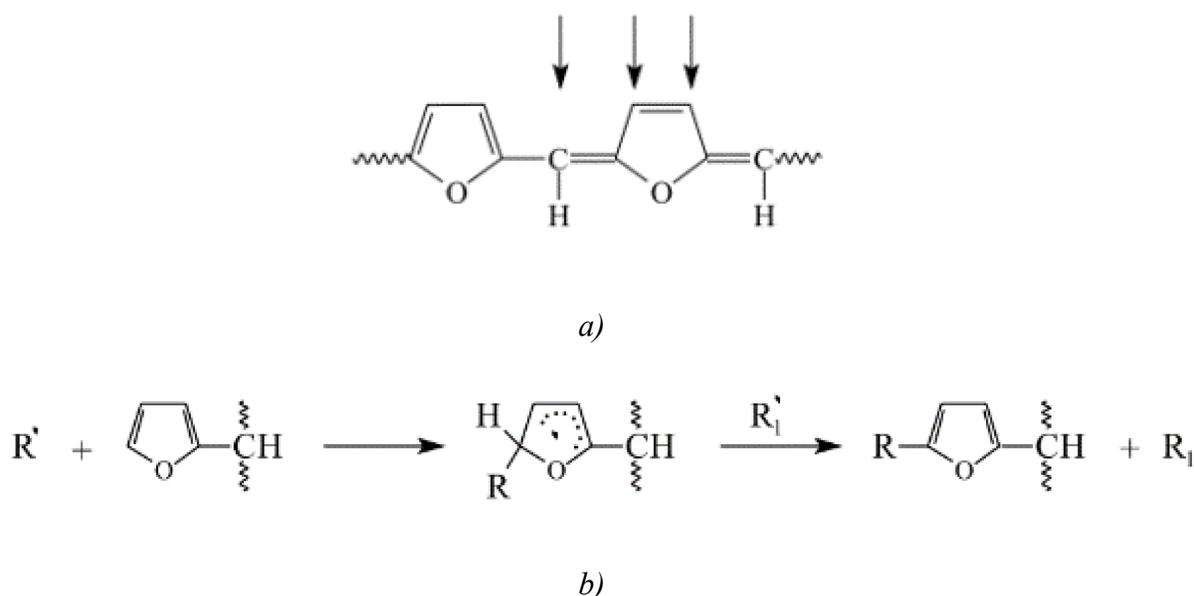
Figure 2.2.16: a) Macroradical attack on a polyolefin b) addition to a monosubstituted furan ring. Figure reprinted from Principe et al. [77] under a Creative Commons Attribution License (Polímeros).

2.2.7 Catalyst Selection

Muthukumar et al. [80] documented several combinations of FA and catalysts incorporated into a polymer concrete, with most catalysts being acidic, which is a popular choice for furfuryl alcohol catalysts [80]–[82]. A summary of the combinations of different catalysts and gel-state of the cross-linked FA is provided in Table 2.2.1 below.

Table 2.2.1: Combinations of Furan-based polymer cement and catalyst combinations [80].

Catalyst	FA	FA + PF	FA +F
OPA	Gels overnight		No gellation
BSC	Local gellation		
PTSC	Rubbery		
SA	Hard		
PTSC/SA	Hard		

FA = furfuryl alcohol

PF = paraformaldehyde

FAD = furfuraldehyde

OPA = o-phosphoric acid

BSC = benzene sulfonyl chloride

PTSC = p-toluene sulfonyl chloride

SA = sulphamic acid

Additionally, Muthukumar et al. [80] used silica sand as the aggregate in the concrete, which is similar to the silica sand used in the 3D-printing system herein. However, the aim was to create fully dense samples, so a distribution of sizes was used to provide optimum packing. In the case of 3D-printed sandstone, a fully dense sample may not be desirable, so binder content or the size distribution of the sand is a possible variable to manipulate in achieving various densities or pore volumes [63], [83]. Another difference was the use of a silane additive, which reduces water absorption in concrete, along with promoting adhesion to the aggregate. It was found that a 0.5% addition by weight of γ-amino propyl-triethoxysilane was enough to almost double the compression strength of the samples [80].

2.2.8 Degradation of Polymerized Furfuryl Alcohol

Due to the polymerization of furfuryl alcohol being a condensation reaction [72], water is produced and must be removed as any moisture can be detrimental to 3D-printed sandstone strength [15]. Residual water may enact ring hydrolysis, leading to the breakdown of furan rings to form aliphatic carboxylic and ketonic groups. Figure 2.2.17 provides a schematic describing the temperatures needed for evolution of molecular groups of PFA.
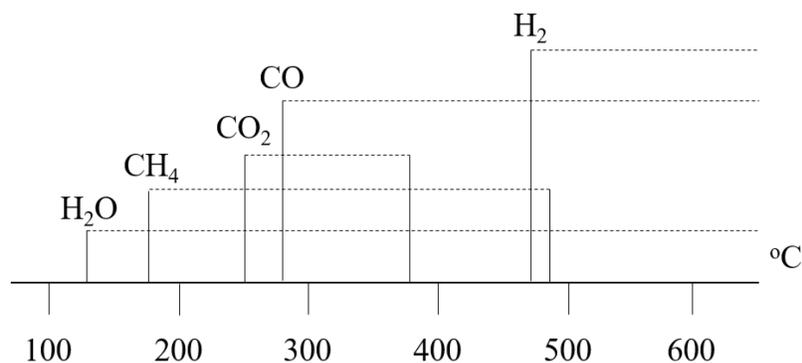
Figure 2.2.17: Degradation mechanics of poly-furfuryl alcohol at specific temperatures showing the evolution of H_2O, CH_4, CO_2, CO and H_2. Adapted with permission from Gaefke et al. [84] © 2017 John Wiley and Sons.

In addition to the results provided in Section 2.2.3, another DSC study by Gaefke et al. [84] shows an exothermic spike above 100°C, which may be attributed to water loss (Figure 2.2.18). Increasing the temperature beyond 170°C results in the breaking of the furan ring of furfuryl

alcohol, evolving CO, CH$_4$ and CO$_2$. Further heating above 460°C results in evolution of H$_2$ and further evolution of CO from the carbonyl bond, resulting in residual carbon.
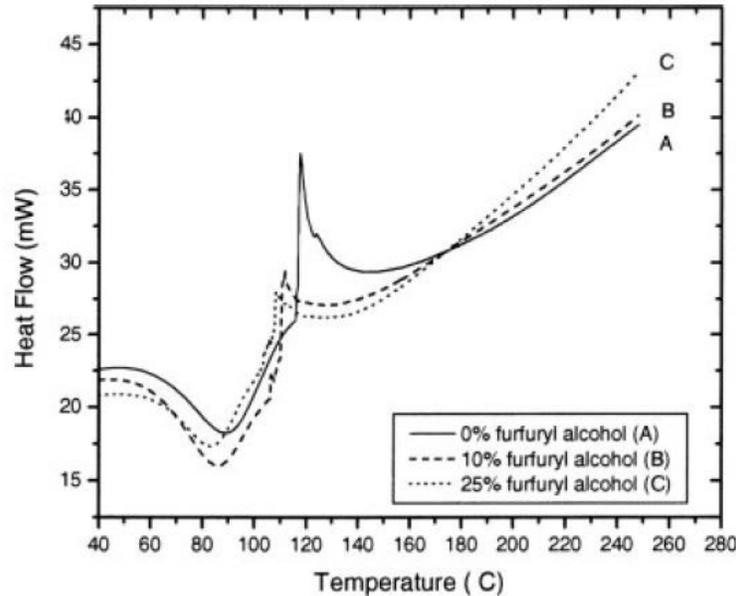
Figure 2.2.18: A DSC curve for furfuryl alcohol showing an exothermic spike above 100°C evident of water loss. From Gaefke et al. [84] © 2017 John Wiley and Sons.

2.3   Unconfined Compressive Strength (UCS) Testing

The unconfined compressive strength (UCS) of a material is the maximum stress that a material can withstand in the axial direction under compression. The term "unconfined" means that the confinement stress on the material is zero, therefore, it can also be termed as a uniaxial compressive strength because the compressive force is only acting along one axis. Therefore, UCS can be calculated from:

$$UCS = \frac{P_{max}}{A_o} \qquad (3)$$

where P_{max} [N] is the maximum load at failure and A_o [mm^2] is the initial cross-sectional area of the specimen.

In most cases, the sample is situated on a steel platen that is stationary throughout the test, while a second platen moves downward onto the sample, axially, compressing the sample to failure. Strain gauges can be attached to the sample for accurate recording of stress versus strain

behaviour. An example reading of the UCS on a stress versus strain curve for compression is shown in Figure 2.3.1. ASTM states three ways in which Young's modulus can be taken: the initial portion of the stress-strain curve, the middle (50 %) of the linear portion of the stress-strain curve and the end of the stress-strain curve immediately before maximum stress [85].

The material subject to testing is cut to form a cylinder with a height to diameter ratio of 2:1 to 2.5:1 as per ASTM D7012 [85]. ASTM D7012 also states that for "weakly cemented sandstone" the specimen diameter shall be at least six times the maximum particle diameter" [85].
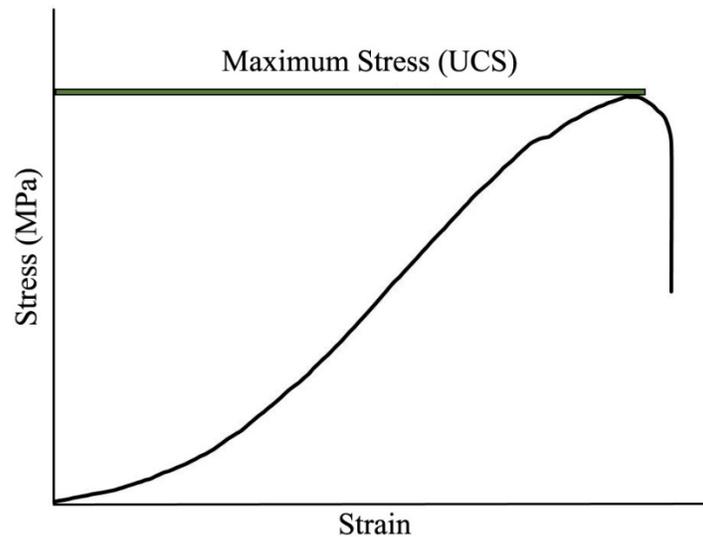
Figure 2.3.1: Illustration showing a stress versus strain curve and how UCS is measured.

2.4   Atomic Force Microscopy (AFM)

In 1982, the first scanning probe microscope was developed by Binning et al. [86] to capture topographic images using a conducting tip and measuring the tunneling current in relation to the sample surface. The technique was later expanded upon in 1986, when the first atomic force microscope (AFM) was used [87]. In general, an AFM operates by using a very small cantilever with a nano-sized tip on the end to make contact and trace the surface of a sample. The deflection of the cantilever is measured by a laser that works in tandem with a piezoelectric scanner to measure the position of the cantilever with nanoscale precision. As the laser is reflected off the end of the cantilever, it is directed into photodiodes that measure a voltage. The voltage difference

is used to create topographic data. The amount of deflection is transmitted to a computer where an image can be produced during rastering of the sample. For this reason, samples subjected to AFM testing must have very smooth surfaces since the largest depth the AFM can image cannot be more than the length of the sharp point on the end of the cantilever, which, in most cases is no more than 200 - 500 μm. An example of an AFM cantilever is shown in Figure 2.4.1, with an example of a topographic surface scan provided by the images in Figure 2.4.2.
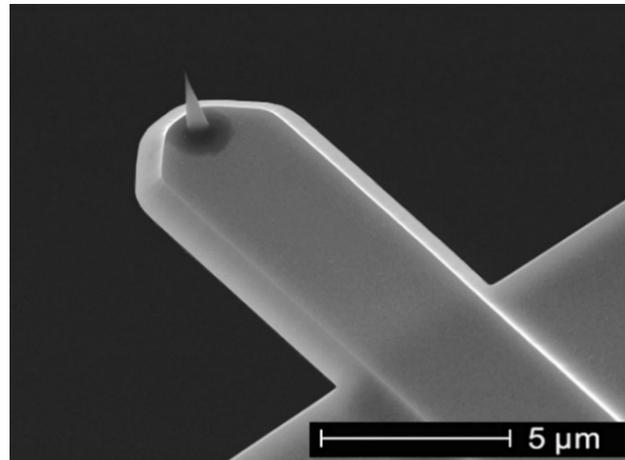
Figure 2.4.1: Image of an AFM cantilever showing the tip used to measure topographic features of a sample. Reprinted with permission [88] © Nano and More.
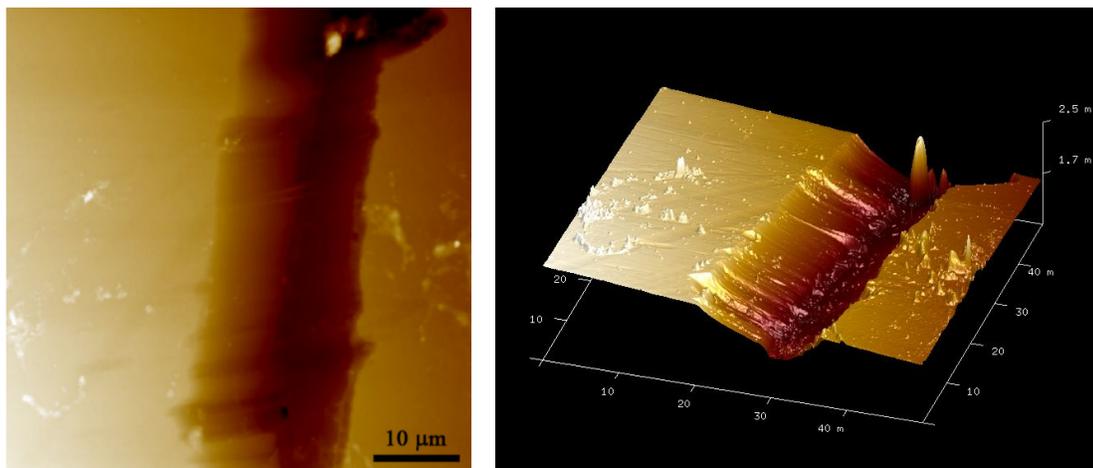
Figure 2.4.2: Left: topographic scan of a 3D-printed binder neck from AFM, with the different shades of brown (representing height) creating a visual image. Right: Same location as the topographic scan on the left, but setup to be viewed in a 3D format via the AFM software.

2.5   Nanoindentation

An indentation testing machine provides the ability to measure the indentation tip depth penetration, h, of an indenter under an applied force, F, throughout the testing cycle. An example of a force versus depth plot is shown below in Figure 2.5.1, where the slope of the curve can be used to determine the indentation elastic modulus (E_{IT}). The only difference between E_{IT} and E, Young's elastic modulus, is the fact that an indenter was used to calculate the value.
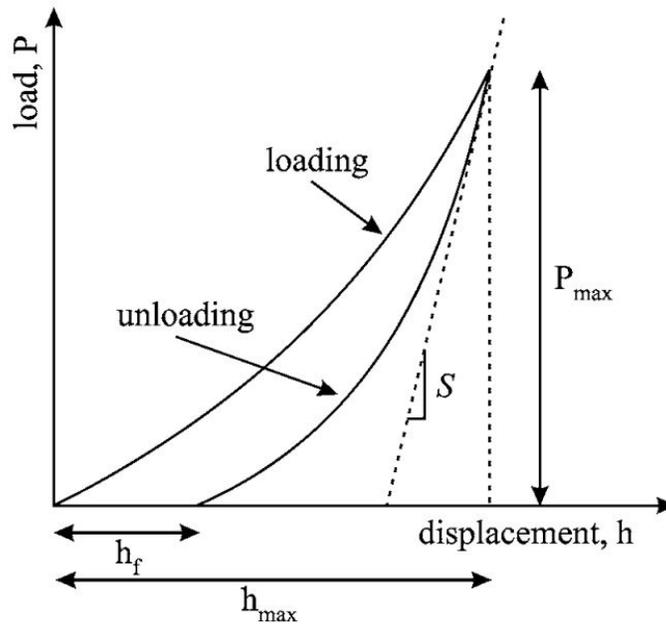
Figure 2.5.1: Schematic of a loading-unloading curve for a nano-indentation measurement where P_{max} is the load at maximum indentation, h_{max} is the indenter displacement at peak load, h_f is the final depth of the contact impression after unloading and S is the initial unloading stiffness. Figure reprinted with permission from Mussert at al. [89] © 2017 Springer.

In order to determine E_{IT} a series of equations are used based on Hertzian contact models and the relationship between load, depth and contact area introduced by Sneddon [90]. Sneddon's equation [90] provides a simple relationship between load and displacement:

$$P = \alpha_o h^m \qquad\qquad (4)$$

where P [N], is load, h [nm], is the displacement and α_o and m are constants. Oliver and Pharr [91] improved upon the equation by including the final unloading depth, h_f [nm] as shown below:

$$P = \alpha_o(h - h_f)^m \qquad (5)$$

As a sample is indented, load and displacement are measured to produce the curve shown in Figure 2.5.1. Eq. 5 models the unloading curve of Figure 2.5.1 through a power law function and the derivative of Eq. 5 provides a model that describes the contact between the indenter tip and sample, which allows for the determination of mechanical properties [91]. Sneddon's [90] solution for elastic contact utilizes the slope of the unloading curve at maximum load to define the contact stiffness, S:

$$S = 2aE_r = \frac{2}{\sqrt{\pi}} E_r \sqrt{A_o} \qquad (6)$$

where a [nm], is contact radius of the tip, A_o [nm^2], is the projected area of the elastic contact, and E_r [GPa] is the reduced modulus that can be calculated by:

$$\frac{1}{E_r} = \frac{(1 + v^2)}{E_{IT}} + \frac{(1 + v_i^2)}{E_i} \qquad (7)$$

where E_{IT} [GPa] and E_i [GPa] are the indentation elastic modulus of the sample and the Young's modulus of the indenter, respectively, and v and v_i are their respective Poisson rations [92]. Therefore, if the properties of the indenter are known and the sample's Poisson's ratio can be estimated, then the indentation elastic modulus (E_{IT}) of the sample can be quantified.

The model described above assumes that testing is done under ideal conditions, but that is not the case during most testing. During such small measurements, load frame compliance and a "tip area function" must be accounted for [93]. Luckily, Oliver and Pharr [91] addressed the issue of load frame compliance by defining the sample and load frame as a series of two springs, thus the total compliance is simply the summation of the compliance between the load frame, C_f, and sample, C_s as per Eq. 8 below:

$$C = C_f + C_s \qquad (8)$$

The sample compliance is simply the inverse of S (Eq. 6) with the total compliance equal to the slope of the load versus displacement curve [91]:

$$\frac{dP}{dh} = C_f + \frac{\sqrt{\pi}}{2E_r}\frac{1}{\sqrt{A_o}} \qquad (9)$$

In addition to compliance, there are other assumptions that must be addressed such as tip rounding and creep under load. To address tip rounding, a tip area function can be calibrated as described by Tranchida et al. [94]:

$$A_0(h_c) = 24.5h_c{}^2 + B_1h_c + B_2h_c{}^{1/2} + B_3h_c{}^{1/4} + \cdots \qquad (10)$$

where h_c [nm] is the contact depth. Eq. 10 can be solved through calibration of a reference material. Creep (or the viscoelastic response) can be addressed by introducing a hold pattern between indentation loading and unloading where the creep rate can be measured.

2.6 Functionalization of Silica Sand

Silane coupling agents (SCAs) are synthetic compounds with an organic and inorganic component, meant to promote adhesion between dissimilar materials. SCAs are particularly well-suited for bonding silicate materials due to their silicone functional groups coupling with hydroxyl groups on the silicate surface [95], [96]. Since the binder used during 3D printing of sandstone is an organic polymer, it has difficulty adhering to silica sand due to the lack of chemical bonds able to form with the surface, therefore, the adhesion relies on mechanical bonding. However, the silica sand grains are rounded and smooth, which can be detrimental to mechanical bonding. To increase adhesion, chemical bonds can be added via treatment of the silica sand surface with a SCA to promote coupling with 3D-printed binder molecules. A schematic of a SCA interacting with an organic and inorganic surface is provided below in Figure 2.6.1.
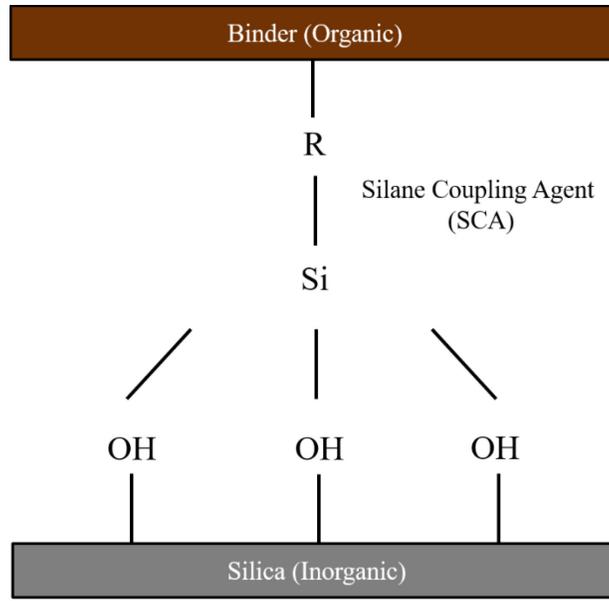
Figure 2.6.1: Schematic illustration showing how a SCA uses a reactive, organic molecule to adhere to an organic surface and the hydroxyl molecular groups to adhere to inorganic surfaces.

3   Experimental

3.1   Design of Experiments

In order to meet the objectives of Section 1.3 multiple experiments and characterization techniques were employed. A brief summary of the experiments along with their expected outcome is provided below in Table 3.1.1.

Table 3.1.1: Summary of testing and characterization methods used in the study of 3D-printed sandstone.

Sections	Experimental Technique	Outcome or Purpose
3.2	• 3D-Printing	• Fabricate samples
4.1 – 4.3	• Stereo microscopy • Optical light microscopy • UV light microscopy • Scanning electron microscopy	• Visualize sand particle morphology • Capture binder neck morphology • Determine location and ease/difficulty of separate phases (binder, silica, epoxy)
4.1 – 4.3	• Fourier Transform Infrared (FTIR) Spectroscopy • X-ray Diffraction (XRD)	• Determine main molecular constituents of binder • Determine if silica sand was crystalline or amorphous
4.4	• Thermogravimetric analysis	• Calculate volume fraction of binder at different binder set points during printing
4.6	• Unconfined Compressive Strength (UCS) testing	• Determine maximum average compressive strength of printed material (before and after silanization)
5.2 – 5.3	• Atomic Force Microscopy (AFM) • Nanoindentation	• Determine the elastic moduli of 3D-printed binder necks on printed samples • Third-party testing to support AFM findings
6.2 – 6.4	• Adhesive testing • UCS testing • Silanization	• Attempt to increase UCS of 3D-printed sandstone by increasing the adhesive strength of the binder and silica sand
7.5	• PFC^{3D} software	• Simulate UCS testing of sandstone using elastic modulus parameters acquired through AFM and nanoindentation

3.2   3D Printing

An M-Flex Sand Printer (ExOne, PA, USA) was used to fabricate the model sandstone in this study. The whole grain silica sand, binder and activator used in the fabrication of the samples was purchased from ExOne and their materials preparation protocols were followed. An illustration of the printing process can be found below in Figure 3.2.1 with representative printed samples in Figure 3.2.2. For printing, 3.5 kg of sand was added to a stand mixer (KitchenAid, ON, Canada) followed by the addition of 5 mL of p-toluene sulphonic acid (activator) while mixing the sand at low speed for approximately two minutes to coat the sand particles. The acid-coated sand was then added to a hopper at the top of the M-Flex printer. The hopper deposited the sand into a vibrating spreader (recoater) where upon it was tamped as it moved along the axis parallel to the job box, providing a layer of silica sand approximately 250 µm thick for printing (the job box is a steel container with a platen free to move in the axis normal to the sand layer). The platen drops a specified distance after each layer, allowing a new layer of sand to be deposited by the recoater. In addition to sand spreading, the print head jets furfuryl alcohol (binder) onto the sand layer while moving along the X and Y-axis, following the pattern of the digital file pre-loaded onto the M-Flex computer. Polymerization of the furfuryl alcohol (FA) takes place when the binder comes into contact with the activator on the sand, creating polymer necks of PFA between sand grains and solidifying the sand in place. It is assumed that there is no concentration gradient between the outside (shell) and inside (core) of the individual layers. Once the layers are completed and the parts have been printed, the job box is removed without disturbing the samples and placed into a large oven set to 80 °C where they are left for 24 hours. 80ºC was found to be the optimum curing temperature for mechanical properties of 3D-printed sandstone by Primkulov et. al. [15] and accelerates the curing process and helps reduce evolved moisture in the parts from the condensation reaction during polymerization [70], [72]. Afterwards, the samples are removed and cleaned with a wire brush to remove any loose sand.

A computer model is transferred to the M-Flex's internal computer for 3D slicing

5 mL of sulphonic acid is mixed with 3.5 kg of quartz sand and added to the M-Flex hopper, which is replenished multiple times during a print

1. The platen is lowered by 250 μm followed by the prepared sand mixture being transferred to the Recoater by the M-Flex.

2. The Recoater travels along the Y-axis in order to deposit and level a layer of sand.

3. A printhead jets binder on the layer of sand creating a 2D image of a single slice from the 3D model loaded earlier into the M-Flex

The process repeats until the part has been completed.

Figure 3.2.1: Illustration of the binder jet additive manufacturing process showing the main steps including modelling, preparation of sand media, layering and binder jetting.

Figure 3.2.2: Photograph of 3D-printed samples fabricated on the M-Flex sand printer.

Although 3D-printing parameters such as activator concentration, recoater speed and deposition rate of sand on the M-Flex machine were left at their default setting in order to study the limitations of the process, other students ran studies in parallel with this thesis that altered several parameters. Specifically, Juan Sebastian Gomez is studying the relationship between layer thickness and build orientation on mechanical properties of 3D-printed sandstone. Secondly, Nathalia Angulo is studying how different printing parameters affect the wettability of 3D-printed sandstone. Additionally, Marzieh Salami is studying the shear properties of 3D-printed sandstone. Lastly, Xiaoyan Teng is using high speed videography and computer simulation to capture crack propagation in 3D-printed sandstone.

3.3   Unconfined Compressive Strength (UCS) Testing of Printed Samples

UCS tests of 3D-printed cylindrical samples 25.4 mm tall and 12.7 mm in diameter were fabricated and placed on a modified desktop tensile tester (PASCO, ME-8236, CA, USA) with 25.4 mm compression platens (PASCO, ME-8247, CA, USA). A stepper motor (SureStep 1288 oz-in, Automation Direct, GA, USA) was added to the tensile tester to allow for a constant strain rate of 3 mm/min [97]. The strain rate was chosen due to the capability of the testing apparatus

and it has been shown that strain rate has little effect on Young's modulus or peak strength for dry, porous materials [98]. However, it is unknown whether strain rate has an effect on samples containing polymeric materials. All samples were loaded to failure, which was defined as a drop to zero force due to the sample splitting. The maximum force of each sample was converted to stress assuming a circular area (as determined through measuring the diameter in multiple places) and recorded as the UCS.

3.4   X-ray Diffraction (XRD)

Silica sand samples used in the 3D-printing of sandstone were characterized on a Rigaku Ultima IV unit equipped with a D/TEX detector. The XRD pattern was ran with a cobalt tube, (38kV and 38 mA) and an iron K-beta filter. The sample was analyzed at 2 degree two-theta with a step size of 0.2.

3.5   Sample Preparation of 3D Printed Materials for Microscopy and Atomic Force Microscopy (AFM)

For microscopy and atomic force microscopy (AFM), small samples of printed material were back-filled under vacuum with fluorescent-dyed (EpoDye, Struers, 40300002) epoxy (LECO, 811-563-107, MI, USA) and left overnight in a vacuum chamber (pressure = -0.14 MPa) to cure followed by sectioning with a slow speed saw (Diamond resin-bonded, Allied High Tech Products, Tech Cut 4, 6-500, CA, USA). A low speed cutting fluid was used during sectioning (Allied High Tech Products, #60-20110, CA, USA). The epoxy aided in lowering the amount of pullout of sand particles during sectioning and the fluorescent dye allowed for contrast between porosity and binder during imaging under ultra-violet light (UV source; 420 nm source). Samples were ground to 1200 grit, followed by a 3 µm and 1 µm cerium oxide slurry polish. A scanning electron microscope (EVOMA15, Zeiss, Cambridge, UK), optical microscope (Imager.M2m, Zeiss, Cambridge, UK) and stereo microscope (Leica EZ4HD and Leica M125, Wetzlar, Germany) were used to capture digital images of the samples. To achieve an even smoother surface, samples exposed to AFM testing were ion milled (Fischione, 1060 SEM Mill, Export, PA) at an angle of 3 degrees for 3 hours under continuous rotation.

3.6   Atomic Force Microscopy (AFM)

An atomic force microscope (Bruker, Dimension Edge AFM, MA, USA) was used to perform indentation on control samples and the binder necks at multiple locations. The control materials were acrylonitrile butadiene styrene (ABS), acrylic or poly(methyl methacrylate) (PMMA), high impact polystyrene (HIPS), polyethylene (PE), polypropylene (PP), polyether-ether-ketone (PEEK), polyamide-imide (PAI -Torlon 4203, Torlon 4301) and indium. The ABS, PMMA, HIPS, PE and PP samples were acquired from Pasco (Roseville, CA, USA), the PEEK and Torlon were acquired from Johnston Plastics (Edmonton, AB, Canada) and the indium was acquired from Sigma (St. Louis, MN, USA). Three different 3D-printed sandstone samples were used with a binder volume fraction of 4, 6 and 8 vol. % (9 samples total). For the control specimens, 10 indents were made in a line at 3 different locations providing a total of 30 force-displacement curves. For the 3D-printed samples 5 different locations (10 indents) were chosen, providing a total of 450 force-displacement curves. All samples were cut by hand using a small saw from samples prepared using the mounting and polishing procedure described in Section 3.5. The samples measured roughly 10 mm by 10 mm square and 5 mm high. The AFM tip used had a resonance frequency of 325 kHz and an average force constant of 40 N/m (Mikromasch, HQ:NSC15/AL BS, Bulgaria). The approach rate of the AFM tip was 3 μm/sec and a cycle hold time of 1 sec. For calculation purposes, a Young's modulus of 137 GPa and a Poisson's ratio of 0.17 were used since the AFM cantilever was made from silicon [99].

3.7   Nanoindentation

Nanoindentation was performed by Mahdi Dargahi from Anton-Paar (Montreal, QC, Canada) where a TTX-NHT[3] Nanoindentation Tester with a Berkovich indenter was used to obtain force displacement data of the binder phase between silica particles of 3D-printed sandstone. The TTX-NHT[3] system has a minimum force load of 0.1 mN and a depth resolution of 0.01 nm. The samples provided to Anton-Paar were subjected to a maximum load of 3 mN with a loading rate of 6 mN/min and a pause at maximum load for 15 seconds. All indentations were completed under ambient conditions.

3.8   Functionalization of Silica Sand

In order to functionalize the silica sand, different silane coupling agents (SCAs) were selected and tested based on compatibility and availability. The silane coupling agents were purchased from Sigma (ON, Canada) and consisted of (3-aminopropyl)trimethoxysilane (APTMS), dodecyltriethoxysilane (DDTES), hexamethyldisilizane (HMDS) and (3-glycidoxypropyl)trimethoxysilane (GPTMS). The SCA solutions were prepared by following a guideline published by Gelest (PA, USA) for SCAs. Approximately 93 mL of methanol and 4 mL of distilled ultra-filtered water (DIUF) were stirred for two minutes before acetic acid was added to the solution until the pH reading from a pH probe (HACH, HQ40D530, CO, USA) read 4.0. At this point 2 mL of the SCA was added and stirred for ten minutes to allow silanol groups to form. All solutions were prepared under ambient conditions.

To functionalize the surface of the silica sand, 100 mL of the SCA solution was poured and mixed by hand into 2 kg of sand and then spread on an aluminum tray and left for several days in a fume hood to allow the moisture to evaporate. The dry, functionalized sand was then fed through a mesh (212 μm/No. 70, W.S Tyler, Canada) by hand to break up any agglomerates.

3.9   Cast Samples

To fabricate cylindrical compression samples from functionalized silica sand, 0.257 mL of p-toluene sulphonic acid was added to 180 g (100 mL) of silica sand (whether control or functionalized) and shaken by hand for 1 minute in a sealed container. 8 mL of furfuryl alcohol was then added to the sand and the container was sealed and shaken for an additional minute. The amount of furfuryl alcohol was selected to equal 4 vol. % of the added sand (100 mL) and the amount of acid was equal to a ratio used previously for 3D-printed sandstone [47].

Epoxy (LECO, 811-563-107, MI, USA) was poured into cylindrical molds that were 3D-printed using ABS (MakerBot Replicator 2X, MakerBot, NY, USA). The epoxy was left to cure under ambient conditions for ~24 hours before removal from the 3D-printed molds. Two epoxy molds were then clamped together to form a cylinder and wet, activated sand was pressed into the molds with 0.2 MPa of pressure using a steel bar as a tamping weight, followed by placing the molds in an oven set to 80ºC for ~18 hours to complete any cross-linking of the furfuryl alcohol.

The surface of the molds was slightly textured from the 3D-printing process, but the texture was not observed on the cast samples after curing.

For compressive loading of cast samples a 400 kN load system (INSTRON 5988, UK) was used at a rate of 0.25 mm/min to failure. The maximum force during compressive loading was normalized by initial sample area and recorded as the unconfined compressive strength (UCS) of the samples via Eq. 3.

3.10   Wetting Angle Measurements

For the wetting angle measurements, glass slides were cleaned by rinsing with toluene, acetone, methanol and isopropanol, respectively. The slide was then placed in the silane solution for five minutes, followed by rinsing twice with methanol and curing in an oven set to 80°C for 10 minutes. The wetting angle measurements were taken on a drop shape analyzer (AST Products, VCA Optima, 1020046004, MA, USA) using a 3 µL drop of furfuryl alcohol as the liquid media.

3.11   Adhesion Testing

Two cylindrical AISI 1020 steel stubs measuring 1" in diameter were ground to 1200 grit using silicon carbide grit paper (Allied High Tech Products, CA, USA), followed by a 3 µm and 1 µm diamond polish to provide a mirror finish. The steel adhesive test stubs were treated with the SCA solutions following the same immersion procedure as described above. The steel stubs were then separated by three glass spheres (Z265926, Sigma Aldrich, USA) measuring 3 mm in diameter that had been previously cleaned using toluene, acetone, methanol and isopropanol, respectively. 2 mL of furfuryl alcohol containing 0.1 vol. % of p-toluene sulphonic acid was then injected in between the stub surfaces, wetting completely, followed by curing in an oven set to 80°C for 12 hours and then cooled to room temperature (see Figure 3.11.1 for an example of a completed test assembly). The steel stub assemblies were then installed on a modified desktop tensile tester and pulled to failure. The adhesion test was setup to mimic that of ASTM C633 [100].

For adhesive testing, a desktop 7 kN load system (PASCO, ME-8236, CA, USA) provided tensile force at a crosshead speed of 1.13 mm/min to failure.
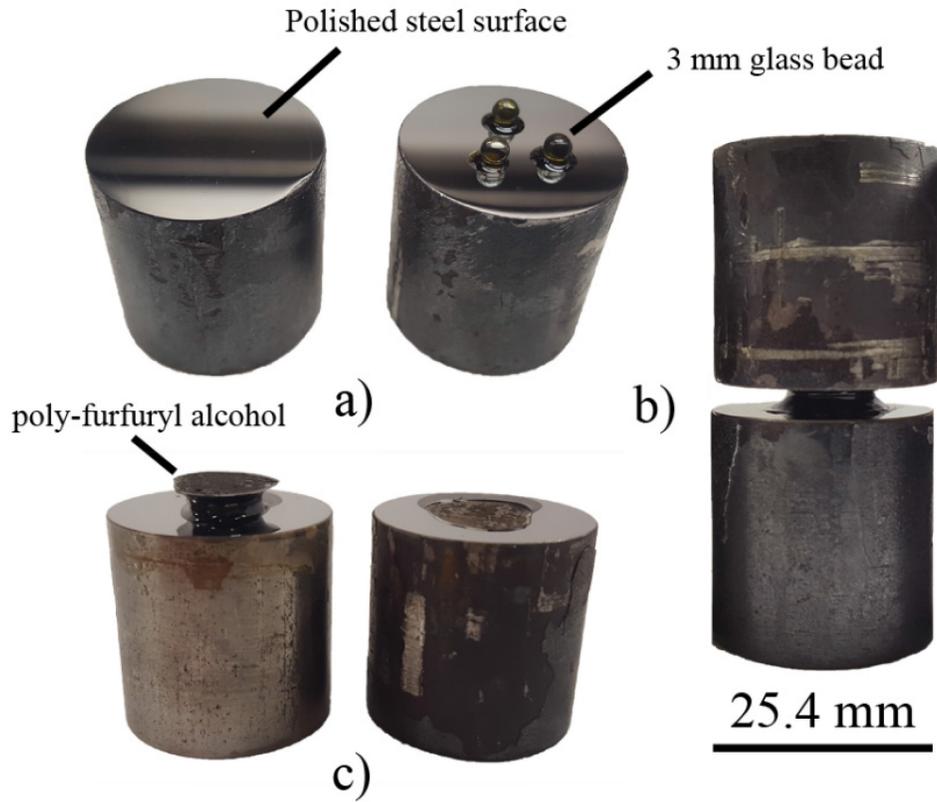
Figure 3.11.1: a) Polished steel adhesive test stubs showing the placement of three 3 mm glass beads for gap separation during curing of poly-furfuryl alcohol; b) a completed adhesive test assembly complete with a PFA neck; c) an adhesive test assembly post failure showing an intact poly-furfuryl alcohol neck.

4 Characterization of 3D-Printed Sandstone

4.1 Binder Characterization

The binder was confirmed to be primarily furfuryl alcohol (FA) through FTIR (Cary 630, Agilent, CA, USA) with minor traces of bisphenol-A and resorcinol as reported by the material datasheet from the supplier (ExOne). The FTIR spectrum is provided in Figure 4.1.1.
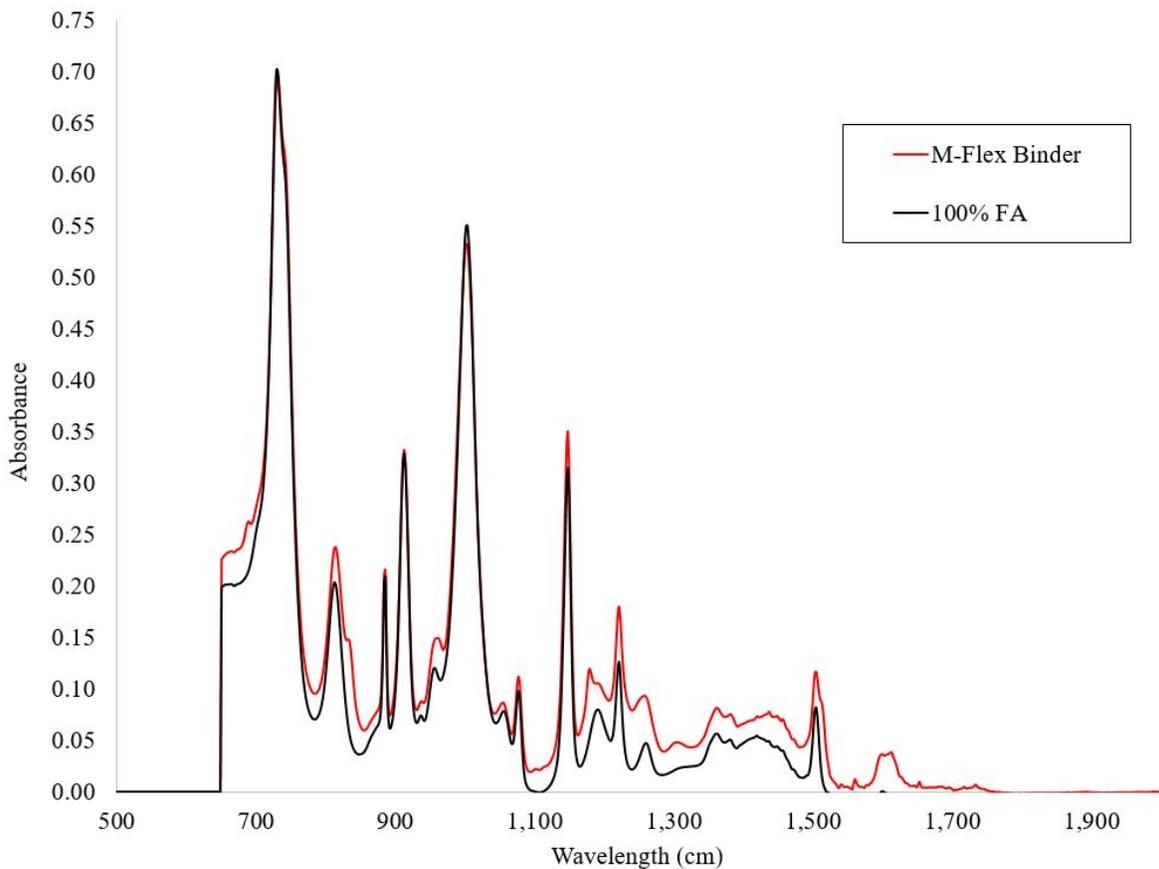
Figure 4.1.1: FTIR spectrum of the M-Flex binder compared to 100 % FA.

4.2 Sand Characterization

The silica sand used was confirmed by XRD to be crystalline and was observed to have a rounded, irregular morphology (Figure 4.2.2). The sand was scanned by x-ray photoelectron spectroscopy (Kratos XPS, NanoFab, Alberta) and the survey scan was analyzed by CasaXPS software to check for any surface contaminants. The sand was tested from the suppliers' container,

without any cleaning or preparation. Minor amounts (< 1 at. %) of Al, K and Mg were detected, although the presence of such elements are common for silica sand [101]. The average diameter of the sand (D_{50}) was reported as 148 µm by a quality control report provided by the supplier.
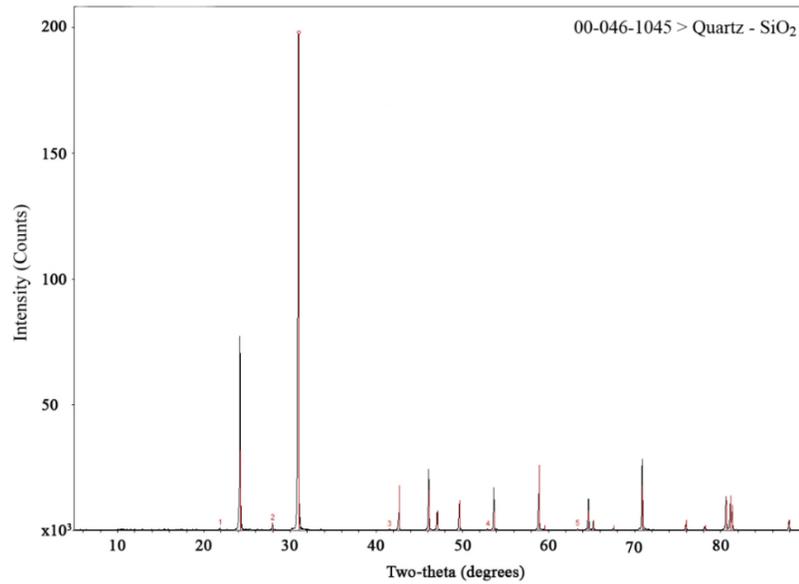
Figure 4.2.1: XRD pattern for the silica sand used to fabricate 3D-printed sandstone, showing a complete overlap of the standard reference pattern for quartz (JCPDS, 46-1045).
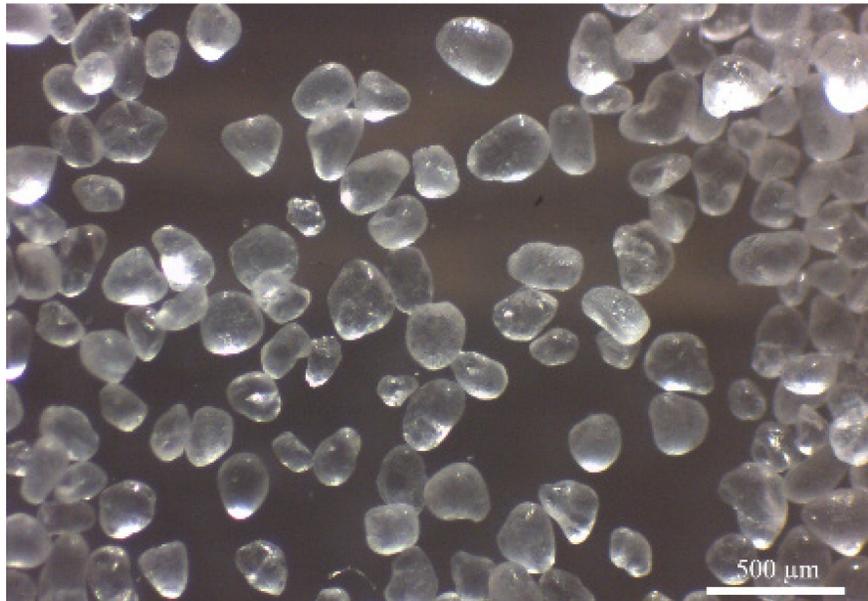
Figure 4.2.2: Stereo micrograph of quartz sand used in 3D-printed sandstone. Note the rounded, irregular morphology characteristic of whole grain silica sand.

4.3   Microstructure

A comparison of natural and 3D-printed sand stone is shown below in Figure 4.3.1. In contrast to the white quartz, the dark color of the printed sample is due to the polymerized furfuryl alcohol binder, which turns black upon crosslinking [72], [102]. Under UV light at high magnification, a typical binder neck between two sand particles can be seen as indicted in Figure 4.3.2. A collage of images comparing natural to 3D-printed sandstone is provided for comparison by Figure 4.3.3, which shows a lower apparent packing factor for model sandstone, evident from the higher amount of back-filled fluorescent epoxy. Additionally, the natural sandstone has increased grain to grain contact area due to the angular nature of the sand grains, compared to the lower contact area caused by the rounded, whole grains of the model sandstone. The UV images of Figure 4.3.3 also highlight the amorphous, polymer binder phase in model sandstone, compared to the crystalline, cemented binding of natural sandstone. It is suggested that due to the reduced contact area between sand grains, 3D-printed sandstone typically has a lower UCS than natural sandstone (almost 1:3 when compared to Berea sandstone [85]).
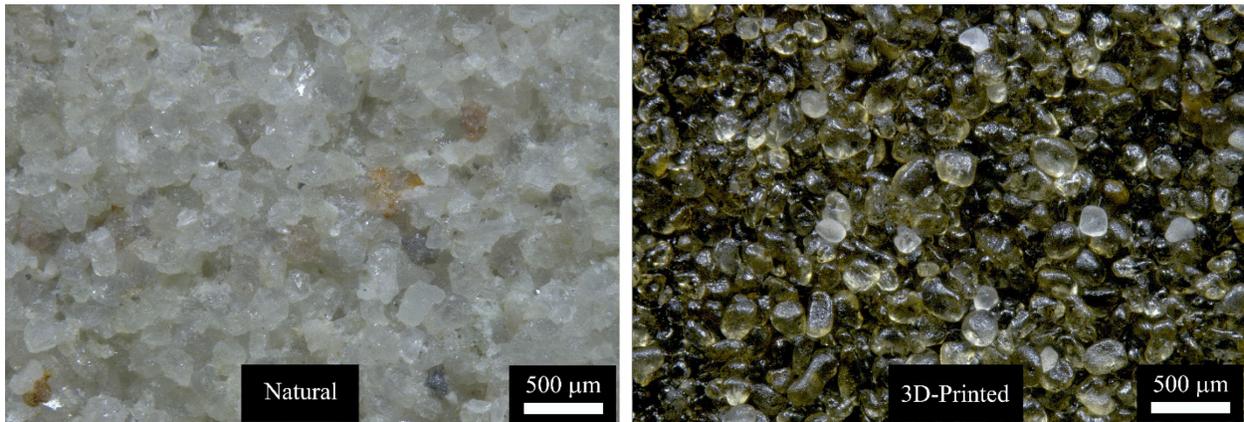
Figure 4.3.1: Natural (Berea) sandstone compared to 3D-printed sandstone. Note the rounded grains and dark color caused by the binder compared to the angular, cemented grains of the natural sandstone.
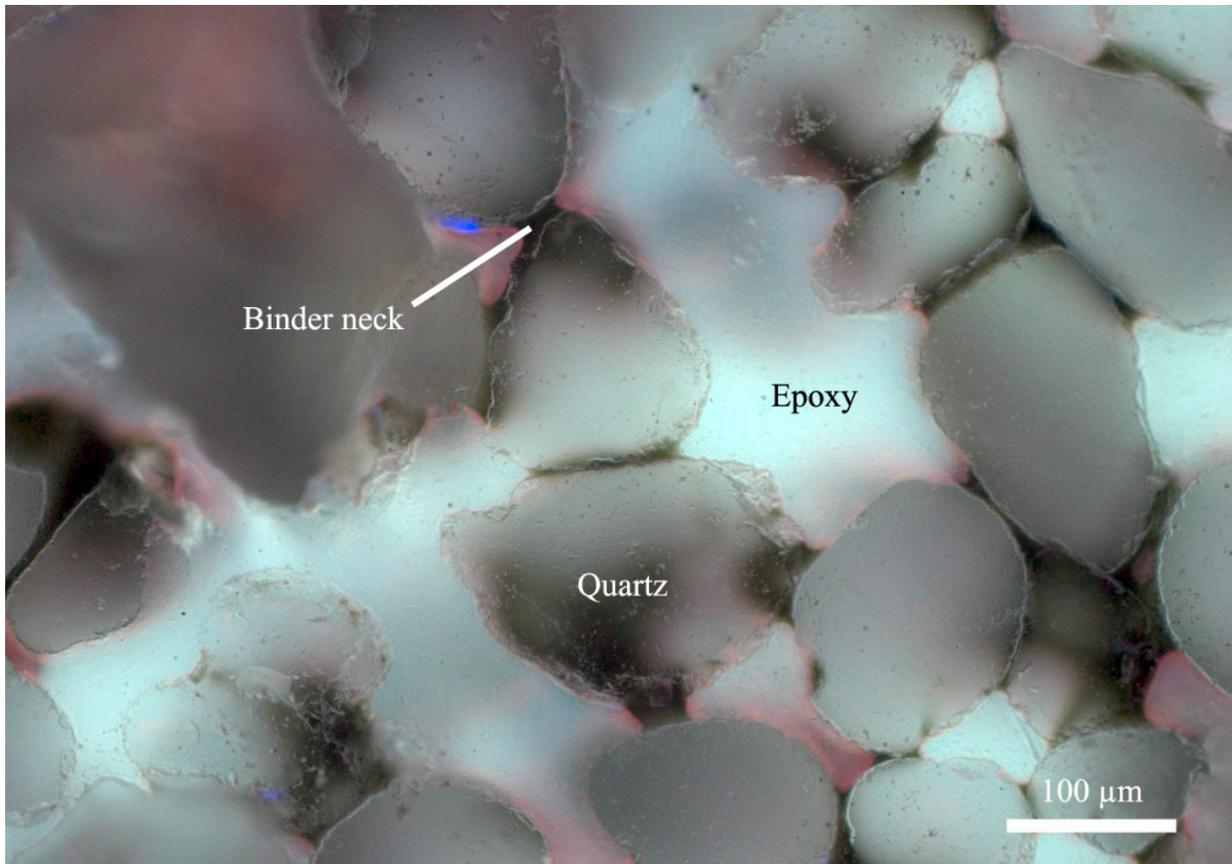
Figure 4.3.2: High magnification optical transmitted bright field image of sand grains within 3D-printed model sandstone. A typical polymerized furfuryl alcohol binder neck indicated. Sample was back-filled with fluorescent epoxy to provide better contrast of the dark binder.

	Natural Berea Sandstone	3D-printed Sandstone
SEM	a)	b)
DIC	c)	d)
UV	e)	f)
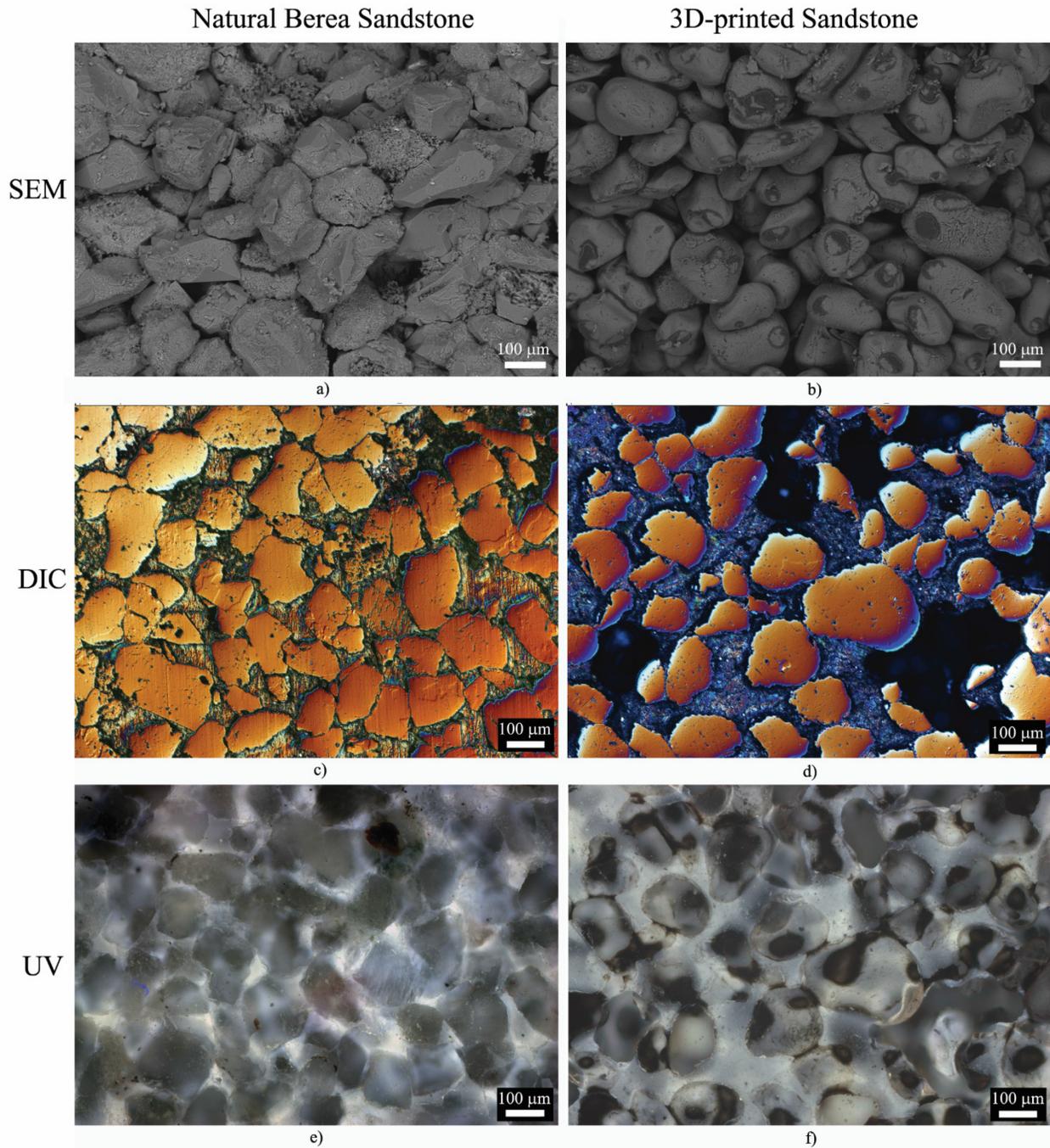
Figure 4.3.3: SEM: scanning electron microscopy; DIC: optical differential interference contrast; UV: transmitted bright field ultraviolet images of natural and 3D-printed sandstone, comparing the apparent packing factor and morphology of the sand grains. The binder phase is visible under UV for 3D-printed sandstone, which can be compared to the cemented silicate bonds of natural.

4.4   Calibration of Binder Volume Fraction

The M-Flex computer assumes a porosity of 40% for loosely-packed sand and deposits enough volume of binder through the print head to fill a percentage of porosity equal to the binder saturation. Therefore, if binder saturation is set to 10%, then 4% of the total volume of the sample should contain binder. In order to generate a binder volume fraction calibration, cylindrical samples printed with increasing binder volume fractions were heated in a furnace at 850 °C for thirty minutes to thermally combust and remove all the binder. Thirty minutes was chosen as acceptable due to the silica sand returning to its natural white appearance without the presence of any dark discoloration due to PFA. The difference in weight from before and after heating was taken on a four-point mass balance and recorded as the mass of binder deposited during printing. Since there is no reported value for the density of cross-linked furfuryl alcohol, the density was selected as the same for its monomer form of 1.13 g/cm^3 [103]. Thus, the volume fraction of binder (V_b) could be calculated via Eq. (15 below, where m_b [g] is the mass of the binder (determined from the burnout procedure) and ρ_b [g/cm^3] is the density of the binder (furfuryl alcohol).

$$V_b = m_b \rho_b \qquad\qquad (11)$$

The calibration curve below in Figure 4.4.1 shows that the binder volume fraction achieved is only ~70% of the set binder volume fraction. However, the binder volume fraction follows a linear relationship with set binder volume fraction, allowing the different binder volume fraction levels to be compared directly in this study (the actual binder volume fraction was found to have a calibration factor of 1.5 times the set binder volume fraction). Therefore, the binder volume can be estimated by:

$$V_b^{calc} = 1.5 V_b^{set} \qquad\qquad (12)$$

where V_b^{calc} is the volume fraction of binder estimated within the sample and V_b^{set} is the volume fraction of binder set by the M-Flex computer.
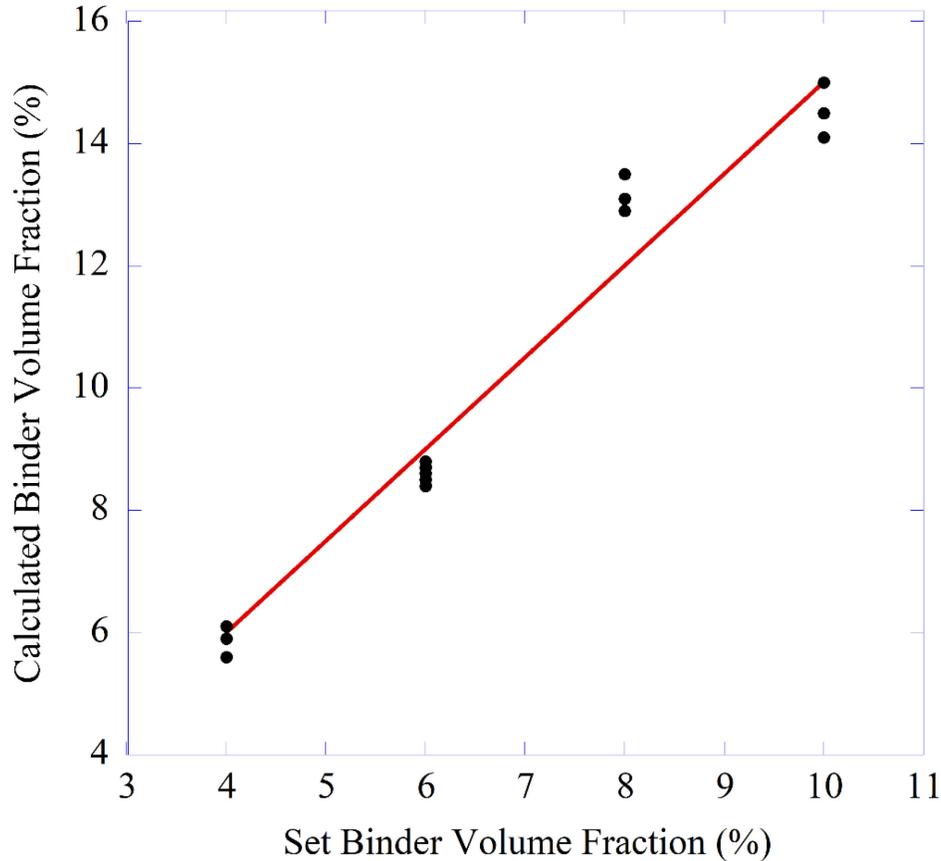
Figure 4.4.1: Binder saturation calibration curve showing the offset from set binder volume fraction compared to calculated binder volume fraction for the specimens (N = 5).

4.5   Effects of Binder Content – Spatial Gradient and Dimensional Control

When increasing the set binder beyond 8 vol. % a "bleeding" and/or "pooling" effect was observed on the bottom of the samples. An example of bleeding and pooling is shown in Figure 4.5.1 below, where the bottom of the sample (printed first) is subject to bleeding. The bleeding effect was most likely pooling of binder due to gravity during printing, since the bleeding accumulates at the bottom of the samples. The pooling effect could be due to the lack of porosity, but epoxy was successfully infiltrated under vacuum with a binder volume fraction > 12 vol. %. The effect was more severe for higher binder saturations. The pooling of binder at the lower end of the sample suggests heterogeneity of binder distribution. To test the distribution of binder saturation, a sample from each binder volume fraction was cut into four sections as per Figure 4.5.1, followed by the burnout procedure described previously in Section 4.4 and plotted below in

Figure 4.5.2. In all cases there was a slight increase in binder content at the bottom of the sample, but was considerably worse for the samples with binder saturation greater than 8 vol. %. It has been published elsewhere that the M-Flex machine is capable of printing defects within 1 mm in size (anything smaller and the defects close due to capillary effects of the binder) [47]. However, as the binder saturation increases, even large fractures can close during printing due to bleeding of the binder through the sand. An example is shown below in Figure 4.5.3, where the same model was printed with various binder saturations and compared visually. Therefore, increasing the binder volume fraction above 8 vol. % will reduce porosity, but more critically has detrimental effects on dimensional control. At binder volume fraction greater than 8 vol. %, dimensional instabilities were observed, including bleeding and pooling of the binder after printing, which implies the maximum possible volume fraction of binder was exceeded.
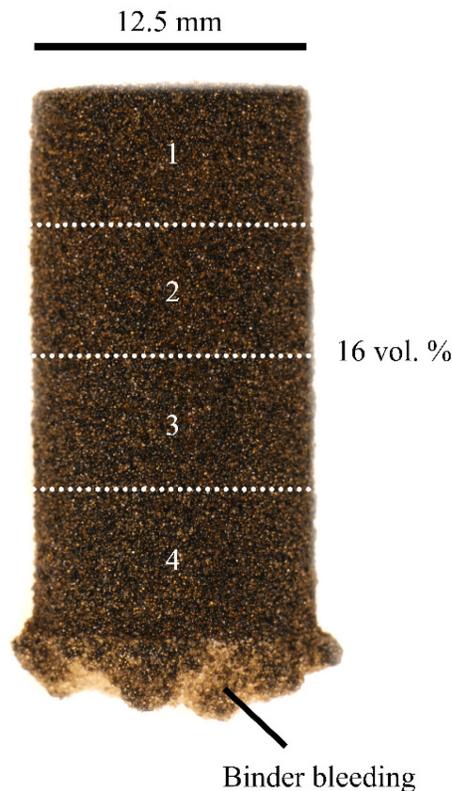
Figure 4.5.1: 3D-printed sandstone fabricated with 16 vol. % of binder. Bottom of sample contains a large amount of bleeding as indicated by the arrow. Dashed lines represent different sections used for burnout procedure.
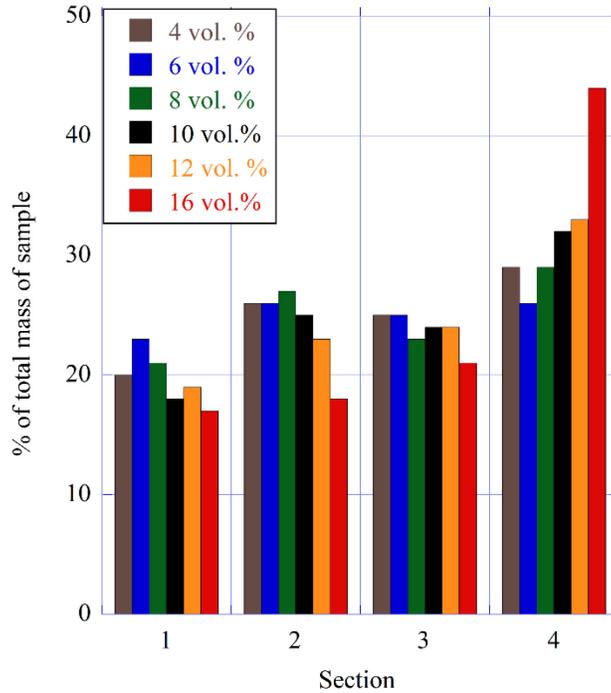
Figure 4.5.2: Average total mass of binder versus section of the sample, showing an increasing amount of binder mass retention at the bottom end of the samples (Section 4) for higher volume fractions of binder.
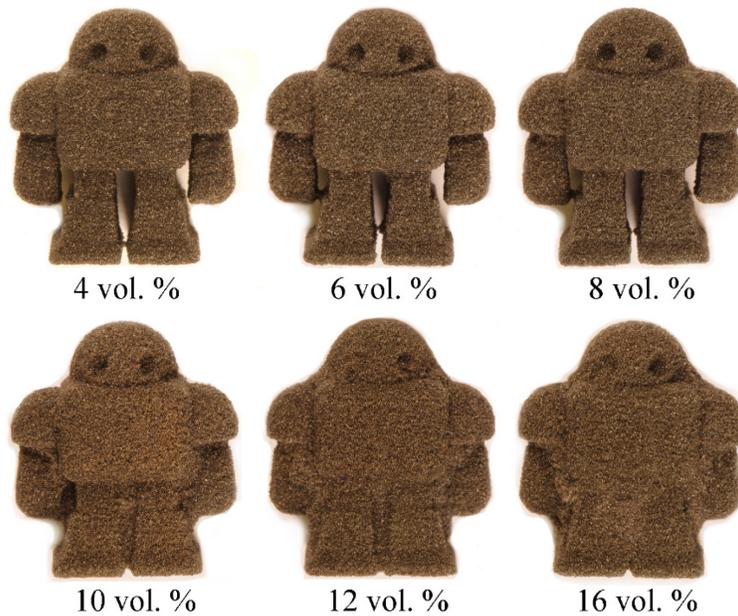
Figure 4.5.3: 3D-printed sandstone models [104] using increasing amount of binder saturation. As binder volume fraction is increased, dimensional control and fidelity is lost on the model, specifically spaces between the arms and legs of the robot.

4.6   Unconfined Compressive Strength

To test the effect of binder saturation on UCS, cylindrical test samples were fabricated and placed in compression to failure. At least 20 samples were tested from each binder saturation level. In most cases the characteristic "end cone" of UCS testing can be observed, which is due to the end effect of compressive loading; the end effect is caused by restrained circumferential expansion during compression against the testing platen due to friction [105]. In most cases, axial cracking occurred along the direction of loading, suggesting failure due to tensile stress perpendicular to the direction of loading [97]. Figure 4.6.1 exhibits a typical failure mode compared to natural sandstone.
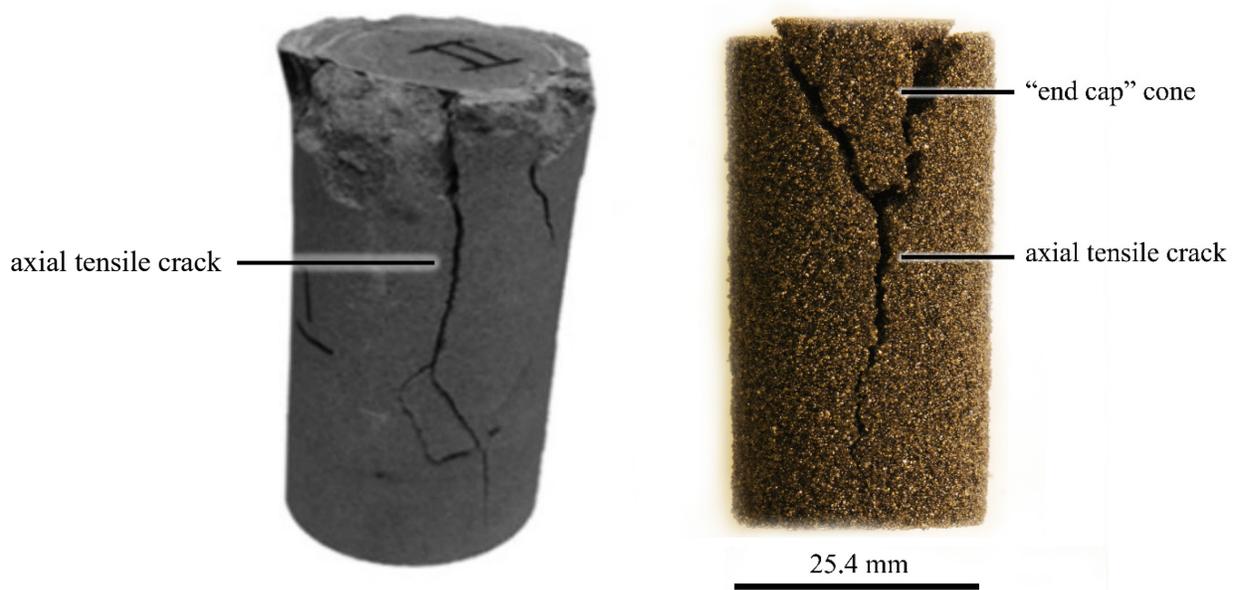
Figure 4.6.1: Left: Photograph of blue sandstone showing axial cracking [106]. Right: Photograph of a 3D-printed UCS specimen after testing. Arrows indicate end cap cone and axial tensile crack. The failure mode is typical of sandstone compression samples when there is friction between the platens and sample faces.

The average maximum stress of each binder saturation was recorded and plotted against actual binder volume fraction in Figure 4.6.2. An increase in binder volume fraction resulted in a higher UCS, as more surface area of the sand was in contact with polymerized furfuryl alcohol, which can be observed through Figure 4.6.3. However, as binder saturation was increased, the strength of the 3D-printed sandstone began to plateau. This plateau may be attributed to the gravity

effect during printing mentioned earlier, where the binder drains towards the bottom of the sample, resulting in a heterogeneous binder distribution. Another explanation may be the limitations of the manufacturing process itself. When the sand is deposited to form a layer to be printed upon, the sand falls from a travelling hopper due to vibratory effects and settles due to gravity. Although there is a minor tamping effect from the hopper, the sand is most likely not at optimal packing (see Figure 4.3.3), producing a large amount of porosity before printing. Due to the porosity of the sand, the liquid binder will infiltrate and begin to neck due to capillary mechanisms on neighbouring grains. However, once the liquid binder comes into contact with the acid, polymerization takes place almost immediately to crosslink the binder into a black, glassy solid. The loose packing and short gelation times may cause the possibility for long binder necks to form, where the compressive strength of the sandstone is now dependent on the binder itself, versus the addition of internal friction from neighbouring sand particles impinging on one another under stress.
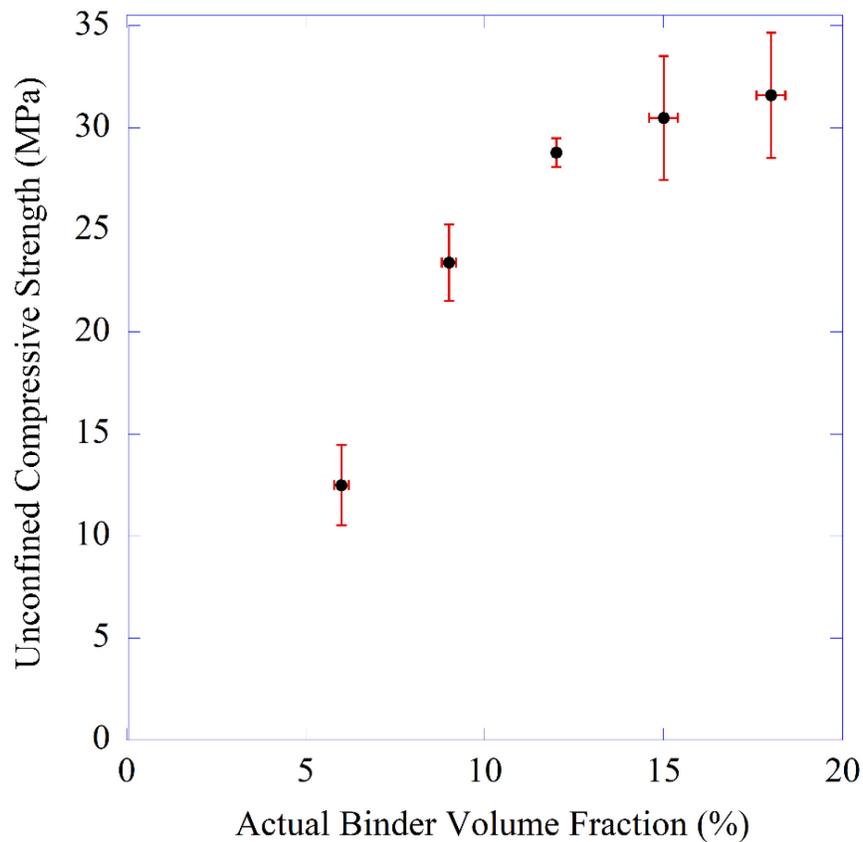
Figure 4.6.2: Unconfined compressive strength (UCS) versus actual binder volume fraction for 3D-printed sandstone. Sample size is a minimum of ten for each data point.
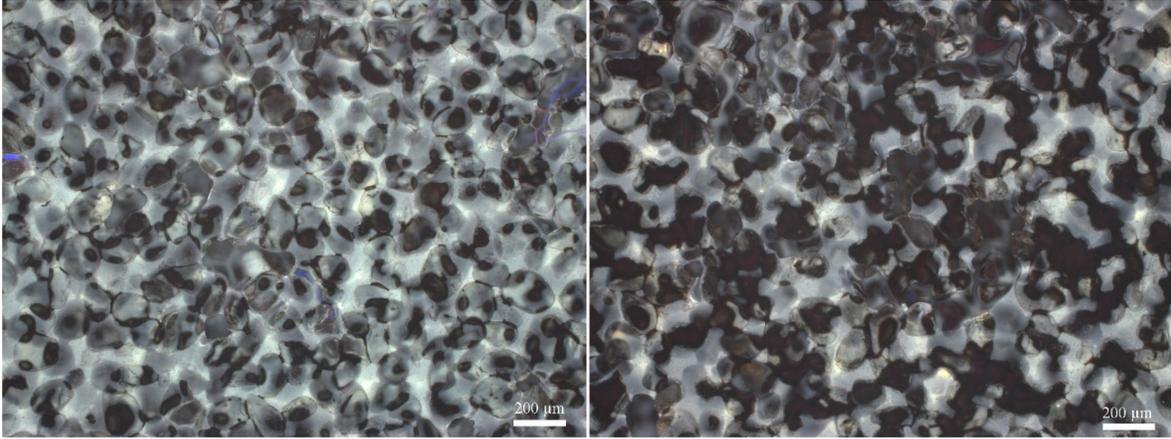
Figure 4.6.3: 3D-printed sandstone micrographs under UV light fabricated with a set binder fraction of a) 4 vol. % and b) 12 vol. %. The increase in binder volume fraction can be observed by the increase in the darker phase of the material during imaging.

4.7 The Relationship Between Young's Modulus and Binder Volume Fraction

It has already been established that the volume fraction of binder used to fabricate 3D-printed sandstone can be increased to achieve a higher UCS (Figure 4.6.2), but is the Young's Modulus of 3D-printed sandstone effected? To answer this question, the Young's modulus was measured from several UCS tests and plotted against its actual binder volume fraction (Figure 4.7.1). The Young's moduli was calculated by taking the slopes of the stress versus strain curves at 50% of the linear portion of the curves as per ASTM [85]. Although this method of calculating Young's modulus is not as accurate as it would be if strain gauges were used, the purpose was to determine if an overall trend was apparent. It was found that the Young's modulus of the 3D-printed sandstone increased sharply with increasing amount of binder, followed by a plateau around 1.3 GPa. The data was analyzed via two tail t-tests (Appendix A-1) where it was found that the data approaches critical t-values between data points with increasing binder volume fraction until they are no longer significantly different ($\alpha = 0.01$). The plateau can be explained by referencing Sections 4.3 and 4.5, where it was shown that 3D-printed sandstone is a porous structure that is susceptible to the detrimental effects of pooling and bleeding when high enough volume fractions of binder are jetted into a sample. Therefore, not only is there a UCS limit to 3D-

printed sandstone through traditional binder jetting techniques, but a Young's modulus limit as well.
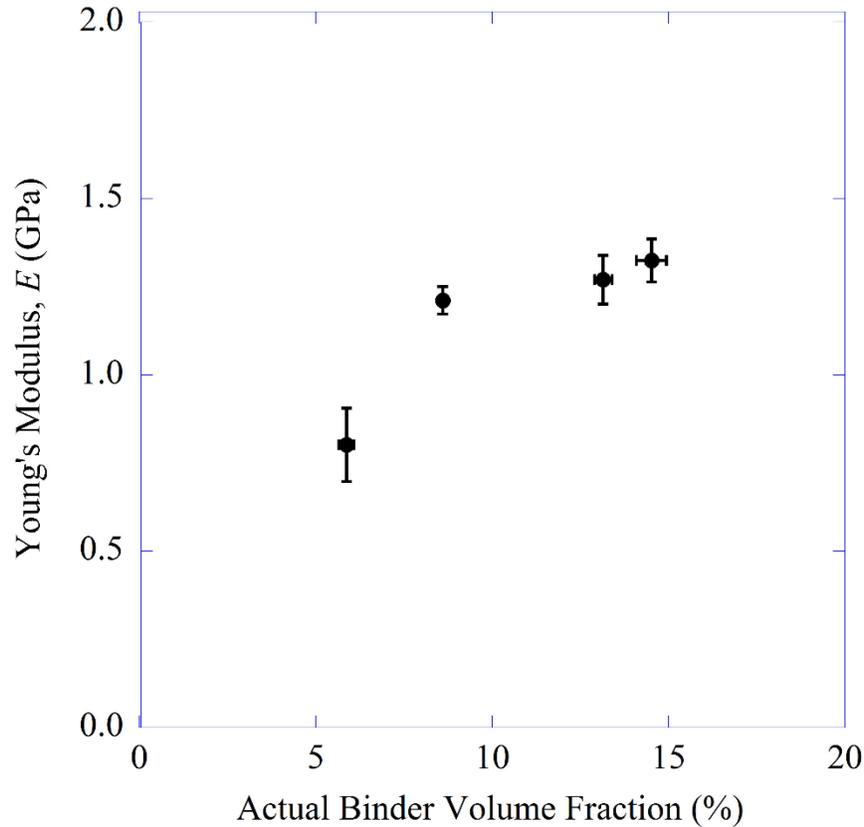
Figure 4.7.1: Young's modulus, E, of 3D-printed sandstone versus actual binder volume fraction. N = 9 for 6 vol. %, N = 19 for 8 vol. %, N = 20 for 13 vol. % and N = 19 for 15 vol. %.

It must be acknowledged that the values reported above for Young's modulus are less than the Young's modulus reported elsewhere for the same material (~1.9 GPa [15]), which may be explained through the difference in testing equipment. Primkulov et al. [15] performed UCS tests on a large, 400 kN load system (INSTRON 5988, UK), while the UCS tests for the 3D-printed sandstone in this study was performed on a smaller, less stiff, 7 kN load system (PASCO, ME-8236, CA, USA). It is suggested that the difference in machine compliance and stiffness would provide underestimated Young's moduli values. However, the trend of Young's modulus

increasing and plateauing with binder volume fraction should still exist, theoretically. In order to understand fully the relationship between binder volume fraction and Young's modulus of 3D-printed sandstone, an attempt to model the data presented in Figure 4.7.1 will now be discussed.

The first attempt at fitting the data from Figure 4.7.1 was to use the rule of mixtures for isotropic strain (Eq. 13 - Voigt [107]) and isotropic stress (Eq. 14 - Reuss [108]):

$$E = V_A E_A + V_B E_B \qquad (13)$$

$$\frac{1}{E} = \frac{V_A}{E_A} + \frac{V_B}{E_B} \qquad (14)$$

where E is Young's modulus, V_i is the volume fraction of the phase and E_i is the Young's elastic modulus of the phase. However, Eqs. 13 and 14 only allow for two phases, while 3D-printed sandstone contains three (sand, binder and air). A third term may be added to Eqs. 13 and 14 to account for the third phase (air), but since the Young's modulus of air is zero, the terms are dropped. Due to this, the Voigt and Reuss rule of mixtures for composites does not accurately reflect the physics of 3D-printed sandstone.

Basaran et al. [109] have presented a micromechanical model for the effective Young's modulus of three-phase composites based on the theory of inclusions and how differing elastic properties effect stress-fields at large distances [110]. The models more closely resemble the data of Figure 4.7.1, due to the fact that a "interface parameter" has been introduced, which describes the interface region between particle and matrix [109]. As the interphase region between particle and matrix is decreased, the composite will approach values of E that are demonstrative of a perfectly bonded composite [109]. The model more closely resembles the physics governing the elastic behaviour of 3D-printed sandstone, but there are a few conflicting assumptions that cannot be over-looked. The model presented by Basaran et al. [109] for a three-phase composite is for tension and they admit that the translation to compressional forces is "difficult" and unknown. Additionally, although there is an interphase region in 3D-printed sandstone (binder) between one

phase (silica sand) and another phase (air), it does not encompass the entire sand particle (Section 4.3). Therefore, we not only have to include a thickness parameter to the film of interphase region surrounding a particle, but there is also a diameter, length and/or ratio of surface area coverage of the particle that would need to be introduced. Also, several other parameters would need to be studied that control the shape of 3D-printed binder necks. Figure 4.7.2 contains an illustration from a capillary study between two spherical studies that highlight the complexity of variables that must be understood in order to develop an interface parameter for 3D-printed sandstone [111]. An example of the interphase region proposed by Basaran et al. [109] and the interphase region of 3D-printed sandstone is contrasted in Figure 4.7.3.
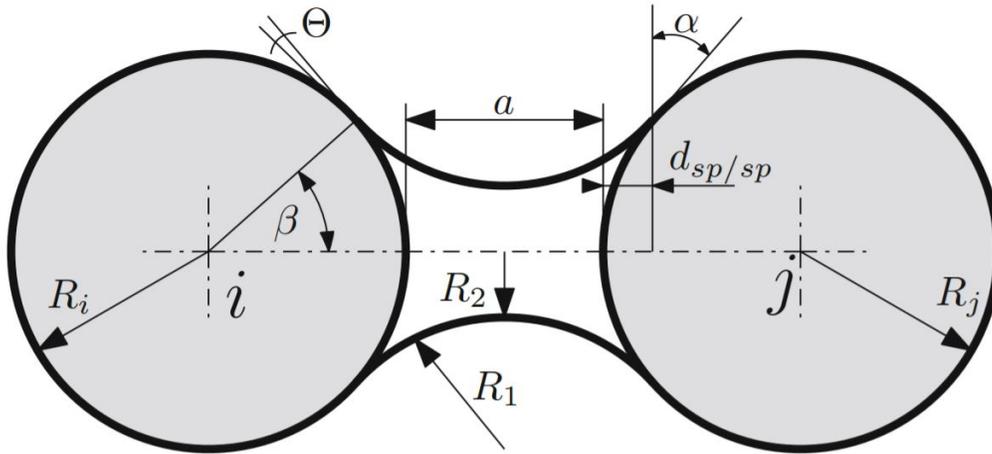
Figure 4.7.2: Illustration highlighting the variables between particle shape and distance in relation to necking dimensions of a liquid. Reprinted with permission from Gladkyy et al. [111] © 2017 Springer.
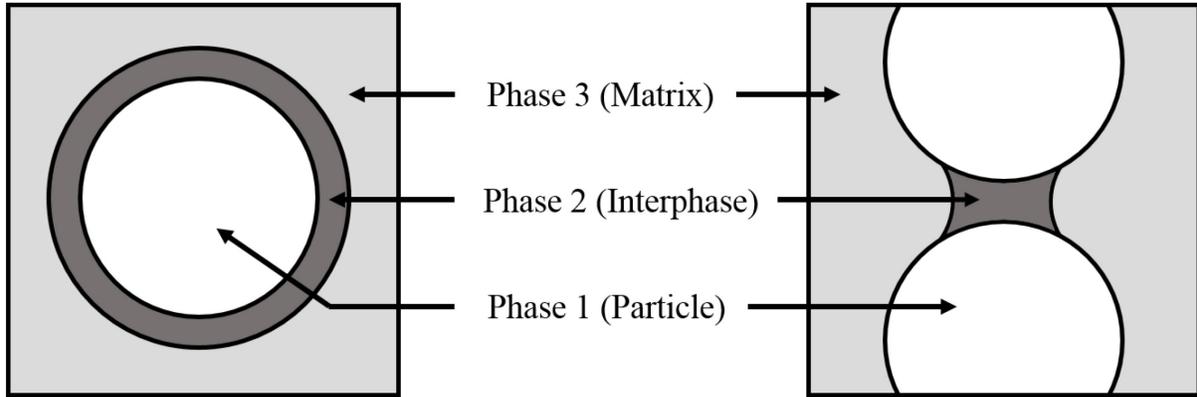
Figure 4.7.3: Interphase region as described by Basaran [109] compared to the proposed interphase region of 3D-printed sandstone. For the case of 3D-printed sandstone the matrix phase would be air.

A simple polynomial was fitted to the data in Figure 4.7.1 and is described by Eq. 15 (Figure 4.7.4). It is suggested that the general form of Eq. 15 could be described by Eq. 16, where one of the coefficients is, coincidently, the same as the Young's modulus for silica. The upper bound of Eq. 16 is shown in Figure 4.7.4 since above 15 vol. % the curve begins to decline.

$$E = 18.8V_b - 67.4V_b^2 \qquad\qquad (15)$$

$$E = KE_bV_b - E_sV_b^2 \qquad\qquad (16)$$

where E is Young's modulus, E_s is the Young's modulus of silica sand and V_b is the actual binder volume fraction. However, the model remains a mathematical expression based on empirical data and is not governed by any micromechanical fundamentals.

$$E = KE_bV_b - E_sV_b^2$$
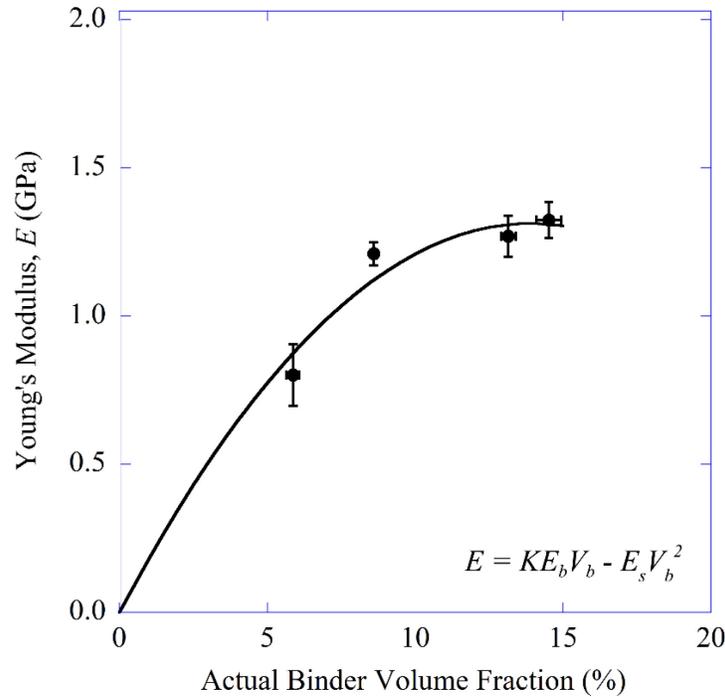
Figure 4.7.4: Young's modulus, *E*, of 3D-printed sandstone versus actual binder volume fraction where a curve has been fitted in an attempt to model the micromechanical response of the binder. K is a yet to be determined parameter that may include variables such as 3D-printed binder neck diameter, length and surface area coverage.

It is suggested that a strong relationship exists between 3D-printed binder neck dimensions and Young's modulus. As the binder volume fraction of 3D-printed sandstone is increased, it is possible that the size of the binder necks increases until a size limit is reached due to surface tensions, liquid properties and particle distance [111]. Due to the nature of binder jetting into a porous semi-infinite particulate field the tendency of liquid binder to pool and bleed never results in the pore space being completely filled by binder (Section 4.5). Hence a practical upper limit of binder volume fraction is reached at a volume fraction much less than the potential fraction of the entire pore space being filled with binder. For example, it has been shown that the volume fraction of sand in 3D-printed sandstone is 53 % [15], but the upper limit of binder volume fraction to prevent pooling and bleeding is up to 15 % – which is approximately a third of the entire pore space available.

In order to accurately model the elastic behaviour of 3D-printed sandstone in relation to binder fraction volume, a few variables need to be removed in addition to further testing being

needed. For one, the silica sand should be replaced with mono-dispersed spherical beads, eliminating the angularity of silica sand. Secondly, the sample size would need to be increased so that strain gauges could be attached for a more accurate measurement of Young's modulus. Lastly, the number of samples would need to be increased dramatically. It is acknowledged that the data presented in Figure 4.7.1 is insufficient to properly calibrate any parameters. Fortunately for 3D-printing the number of samples can be increased easily for future testing.

5   Determination of Cured Binder Elastic Modulus

5.1   Nomenclature of Young's Modulus

The nomenclature for Young's modulus may change depending on the method used to acquire it or the material it is referring to. For clarity, Table 5.1.1 provides a summation of the different Young's modulus terms used in the following sections.

Table 5.1.1: Description of Young's moduli mentioned in the thesis

Term	Name	Description
E	Young's modulus	Relationship between stress and strain in the elastic regime.
Ei	Young's modulus of an indenter	Young's modulus of the material used to fabricate an indenter.
E_r	Reduced modulus	A combination of the Young's modulus between a material and an indenter (Eq. 7).
E_{IT}	Indentation elastic modulus	Synonymous with Young's modulus, but acquired via indentation.
$\bar{E}_c$	Cement elastic modulus	A parameter within PFC^{3D} software describing the elastic modulus of material holding two particles together.

5.2   Determination of Indentation Elastic Modulus (E_{IT}) via Atomic Force Microscopy

Although the primary use for AFM is imaging of nanoscale features, AFM has been implemented as a nanoindenter [94], [112], [113]. To acquire material properties such as the elastic modulus from AFM, contact mechanics and depth sensing indentation (DSI) methods can be utilized [93], [114], [115]. Normally, the shape and contact area of the AFM tip must be known, as well as correcting for thermal drift and creep [93], [115], [116]. However, Tang et al. [92] have devised a way to quantify the elastic modulus of polymers empirically using AFM without determining the contact area or tip radius. The methodology is provided in detail in Tang et al's study [92] and the thesis of Hoffman [93]. The methodology is summarized below for clarity.

The methodology of Tang et al. [92] relies on an empirical relationship between reference materials. The basis is a set of equations based on Sneddon's elastic contact solution [90], which captures the AFM cantilever's stiffness and tip radius into one equation:

$$K = A\left(1 + \frac{\alpha}{E_r}\right) \qquad (17)$$

where A [V/μm] is the cantilever sensitivity , α [GPa] is the cantilever-tip constant, E_r [GPa] is reduced modulus and K [μm/V] is the slope value determined from the linear portion of the unloading phase of a force versus displacement curve [92]. An example of determining K is shown below in Figure 5.2.1, with an example of an AFM image showing a tested binder neck location shown by Figure 5.2.2. Reduced modulus, E_r, can be determined using Eq. 7 from Section 2.5 where E_{IT} and E_i are the indentation elastic modulus of the sample and the Young's modulus of the AFM tip, respectively, and ν and ν_i are their respective Poisson rations [92]. If the cantilever sensitivity, A, and cantilever-tip constant, α, are calculated before the experiment by using two reference materials, then K can be calculated from the slopes of force displacement curves and Eqs. 7 and 17 can be used to determine E_r, which allows for the determination of the indentation elastic modulus of the sample, E_{IT}.
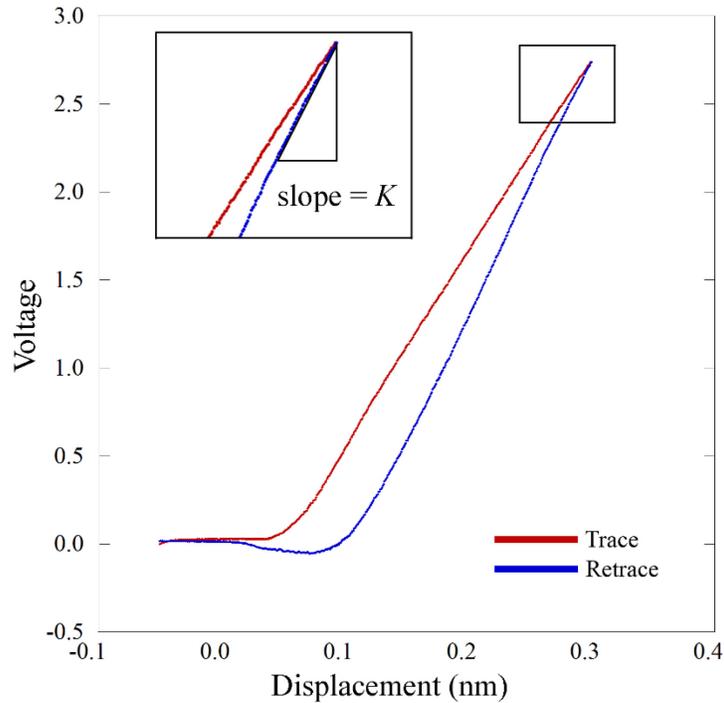
Figure 5.2.1: A graph of Voltage versus Displacement captured on the AFM, showing both the trace (red) and retrace (blue) force curves for PE. The value of K for Eq. 17 is calculated by taking the slope of the first 150 data points at the beginning of the retrace curve (inset), capturing the elastic response after indentation.
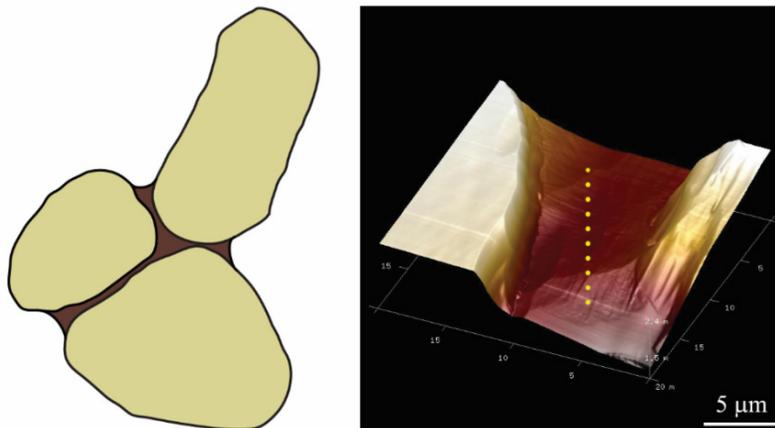
Figure 5.2.2: Left – an illustrated bonded joint showing the location of AFM indentation (Location 1 from Figure 5.2.3). Right – a 3D topographic image of the location captured during AFM. The yellow-dashed line represents an example of where indentations were performed.

Although the retrace (unloading) curve was used for this study, it has been shown that the trace (loading) curve may provide a better estimate of mechanical properties such as Young's modulus [117]. Additionally, it has been shown that varying the loading rate of nanoindentation can vary mechanical properties, with higher loading rates leading to increased hardness [118], [119]. However, since studies containing polymers used the unloading curve [92], [93], the retrace curves were used to determine indentation elastic modulus for this study. The control samples mentioned in Section 3.6 were indented via AFM with PMMA and indium being chosen as the reference materials for calculations. By using the K values captured from the force curves of PMMA and indium, A and α could be calculated from Eqs. 7 and 17 (Appendix A-2 and A-3). The resulting A and α values were 50.0 V/μm and 1.27 GPa, respectively. The average K values for all materials, along with their respective reduced elastic moduli, E_r, can be found below in Table 5.2.1. With A and α now known, the Goal Seek function of Microsoft Excel could be used to calculate the value of E_r from Eq. 17 for the other materials, providing a verification method of how well the test performed. Lastly, an estimate of the elastic modulus of the binder between sand particles of 3D-printed sandstone could be estimated the same way, resulting in a K value of 61.06 ± 1.84 μm/V and an indentation elastic modulus, E_{IT}, of 5.23 ± 0.31 GPa.

Table 5.2.1: K values of each sample with their respective reduced modulus, E_r, and Poisson's ratio, v, along with the calculated value for indentation modulus of elasticity, E_{IT}, from Eqs. 7 and 17. The samples highlighted had their elastic modulus set in order to calibrate the two unknown variables. Each material had a minimum of N = 30.

Sample	K (μm/V)	E_r (GPa)	v	E_{IT} (GPa)
PE	94.18 ± 3.44	1.44 ± 0.08	0.46[a]	1.14 ± 0.08
Epoxy	98.94 ± 1.52	1.30 ± 0.03	0.35[b]	1.15 ± 0.03
PP	78.04 ± 1.64	2.26 ± 0.08	0.42[a]	1.89 ± 0.08
HIPS	74.06 ± 3.38	2.63 ± 0.20	0.41[a]	2.23 ± 0.20
ABS	72.72 ± 1.84	2.79 ± 0.12	0.35[a]	2.49 ± 0.12
PMMA	68.79 ± 0.86	3.37	0.37[a]	3.0
PEEK	61.31 ± 1.26	5.59 ± 0.20	0.37[c]	4.89 ± 0.20
PFA	61.06 ± 1.84	5.72 ± 0.31	0.35	5.23 ± 0.31
PAI	59.85 ± 2.99	6.42 ± 0.52	0.45[c]	5.36 ± 0.52
Indium	55.95 ± 7.27	10.7	0.45[d]	9.2

Although the AFM is equipped with a microscope for real-time control of indentation sites, the light source is white light. Without a UV light source it can be difficult to determine which areas between particles contain binder. Luckily, the ion milling during sample preparation creates a visible boundary between mounting epoxy and 3D-printed binder (due to the difference in material properties), allowing for an estimate of where the binder is located. After indentation, the location of testing was found on a microscope and UV light was used to confirm the presence of 3D-printed binder. An example of an AFM indentation location is shown by Figure 5.2.3, showing the same area under white and a UV light source.
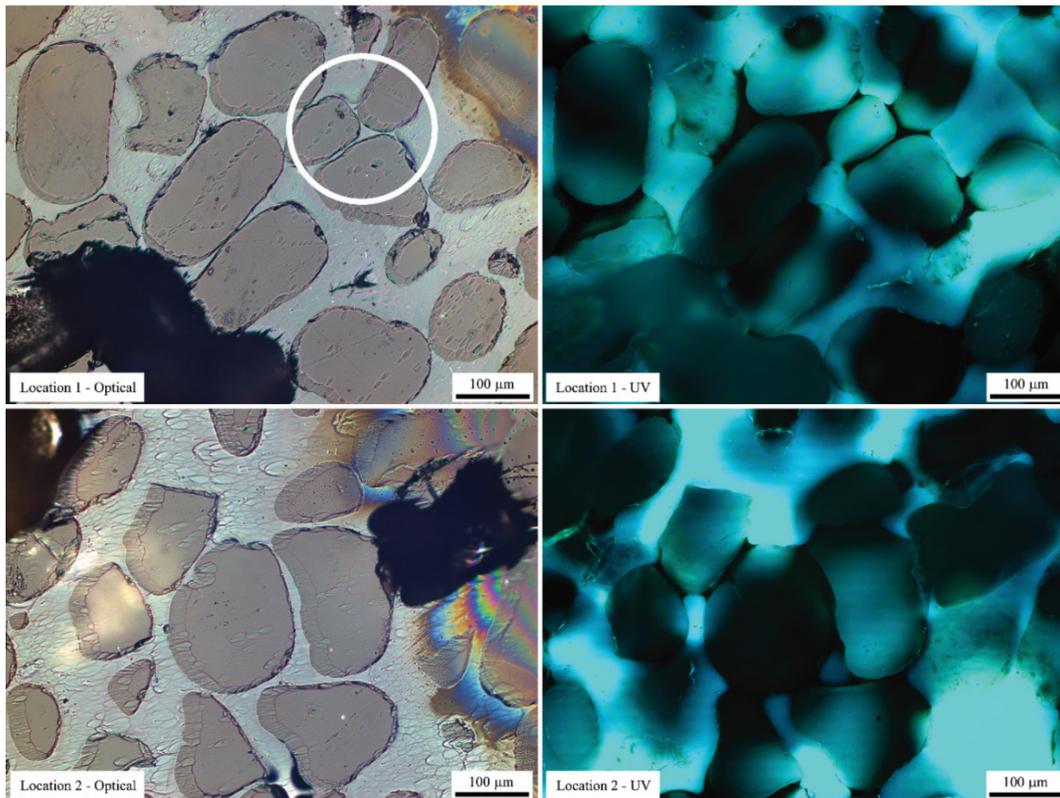
Figure 5.2.3: A collage of micrographs taken under white (optical) light and ultra-violet (UV) light of two locations of interest. The 3D-printed binder is not visible under the white light used in AFM, but the position of interest can be tracked and indented during AFM. The presence of binder can be confirmed before indentation by creating a topographic image of the surface (Figure 5.2.2), where indentation locations can be selected.

5.3 Determination of Indentation Elastic Modulus (E_{IT}) via Nanoindentation

In addition to AFM indentation, nanoindenation was performed for measurement verification by Anton-Paar (Montreal, QC). The indentation elastic modulus (E_{IT}) was calculated using the Oliver-Pharr method [91], where a projected contact depth and area are used to correlate the elastic modulus.

The main difference between the AFM technique of Section 5.2 and nanoindentation is that the AFM indentation method is based on an empirical relationship between reference materials, which captures variables such as tip rounding, contact area and depth into one constant, while nanoindenation is based on the Oliver-Pharr theory of contact mechanics [114]. Therefore, no other materials are needed besides the material in question as the indentation elastic modulus can be directly calculated. For comparison, the results of nanoindentation are tabulated below in Table 5.3.1, which show good agreement with the results of AFM indentation. However, the hardness of the PFA prepared on a glass slide is almost double that of 3D-printed sandstone. One could argue that the glass slide is interfering with the measurement, but the PFA layer was ~3 mm thick on deposition. The layer of PFA is much too thick for the glass slide to interfere with nanoindentation measurements, since the indentation is on the order of nanometres. A possible suggestion could be the method of synthesis or fabrication. The PFA on the glass slide was prepared via mixing and then curing in an oven immediately, allowing for a fast buildup of heat on the sample to reach 80°C. Yet 3D-printed sandstone is surrounded by sand in the job box when placed in the oven, meaning that it may take time to reach a temperature of 80°C. The slow ramp up in sample temperature may alter the kinetics of polymerization or to change the hardness of the PFA on the surface.

Table 5.3.1: Nanoindentation data performed and provided by Anton-Paar [123].

	Indentation Hardness (H_{IT}) (MPa)	Vickers Hardness (HV_{IT} - Vickers)	Indentation Elastic Modulus (E_{IT} - GPa)
PFA Slide	498.1 ± 28.2	46.1 ± 2.6	5.50 ± 0.26
Sample 1	263.5 ± 27.2	24.4 ± 2.5	5.30 ± 0.55
Sample 2	283.7 ± 2.9	26.3 ± 0.3	4.95 ± 0.67
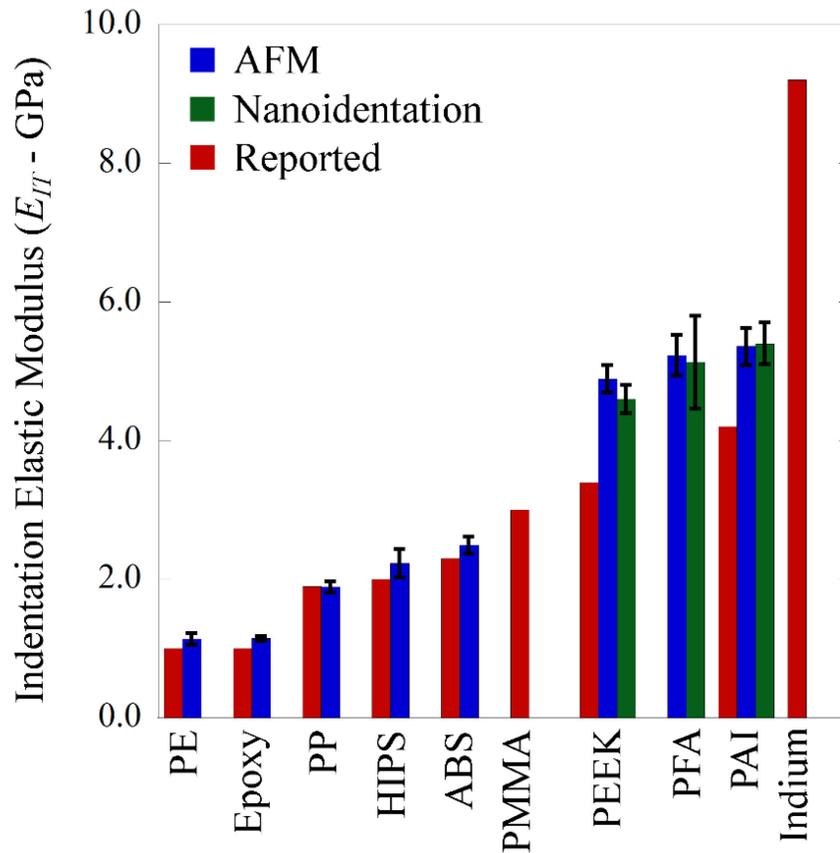
Figure 5.3.1: Indentation elastic modulus (E_{IT}) of various polymers, comparing the values obtained between Atomic Force Microscopy (AFM) and Nanoindentation. Theoretical values for the polymer samples are shown for reference [120]–[122]. A value of 5.23 ± 0.29 GPa was obtained for PFA via AFM and 5.13 ± 0.67 GPa via nanoindentation. A two-tail t-test with with $\alpha = 0.01$ shows that the elastic moduli values between AFM and nanoindentation are not significantly different ($t = 1.37 < t_{crit} = 2.66$, DOF = 62). PMMA and Indium were used as reference materials for Eq. 17. Sample size is a minimum of 30 per material.

Through determination of the Young's modulus of the solidified binder between silica grains, a micro-mechanical property for a 3D-printed geomaterial was determined for the first time. By direct quantification of the Young's modulus of the 3D-printed binder, it is hypothesized that PFC^{3D} calibration procedures for micro-mechanical properties of geomaterials may be bypassed in order to provide better estimations of macro-mechanical properties.

6   Improving Binder Adhesion

6.1   Motivation

The UCS of 3D-printed sandstone (~23 MPa) is less than half of natural sandstone (~60 MPa for Berea) [85]. Natural geomaterials are bound together with ceramic minerals such as feldspars, silica, and calcite, hence their properties are different that model materials bound with organic polymers. Therefore, there is a drive to increase the UCS of 3D-printed sandstone so that it may more closely resemble traditional rock coring samples through replication of the original, reducing cost and lowering the variance of lab scale testing. Additionally, replication of samples with controlled defects will allow for testing of different effects such as cracks and pores.

The hypotheses to be tested were: 1) due to the organic nature of the binder used during printing, there is poor adhesion to the inorganic silica particles, which may account for the lower strength compared to nature sandstone, and 2) silane coupling agents may reduce adhesive failure, as they have been used as an intermediary layer between surfaces to promote adhesion between organic/inorganic material systems for decades [124].

Since the binder used when 3D printing sandstone is an organic polymer, it has difficulty adhering to silica sand due to the lack of chemical bonds able to form with the surface, meaning the eventual adhesion relies on mechanical bonding. However, the silica sand grains are rounded and smooth, which can be detrimental to mechanical bonding. To increase adhesion, chemical bonds can be added via treatment of the silica sand surface with a silane coupling agent (SCA). The SCA creates an organo-functional group available to chemically bond with the polymer groups of the furfuryl alcohol thus increasing adhesion.

However, using functionalized silica sand in the 3D-printer is problematic, as the SCA causes the sand to easily clump together. Any media that is used in the 3D-printer must flow readily, otherwise clogging of the recoater is inevitable. Therefore, to test the feasibility of using silane-treated sand for 3D-printed sandstone, cylindrical specimens were fabricated via molding to provide insight into any UCS increases of poly-furfuryl alcohol and silica sand. If there was a significant improvement of UCS, then introduction of treated sand into binder jet based additive

manufacturing systems may be implemented by addressing the flowability of the functionalized silica sand.

6.2   Wetting Angle Measurements

In order to select SCA candidates for improving the adhesion of furfuryl alcohol to silica sand, glass slides were treated with each SCA and placed in contact with a 3 µL drop of furfuryl alcohol to test the wetting behavior. Figure 6.2.1 captures the behavior of furfuryl alcohol in contact with various SCAs. APTMS and GPTMS provided lowest contact indicating a possible adhesion improvement to silica. However, it should be mentioned that the wetting angle measurement is only used for the affinity of pure furfuryl alcohol and not polymerized furfuryl alcohol as no acid has been introduced during the wetting angle measurements.
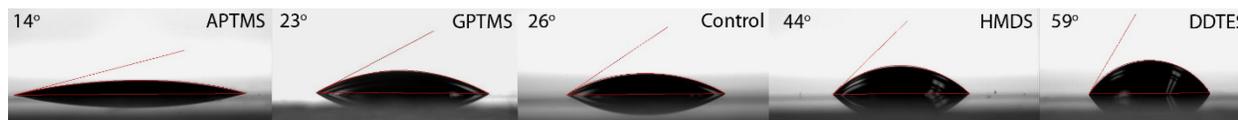
Figure 6.2.1: Contact angle measurements of furfuryl alcohol (3 µL) on glass slides treated with different SCAs. Different wetting behavior can be observed depending on the particular SCA used. A decreased contact angle (increased wetting; the two leftmost images of APTMS and GPTMS) is indicative of potential for increased adhesion through improved wetting.

Since APTMS and GPTMS both resulted in decreased contact angles for FA, it was possible that the surface adhesion of the polymerized FA would increase. It is suggested that adhesion of polymerized FA would increase based on the increased wettability of the FA, where surface tensions between liquid and surface would aid in adhesion [125]. Due to the complications of testing the tensile adhesion of glass, steel was used an alternative. Although the silica and steel have different surface chemistries, the surface is still inorganic compared to the organic furfuryl alcohol.

6.3   Adhesion Testing

In order to determine the maximum adhesive strength, the area of cross-linked polymer fracture surface area was measured via photography and image analysis, post tensile failure, where an example is given below in Figure 6.3.1. The results of adhesive testing are tabulated in Figure 6.3.2 below, with measured contact angles provided to show the inverse relationship with maximum adhesive strength.

149.1 mm^2 10 mm
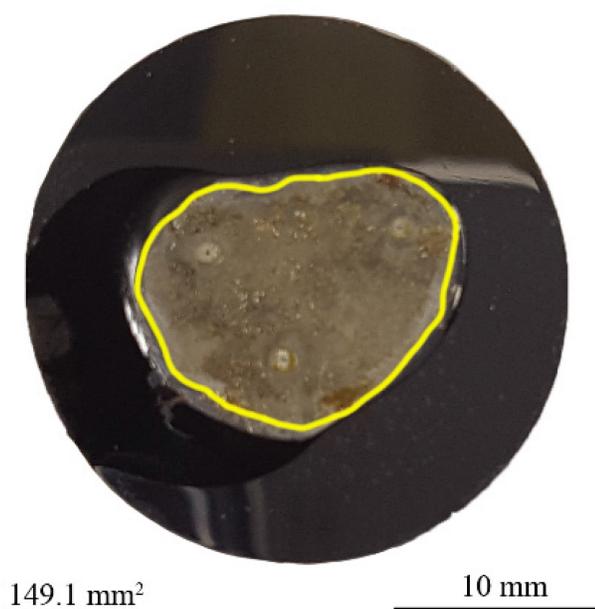
Figure 6.3.1: A photograph showing how image analysis was used to quantify the area of the
              irregular shape of the poly-furfuryl alcohol neck after testing. The yellow border
              indicates the perimeter of the calculated area.
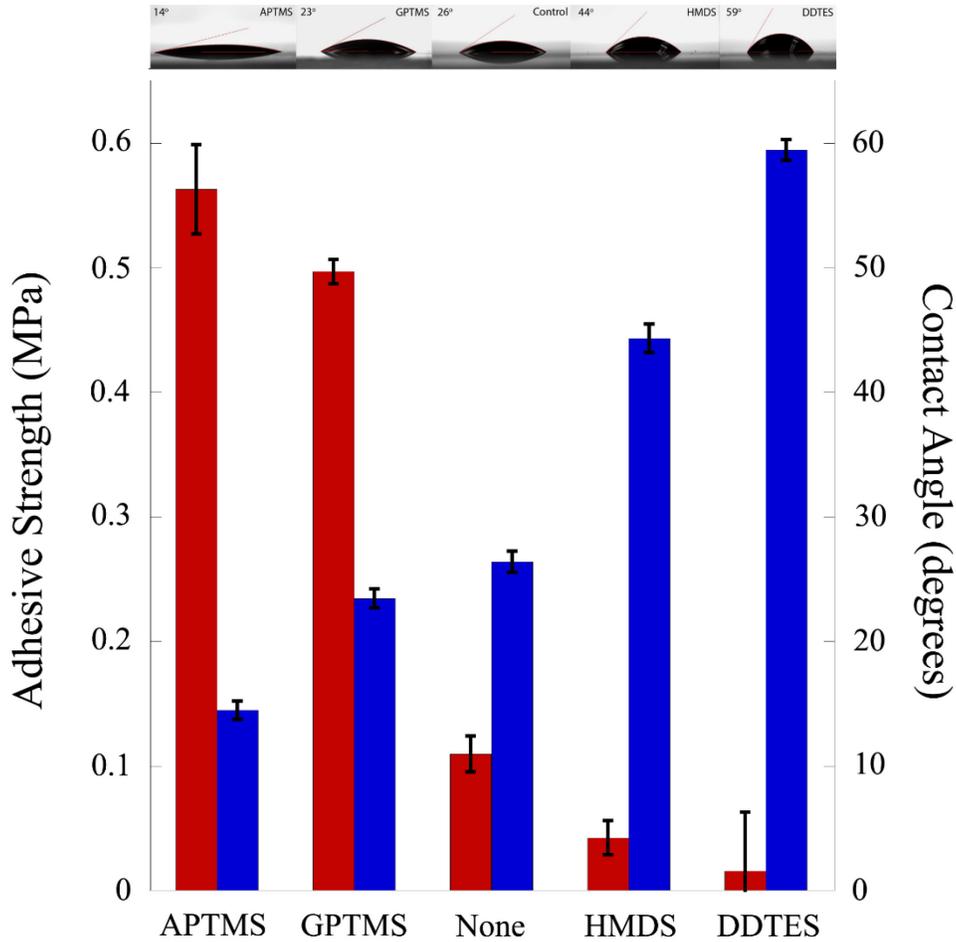
Figure 6.3.2: The adhesive strength of poly-furfuryl alcohol between polished AISI 1020 steel stubs showing how APTMS and GPTMS provide the greatest improvement compared to HMDS and DDTES. The improvement increase in adhesive strength may be attributed to the higher degree of wetting of furfuryl alcohol to the surface prior to curing (N = 3, error bars are standard deviation).

The relationship between contact angle and adhesive strength becomes clear when comparing Figure 6.2.1 and Figure 6.3.2, where the lower contact angle results in a higher adhesive strength, as expected. The SCA creates a hydrophobic layer, which will reduce the tendency for water to wet the surface, which can be detrimental to an organic adhesive. Due to their high adhesive strength increases, APTMS and GPTMS were chosen as SCA candidates for UCS testing of silica sand bonded with poly-furfuryl alcohol.

During fabrication of UCS samples, a critical observation was made. Upon addition of the acid activator to the furfuryl alcohol, a dark green color should develop over a matter of minutes, due to the presence of chromophores being formed, indicating that cross-linking is occurring [72]. The dark green color is evident with silica sand treated with GPTMS, but not APTMS (Figure 6.3.3). It was found that APTMS neutralizes the reaction between furfuryl alcohol and the cross-linking agent (p-toluene sulphonic acid). Upon closer inspection of the APTMS structure, the organic tail of the molecule is NH_2 (see Figure 6.3.4), which would create a basic surface. Therefore, although APTMS increases the wetting and adhesion of furfuryl alcohol, it is not compatible with polyfurfuryl alcohol due to the need for an acidic cross-linking agent, which is neutralized on contact with the functionalized surface. Even if the furfuryl alcohol is mixed with the acid before addition to the sand, the reaction was still neutralized and no further cross-linking occurred. However, it is interesting to note that the cross-linking reaction was not neutralized by APTMS when a polished, steel surface was used (adhesive testing). Although the reason is unexplained at this time, we suggest that the large increase of surface area when using silica sand instead of a polished, steel sample may attribute to the neutralization of the acid activator.
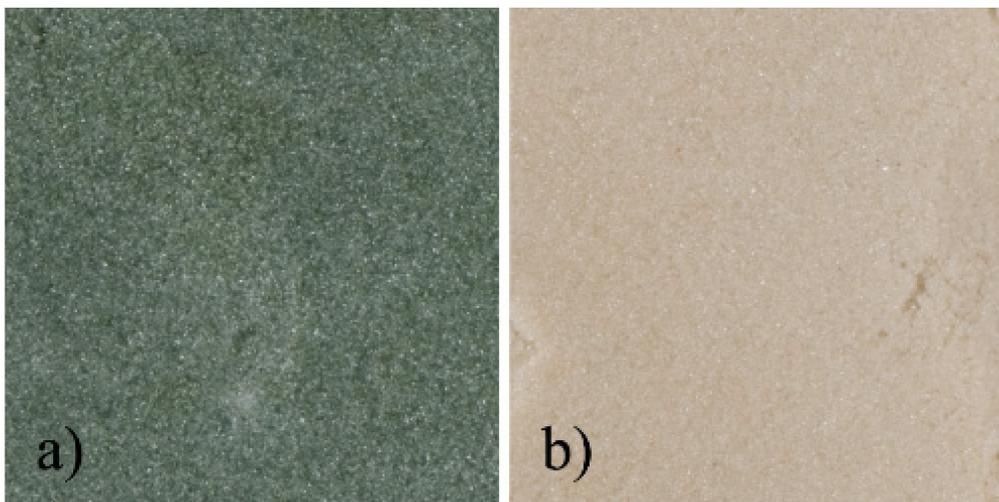
Figure 6.3.3: Furfuryl alcohol and p-toluene sulphonic acid added to a) untreated sand and b) sand treated with GPTMS. The green color in a) is indicative that cross-linking of the furfuryl alcohol has occurred. The absence of any color change for the sand in b) means no cross-linking has occurred, a consequence of APTMS creating a basic surface on the silica sand and neutralizing the p-toluene sulphonic acid used for cross-linking.
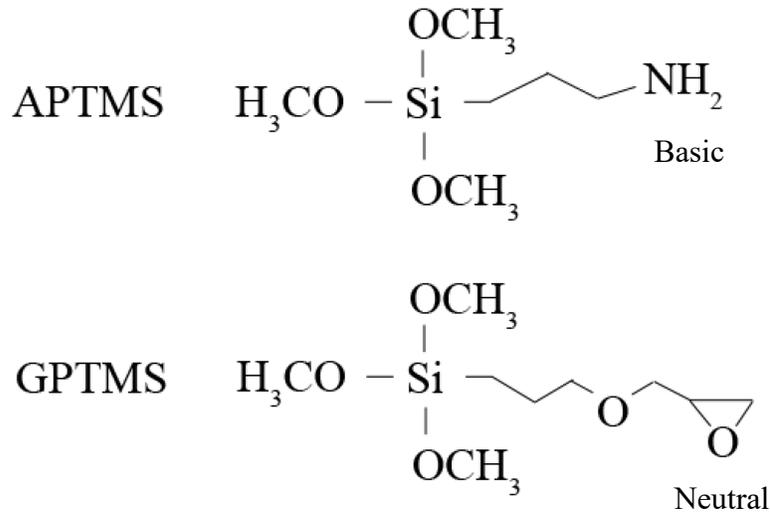
Figure 6.3.4: A schematic of the APTMS and GPTMS molecular structure contrasting the differences in the functional chain end. APTMS has a NH_2 chain end, which can leave the surface of the silica sand in a basic state, neutralizing the acid activator responsible for cross-linking the FA.

6.4   Improvement of Unconfined Compressive Strength (UCS)

Cylindrical compression samples were fabricated for both bare and functionalized silica sand as described earlier. An example of a failed UCS sample was shown previously in Figure 4.6.1 where axial splitting occurred, which is a typical failure mode of natural rock [126]. The results are plotted below in Figure 6.4.1, where the SCA-treated samples can be observed to have a significant increase in UCS. A two tail t-test was performed on the UCS results and they were found to be significantly different, since the t-value of the two sample sets is higher than the critical t-value ($t = 8.06$, $\alpha = 0.001$, $t_{crit} = 3.51$). SEM images of a control and functionalized sample can be found below in Figure 6.4.2, where the difference in fracture behavior between the sand grains can be observed. For the control samples (no SCA), binder necks mostly failed in adhesive failure, where a poly-furfuryl alcohol ring provides evidence of where a neck was bonded previously and other necks show a smooth cup, suggesting pull off with the binder intact. As for the functionalized samples with a SCA, binder necks suffered cohesive failure, where the binder failed in shear, which is traditional for natural rock UCS samples [126]. Additionally, cohesive failure likely requires more energy than adhesive failure, which is evident from the increased adhesion strength of SCA-treated steel in Figure 6.3.2.
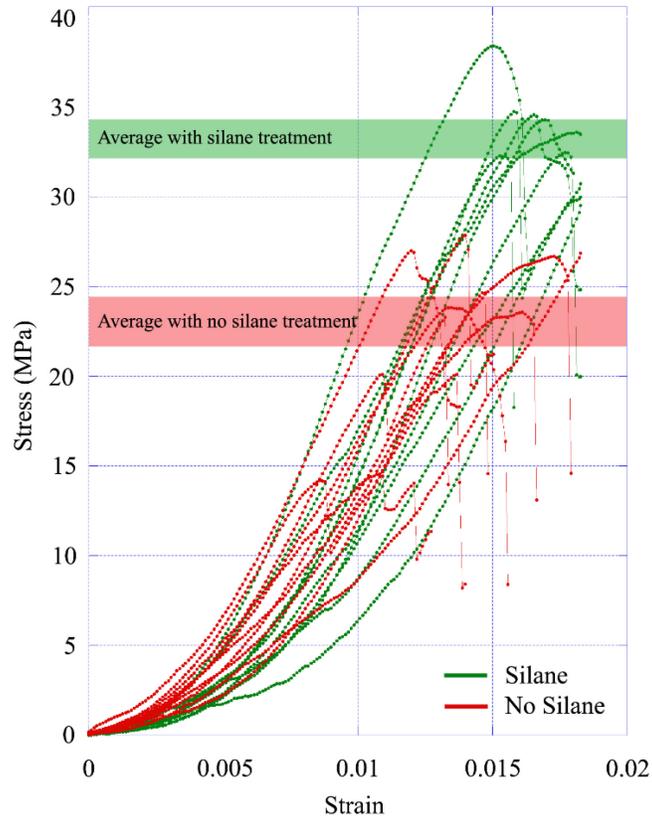
Figure 6.4.1: UCS curves for molded poly-furfuryl alcohol and silica sand, with and without silane treatments of GPTMS. The increased UCS of silane-treated sand can be attributed to the increased wetting and adhesive strength on the silica sand surfaces.
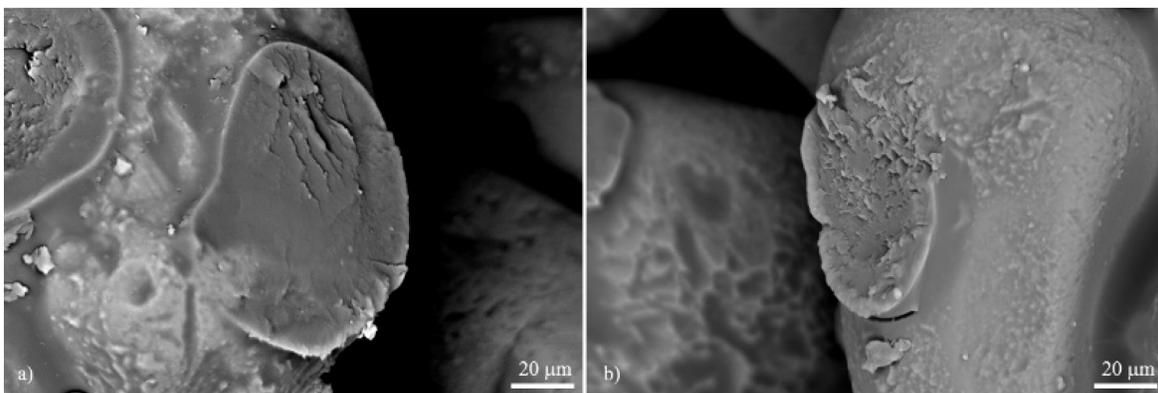
Figure 6.4.2: One half of a binder neck from a UCS sample fabricated using a) untreated sand and b) sand treated with GPTMS. The failure surface of the binder neck in a) is smooth, which may suggest a decoupling from the surface or adhesive failure. The rough surface of the failed neck in b) suggests increased adhesion during failure.

6.5   Effect of Silanization on E_{IT}

In order to explain the apparent increase in UCS of 3D-printed sample exposed to silanization, samples were indented via nanoindentation to capture any changes in E_{IT}. The results of nanoindentation on samples before and after silanization are shown below in Table 6.5.1, where it can be seen that the silanization of the sand has increased the indentation elastic modulus of the binder. With an increase in E_{IT} it can be argued that the UCS of the 3D-printed samples has increased due to stiffer bonds between grains. When combined with Figure 6.4.2, where the binder neck appears to have a more ductile failure and the data collected in Table 6.5.1, it is reasonable to believe that the stiffness of the bonds, combined with better adhesive strength is the reason for an increase in UCS. To provide further evidence, the Young's modulus of sample with and without a SCA were calculated and compared. It was found that samples without any SCA had an E of 1.14 ± 0.1 GPa and samples treated with a SCA had a E of 1.36 ± 0.04 GPa (Figure 6.5.1).

Table 6.5.1: Nanoindentation results performed by Anton Paar [106] combined with the UCS measurements from Figure Figure 6.4.1.

	Indentation Hardness (H_{IT}) (MPa)	Vickers Hardness (HV_{IT}) (Vickers)	Elastic Modulus (E_{IT}) (MPa)	UCS (MPa)
Silane	394 ± 36	36.5 ± 3.3	7.92 ± 1.46	33.9 ± 1.8
No Silane	189 ± 16	17.5 ± 1.5	5.53 ± 0.93	23.8 ± 3.9
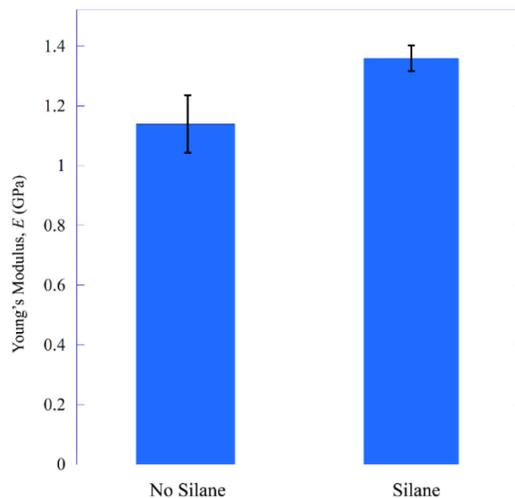
Figure 6.5.1: Graph containing the average values of Young's modulus, E, for UCS samples containing no silane and those with GPTMS treatment.

7 PFC³ᴰ Simulation

7.1 Motivation

Well before 3D-printing was invented, computer modelling was established as a possible method of reproducing samples by digitally reconstructing geomaterials based on calibration data acquired via UCS testing. Variance in properties such as grain size and bedding orientation could be controlled and ran without the need of additional samples once calibrated. Particle Flow Code (PFC³ᴰ - Itasca Consulting Group, MN, USA) is one software of choice for many geological engineers, where a matrix of packed spheres represents granular material. Chapter 5 presented results for the binder indentation elastic modulus (E_{IT}), which can be argued to be synonymous with one of the major parameters required for any PFC³ᴰ simulation: the cement elastic modulus, $\bar{E}_c$. The cement elastic modulus is usually calibrated before simulation, by fitting parameters to USC tests on laboratory samples. However, by measuring the Young's modulus of the 3D-printed binder in-situ, calibration of $\bar{E}_c$ can be replaced with a quantified value for the first time. However, before results of the simulations can be presented the following sections present a background on the theory and assumptions that govern PFC³ᴰ.

7.2 The Bonded Particle Method (BPM)

One model that is routinely used in FEA for particulate rock material such as sandstone, is the bonded particle model (BPM) proposed by Potyondy et al. [127]. The BPM for rock is a mathematical model to predict the behavior of heterogeneous material comprised of cemented grains and is used in one of the more popular codes for predicting mechanical behaviour of rock, Particle Flow Code (PFC³ᴰ). The BPM model can be used with cemented sedimentary rock, such as sandstone, where sand particles are cemented together at various contact points. Under load, compressive, tensile, shear and rotational forces are developed that lead to microcracking within the material. Potyondy et al. [127] explains that the mechanical behavior of rock is driven by the evolution of "force-chains", the summation of micromechanisms (individual changes in response to stress) surrounding a grain leading to increased loads. Due to these force-chains, some particles experience higher loads, while others experience none. It is the summation of these forces and responses that determine the macroscopic properties of the material, as determined by the BPM.

When a bond between particles or "spheres" in the model is broken, the force values on surrounding particles is adjusted, which may cause additional bonds to fail leading in the growth of a crack. Although micromechanical properties in rock are unknown, the BPM can be used following a macroscopic test to calibrate the elastic properties of the material [127].

As mentioned earlier, one software platform that is routinely used to model mechanical behaviour of rock masses is Particle Flow Code (PFC^{3D}). In order to use PFC^{3D}, values such as the radii of particles, friction coefficient at the particle contacts and bond strength values of joints between particles must be entered. Contact normal and shear stiffness values must be estimated, as well. The previous values may be determined using a laboratory scale calibration and inverse modelling procedure by acquiring macromechanical properties through compression and shear testing [17], [128], [129]. However, since the material properties are acquired through macromechanical testing, they only reflect continuum behavior and not discrete contacts or joints between particles, bringing forward the problem discussed earlier in Section 1.1 of a scaling effect. Furthermore, macromechanical testing does not differentiate from discontinuities in bulk geomechanical material. As stated in the PFC^{3D} Manual from Itasca [49] "scale-dependence of joint properties is a major question in rock mechanics", which has yet to be addressed fully. Since no theory exists relating macromechanical and micromechanical material properties of bonded rock, micromechanical material property selection for PFC^{3D} is usually adopted based on the reflection of an accurate macromechanical response [49], [128].

Due to the heterogeneity of rock, the macromechanical and micromechanical calibration method has been widely accepted [128], [129]. However, with each iteration of altering micromechanical values in FEA, it becomes unclear as to which material properties are accurate when multiple parameters are changed to fit the macro-mechanical response. Additionally, the use of spheres in PFC^{3D} cannot accurately capture the behavior of complex shapes or interlocked grains, which has resulted in unrealistic ratios of unconfined compressive strength to indirect tensile strength for digitally-constructed rock specimens [129]–[131]. It is suggested that appropriate parameters for PFC^{3D} modelling be chosen by comparison to joint properties acquired from field data, but field testing for joint properties is "extremely limited" [49]. A study by Kulhawy et al. [132] contains some field test observations, with limited summaries of normal and shear stiffness available elsewhere [26], [133].

However, it can be difficult for PFC^{3D} users to select the correct data based on the natural heterogeneity of rock. One of the main reasons is discussed by Kulhawy [132], stating that the stress-strain behavior of rock materials is non-linear over a wide range of stresses. Even for a carefully controlled experiment, where the test specimens and conditions simulating a field condition are duplicated, the stress-strain behaviour is dependent on the magnitude of confining pressure [132]. Therefore, the reliability of results obtained from uniaxial experiments that are used to obtain data for macro and micromechanical calibration methods can become suspect.

Additionally, the following is explicitly stated by the software company Itasca [49]:

> "Although the behavior of the PFC model is found to resemble that of rock, in general, we do not associate a PFC particle [sphere] with a rock grain. The assembly of bonded particles is a valid microstructural model in its own right and should not be confused with the microstructure of rock. If it is required that the microstructure of rock be modeled in detail, then the smooth-joint contact model can be used to create a grain-based model" [49, p. 3-7]

The "smooth-joint contact model" quoted above is one proposed by Mas Ivars et al. [22] in 2011, where the BPM is used to represent intact material and a smooth-joint contact model (SJM) is used to represent the in-situ joint network. His proposed model was an attempt to address the problem of the rock mass classification (RFC) systems developed for and in use in civil and mining engineering, where rock masses can be "ranked" based on their joints and weakening/softening effects [22]. Additionally, Mas Ivars et al. [22] continues to state that the "the ability for Rock Mass Classification (RMC) systems are not particularly well-suited for estimating strength anisotropy and scaling effects."

Regardless of the model used, a numerical value for the elastic moduli of the digital "cement" bonding spheres together in PFC^{3D} must be calibrated or estimated. However, to the best of the author's knowledge, has never been quantified directly. Due to the natural heterogeneity of rock, there exists a deficiency in the translation from macromechanical response of rock masses to micromechanical property input parameters for PFC^{3D}.

7.3   Particle Flow Code (PFC^{3D}) – Contact Theory and Assumptions

Due to the recurring references to PFC^{3D} in the previous section, the author felt it important to provide a summation of the contact assumptions and mathematics used be provided. A thorough explanation of the contact assumptions and mathematics used within PFC^{3D} can be found in the software manual [49], but for clarity a few key points will be summarized below.

PFC^{3D} is governed by the use of thousands of "spheres" that interact with one another in a simulated vessel of finite dimensions. Although a common assumption is to believe a single sphere is the same as a single rock grain, the software company itself warns against this logic since the sphere is simply a pointer for a mathematical equation and has no physical meaning [49]. Spheres have been "clumped" together in an attempt to obtain a more realistic simulation, but stiffness, radii and friction parameters are still required to be entered and calibrated [131]. Additionally, the accuracy and resolution of a simulation can be increased by adding more spheres, but the computation time can easily turn from minutes to hours.

PFC^{3D} is built and constrained by two different types of bonds between particles: contact and parallel. Contact bonds occur at a "vanishingly small point" and are governed by Hertzian contact mechanics, while parallel bonds have a finite amount of material between them that allow for shear and moments to develop [49]. Figure 2.8.1 contains an illustration of a contact and parallel bond for clarity, where it can be seen that there is no shear component for a contact bond. For 3D-printed sandstone, no contact bonds exist and the necks of binder adhering two silica grains together (Figure 4.3.2) share similarities with parallel bonds.
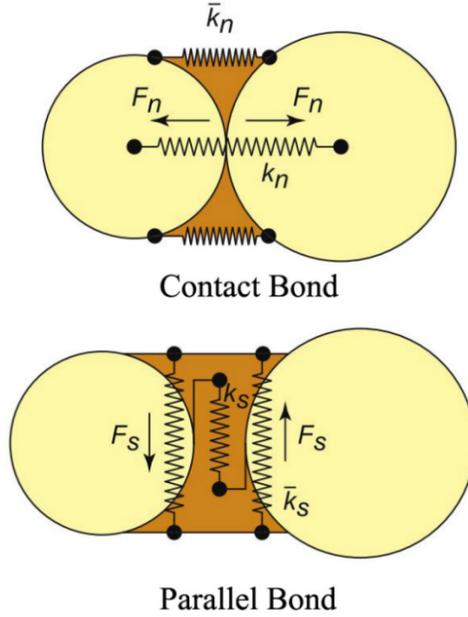
Figure 7.3.1: Illustration of a contact bond and parallel bond that govern PFC^{3D}. Reprinted from Lisjak et al. [130] under a Creative Commons License.

An important comment that must be made is that when a parallel bond breaks the stresses dependant on the bond are set to zero and the bond is deleted, along with the material between spheres. However, in reality when a bonded joint breaks there may be material left over that can attribute to frictional forces acting on the grain that are not accounted for in PFC^{3D}. Additionally, there is a parameter named the "radius multiplier" of a parallel bond that is defined as the ratio of parallel bond width to particle diameter. Therefore, the default value of 1.0 means that the parallel bond is the same width as the particle diameter, which is not the case for 3D-printed binder necks and will be addressed in Section 7.5.

For PFC^{3D} simulations containing parallel bonds the cement Young's elastic modulus, $\bar{E}_c$, is a parameter that is required and, to the best of the author's knowledge, has never been quantified prior to calibration. $\bar{E}_c$ can be defined as the Young's modulus of the material "gluing" the spheres together during PFC^{3D} simulations. $\bar{E}_c$ is usually adjusted to tune the Young's modulus, E, of the simulated rock material to the E of a rock material that was previously tested in compression in a laboratory setting. Additional information concerning PFC^{3D} theory and the calibration procedure can be found in Appendix A-4.

7.4 Comparison of $\bar{E}_c$ Values to Literature

It is difficult to compare values of $\bar{E}_c$ directly since the cement in 3D-printed sandstone is polymeric and not crystalline or ceramic in nature as is the case for all studies with reported $\bar{E}_c$ values. Therefore, this section is merely to be used as a relative comparison on the works of previous researchers and the assumptions they used in modelling rock using the BPM and PFC^{3D}.

In 2013, Rong et al. [134] published a study that was aimed at understanding the relationship particle shape has on mechanical properties of a rock mass using PFC^{3D}. Using the traditional method of triaxial testing to determine microproperties, followed by a numerical calibration procedure, they selected an $\bar{E}_c$ of the parallel bonds in their model sandstone to be 20 GPa.

In 2014, Ding et al. [135] were interested in model scale and particle size distribution on simulated macroscopic properties of rock and used an $\bar{E}_c$ value of 69.7 GPa, comparing most of their assumptions to Potyondy and Cundall [127], which used a value of 72 GPa. Since granite was used in both studies, the cement elastic modulus was set as the same as the grain elastic modulus.

For red sandstone, a study was published in 2014 using a calibrated value of 8.6 GPa for $\bar{E}_c$ [136], which is the closest match for the 3D-printed sandstone analogue. However, the cementing material for 3D-printed sandstone is polymeric and not geological "sediment".

7.5 PFC^{3D} Results

PFC^{3D} simulations were run using the aid of the Virtual Lab Assistant (VLA) written by Nathan Deisman for Itasca, where input parameters for several properties are calculated before-hand using the pre-defined FISH language within the software and pre-loaded prior to any computations. The VLA allows for complicated simulations to be run by setting the parameters at the beginning of the simulation.

The PFC^{3D} simulation begins by creating a virtual cylindrical "vessel" with retaining walls. The bottom of the cylinder has a stationary wall that does not move during simulation. Once the vessel has been created, the balls are added one at a time until the vessel is filled, with any balls being deleted that do not have three or more contacts. Afterwards, the balls expand slightly to

reduce the porosity in the vessel further. At this point, a compressive stress of 1 MPa is usually added to the vessel to compact the specimens. During 3D-printing of sandstone, there is only a minor amount of tamping from the Re-coater on the M-Flex printer. Therefore, instead of the default of 1 MPa, a packing density of 100 kpa was used to pack the vessel. Afterwards, parallel bonds are created for particles that are in contact, followed by removing the cylindrical retaining wall. The sample is now representative of a particulate UCS sample as shown below in Figure 7.5.1. To meet ASTM D7102 standards , the top of the specimen is shown in Figure 7.5.1 where it can be seen that the diameter of the specimen is at least six times the largest grain diameter [85]. Once the sample has been created, a retaining wall moves vertically along the axis of the sample to mimic a UCS test. The test continues until the stress reading is 0.8 times the maximum recorded stress. At this point the test is terminated and the Young's modulus of the sample, E, can be determined. E is determined through measuring the slope of the stress-strain curve generated during the simulation, where strain is recorded by movement of the top and bottom retaining walls.
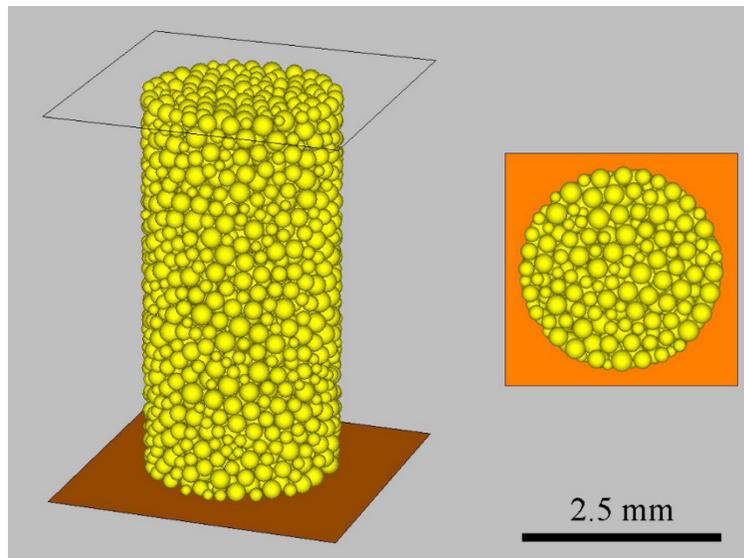
Figure 7.5.1: Screenshot showing a 2.5 mm (resolution = 12) UCS sample simulated by PFC^{3D}. A top view is provided on the right to meet ASTM D7102 requirements. The orange platen is stationary and immovable, while the transparent wall at the top of the sample moves downward along the sample, axially, compressing until the recorded stress is 0.8 times the maximum stress.

A number of parameters were kept constant between simulations with PFC[3D] and are captured in Table 6.5.1. Particle resolution is defined as the number of particles across the diameter of the sample and can be calculated by:

$$RES = \left(\frac{L}{R_{min}}\right)\frac{1}{\left(1 + \frac{R_{max}}{R_{min}}\right)} \tag{18}$$

where L [mm] is the diameter of the specimen and R_{min} and R_{max} [μm] are the minimum and maximum radii of the particles, respectively [137]. For PFC[3D] simulations particle radii were chosen based on a report from ExOne where 53% of the sand grains were between 100 and 140 Mesh and 44% of the grains were between 140 and 200 Mesh. Therefore, a R_{max} of 149 μm and a R_{min} of 74 μm were used (based on the mesh sizes stated previously). By using a diameter of 2.7 mm and incorporating the 2:1 height to diameter ratio deemed by ASTM 7102 [85], a resolution of 12 was targeted. The value changes slightly once the simulation begins since the particle enlarge slightly to fill any remaining porosity before bonds are created.

Table 7.5.1: PFC[3D] simulation parameters

Particle Resolution	~12
Minimum Particle Radius (μm)	74
Maximum Particle Radius (μm)	149
Radius Ratio (R_{max} / R_{min})	2.014
Minimum Number of Contacts[a]	3
Ball Density (kg/m^{3})[b]	2648
Stiffness ratio (k_n/k_s)[c]	4.84

[a]Minimum number of contacts is the number of contacts a particle must have on loading or else it is deleted. The default value was chosen from PFC[3D].
[b]Ball density was set to mimic silica sand grains [99].
[c]Stiffness ratio was chosen through consultation with PFC users.

There is an immediate disconnect between sample dimensions from UCS samples (12.5 mm) in Chapter 4 to the sample diameter of 2.7 mm reported here. The reasoning is to keep particle resolution ~12, which resulted in a more manageable simulation time (~ 2 hours). Theoretically, PFC[3D] output is varied by particle resolution and sample diameter should not change the values of [49]. Therefore, if a 12.5 mm diameter specimen was to be simulated, the radii of particles should

be increased appropriately. For the following simulations the radii of particles were kept the same as the silica sand used in 3D-printed sandstone.

In order to compare the values of $\bar{E}_c$ acquired through AFM and nanoindentation to simulated values, the parameters in Table 7.5.1 were modelled in PFC^{3D} via the VLA platform. Table 7.5.2 contains outputs of PFC^{3D} from the simulations, where it can be seen that the Young's modulus of the samples is in the range of Young's modulus reported by Primkulov et al. [15], but the UCS is underestimated. For Runs 1-3, $\bar{E}_c$ was set to the value measured through AFM and for Run 4 it was set to the value of silanized samples from Section 6.5.

Table 7.5.2: PFC^{3D} simulation outputs using the parameters from Table 7.5.1.

Run	Particles	Resolution	$\bar{E}_c$ (GPa)	Radius Multiplier	UCS (MPa)	E (GPa)
1	1972	11.7	5.23	0.50	5.57	1.73
2	2883	12.1	5.23	0.55	6.57	1.88
3	2247	12.2	5.23	0.60	9.74	2.19
4	2247	12.2	7.92	0.60	10.38	3.09

One of the major assumptions of PFC^{3D} is that the particles are round, which is not the case for 3D-printed sandstone (Figure 4.2.2). The silica contains angularity that is not captured in the simulation, which may increase the friction between particles on compression, resulting in a higher UCS in a laboratory setting. The sample size of the simulation is also arguable, but could be tested in the future by increasing the sample dimension and resolution.

It is suggested that the underestimation of UCS (< 20 MPa) may also be due to the radius multiplier parameter. By default it is set to 1.0, making the parallel bonds as wide as the particle they are bonding, but that is not the case for 3D-printed sandstone (Figure 4.3.2). The 3D-printed binder necks can vary from a fraction of the particle diameter to a bond encompassing most of the particle diameter. For the simulations, the radius multiplier was set to a value of 0.5 – 0.6 to better capture the microstructure of 3D-printed binder necks. When the radius multiplier was raised from 0.5 to 0.6, the UCS was almost doubled, suggesting a strong sensitivity to this parameter.

7.6   Summary of Mechanical Properties

Figure 7.6.1 contains two graphs that provide a summation of mechanical testing completed on 3D-printed sandstone and the resulting simulation values from PFC^{3D}. The UCS of

3D-printed sandstone containing 8 vol. % of binder was the same (~23 MPa) for both a small desktop tester and a full-sized Instron tester. However, the Young's modulus values differed and can be explained due to a higher machine stiffness and compliance for the Instron tester. The PFC^{3D} values matched the Young's modulus values obtained on the Instron tester, but fell far below the average UCS values for both the Instron and desktop tester. A review of Table 7.5.2 shows that UCS of 3D-printed rock may have a strong sensitivity to the radius multiplier parameter of PFC^{3D}.
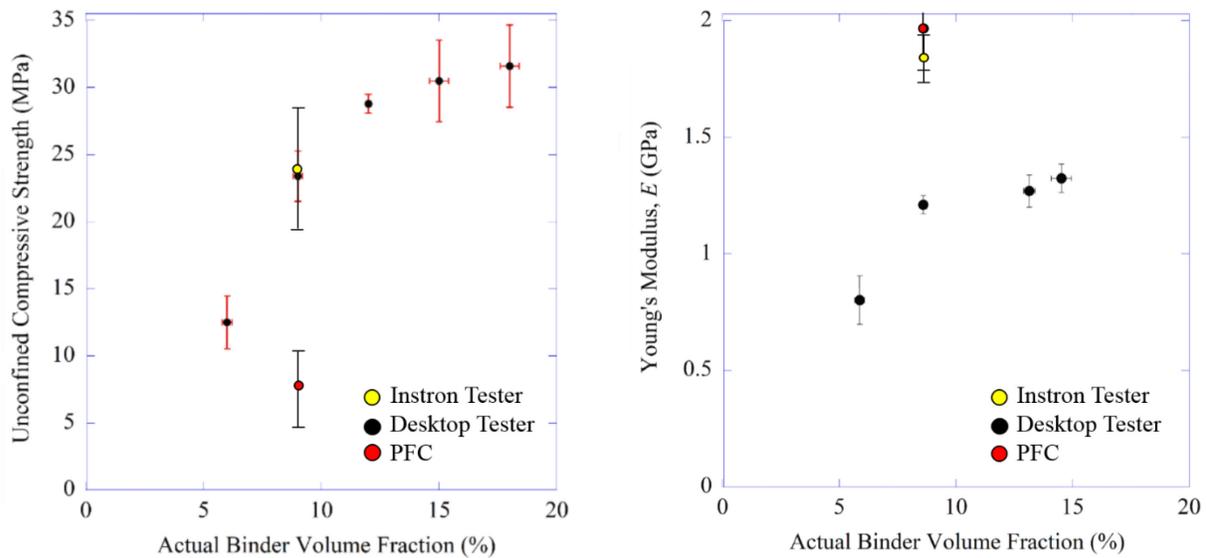
Figure 7.6.1: Left: Unconfined compressive strength of 3D-printed sandstone as a function of actual binder volume fraction. Right: Young's modulus of 3D-printed sandstone as a function of actual binder volume fraction. The PFC^{3D} simulation results do not match the UCS measurements, but do match the Young's modulus results from the Instron tester. However, the PFC^{3D} simulation results match closely to the Young's modulus of 3D-printed sandstone measured on an Instron machine.

8   Conclusions and Future Work

Variability in geomaterial properties such as grain size, number of grain contacts and cementing type, to name a few, may make the results of geomechanical laboratory tests suspect. Additionally, with such a high variance in material properties of geomaterials the opportunities for complete repeatability of a test is extremely low. Thus 3D-printing of sandstone creates prospects of tighter sample variance and controlled properties, making the idea of repeatable geomechanical engineering tests a possibility.

Using a research paradigm encompassing the materials engineering approach of studying processing, structure, properties and performance of a material, 3D-printed sandstone was characterized using various techniques that were presented within this thesis. By studying the processing and properties separately, the UCS and Young's modulus of 3D-printed sandstone were increased by raising the binder volume fraction without a loss of dimensional stability. However, as acknowledged previously in Section 5.4, the UCS test data presented within this thesis for 3D-printed sandstone were completed on a desktop tensile tester, with a maximum load of 7kN. Therefore, not only would the frame compliance and stiffness be a source of error, reducing the Young's modulus recorded, but the size of the system required smaller samples of only 25 mm tall. The scaling effect with regards to UCS and sample size was raised earlier, where the UCS and Young's modulus can appear to be larger with smaller samples. This is due to the fact of "dead zones" interacting with each other during UCS testing. Therefore, the relationships between binder volume fraction and UCS or Young's modulus could be improved by either incorporating the data from other researchers on the same material or repeating the UCS testing with larger samples on a larger testing system.

An optimum binder volume fraction was determined in this thesis, but other parameters for the M-Flex machine were not explored such as, but not limited to, recoater speed and layer thickness. Additionally, the theory and physics behind print head technology is vast and was not touched upon for this thesis. By understanding the relationships between piezoelectric nozzles and binder fluid properties, 3D-printed sandstone models may be improved.

Although 3D-printed sandstone properties such as UCS, Young's modulus and saturation limits were studied, the literature on the polymerization and polymer properties of poly-furfuryl

alcohol is limited. Future work would benefit from a rheology study during polymerization and a measurement of the cross-link density after post-curing. Additionally, a statistical analysis of binder neck size, along with grain size distribution, would aid in understanding and modelling the binder volume fraction in relation to mechanical properties.

A silane coupling agent (SCA) was added to cast samples prepared using the same materials used to 3D-print sandstone. A two-fold increase in UCS was observed compared to samples that contained no SCA. It is suggested that the SCA acts as an adhesion promoter between the binder and the silica grains, allowing for higher stresses to be exhibited on the sample before failure. However, as mentioned, the samples used for UCS testing were cast and not 3D-printed. The reasoning is that the SCA causes the silica sand to clump easily and upon printing will become clogged, resulting in a failed print. To increase the flowability of the treated silica sand, it is suggested that a commercially available flow additive such as fumed silica be admixed prior to 3D-printing in an attempt to address the clogging of the 3D-printer recoater.

The indentation Young's modulus (E_{IT}) of 3D-printed sandstone binder between sand grains was quantified via direct measurement of a printed sample, resulting in a value of 5.23 ± 0.3 GPa. The results compare favourably to nanoindentation tests performed by Anton Paar of 5.13 ± 0.9 GPa. Interestingly, when nanoindentation was performed on samples that had been treated with SCA, the E_{IT} of the binder increased to 7.92 ± 1.5 GPa. The reasoning for the increase in E_{IT} is unknown at this time, but it is suggested that a reaction with the SCA may cause the cross-link density of the binder to increase.

Lastly, PFC^{3D} simulations were presented using the E_{IT} values obtained via AFM nanoindentation and inputted as $\bar{E}_c$, the Young's modulus of material bonding particles together. It was found that although Young's modulus can be matched, the values of UCS are underestimated. It is suggested that the assumption of spherical particles and parallel bond sizing may attribute to underestimated values. To better fit simulations of PFC^{3D} with $\bar{E}_c$ values quantified using AFM and nanoindentation, a sensitivity study should be completed on the radius multiplier parameter. A future study could include 3D-printing sandstone with spherical powder to match the assumption made by PFC^{3D}, followed by statistically determining the size of the 3D-printed binder necks via microscopy or micro computed tomography (CT) scanning.

Bibliography

[1]   E. Broch and J. A. Franklin, "The point-load strength test," *Int. J. Rock Mech. Min. Sci.*, vol. 9, no. 6, pp. 669–676, 1972.

[2]   H. J. Pincus, "Interlaboratory Testing Program for Rock Properties, Round One - Longitudinal and Transverse Pulse Velocities, Unconfined Compressive Strength, Uniaxial Modulus, and Splitting Tensile Strength," *Geotech. Test. J.*, vol. 16, pp. 138–163, 1993.

[3]   H. J. Pincus, "Addendum to Interlaboratory Testing Program for Rock Properties, Round One," *Geotech. Test. J.*, vol. 17, pp. 256–258, 1994.

[4]   Weatherford Laboratories AS, Image [Online]. Available: https://portal.weatherfordlabs.com/default.aspx?ReturnUrl=%2f, accessed October 27, 2017.

[5]   W. F. Brace, "Dependence of fracture strength of rocks on grain size," in *The 4th U.S. Symposium on Rock Mechanics (USRMS)*, 1961, p. March 30-April 1.

[6]   M. P. Fahy and M. J. Guccione, "Estimating strength of sandstone using petrographic thin-section data," *Environ. Eng. Geosci.*, vol. 16, pp. 467–485, 1979.

[7]   W. A. Olsson, "Grain size dependence of yield stress in marble," *J. Geophys. Res.*, vol. 79, pp. 4859–4862, 1974.

[8]   C. G. Dyke and L. Dobereiner, "Evaluating the strength and deformability of sandstones," *Q. J. Eng. Geol. Hydrogeol.*, vol. 24, pp. 123–134, 1991.

[9]   R. Ulusay, K. Türeli, and M. H. Ider, "Prediction of engineering properties of a selected litharenite sandstone from its petrographic characteristics using correlation and multivariate statistical techniques," *Eng. Geol.*, vol. 38, pp. 135–157, 1994.

[10]   A. Shakoor and R. E. Bonelli, "Relationship between petrographic characteristics, engineering index properties, and mechanical properties of selected sandstones," *Bull. Eng. Geol. Environ.*, vol. 28, pp. 55–71, 1991.

[11]   V. S. Vutukuri, R. D. Lama, and S. S. Saluja, *Handbook on Mechanical Properties of Rocks*. Clausthal, Germany: Trans Tech Publications, 1974.

[12]   A. B. Hawkins and B. J. McConnell, "Sensitivity of sandstone strength and deformability to changes in moisture content," *Eng. Geol.*, vol. 25, pp. 115–130, 1992.

[13]   S. Fereshtenejad and J. J. Song, "Fundamental study on applicability of powder-based 3D printer for physical modeling in rock mechanics," *Rock Mech. Rock Eng.*, vol. 49, no. 1–10, 2016.

[14]   A. B. Hawkins, "Aspects of rock strength," *Bull. Eng. Geol. Environ.*, vol. 57, no. 17–30, 1998.

[15]   B. Primkulov, J. Chalaturnyk, R. J. Chalaturnyk, and G. Zambrano Narvaez, "3D Printed Sandstone Strength: Curing of Furfuryl Alcohol Resin-Based Sandstone," *3D Print. Addit.*

Manuf., vol. 4, no. 3, pp. 149–155, 2017.

[16] E. Hoek, "Strength of Jointed Rock Masses," *Géotechnique*, vol. 23, no. 3, pp. 187–223, 1983.

[17] N. R. Barton, "A model study of rock-joint deformation," *Int. J. Rock Mech. Min. Sci.*, vol. 9, no. 5, pp. 579–582, 1972.

[18] P. A. Cundall, Thesis entitled "The Measurement and Analysis of Accelerations in Rock Slopes," University of London, 1971.

[19] O. C. Zienkiewicz, B. Best, C. Dullage, and K. Stagg, "Analysis of Non-linear Problems in Rock Mechanics with Particular Reference to Jointed Rock Systems," in *Proceedings of the Second Congress of the International Society for Rock Mechanics*, Belgrade, September 21 - 26, 1970.

[20] M. A. Mahtab and R. E. Goodman, "Three-dimensional Finite Element Analysis of Jointed Rock Slopes," in *Proceedings of the Second Congress of the International Society for Rock Mechanics*, Belgrade, September 21 - 26, 1970.

[21] R. E. Goodman, R. L. Taylor, and T. A. Brekke, "A model for the mechanics of jointed rock," *J. Soil Mech. Found. Div. Proc. Am. Soc. Civ. Eng.*, vol. 94(SM3), pp. 637–659, 1968.

[22] D. Mas Ivars, M. Pierce, C. Darcel, J. Reyes-Montes, D. Potyondy, R. Young, and P. Cundall, "The synthetic rock mass approach for jointed rock mass modelling," *Int. J. Rock Mech. Min. Sci.*, vol. 48, no. 2, pp. 219–244, 2011.

[23] A. Schultz, "What's the difference between a rock and a rock mass (and why is it important)?" *Abstr. Lunar Planet. Sci. Conf.*, vol. 23, p. 1243, 1992.

[24] B. Stimpson, "Modelling materials for engineering rock mechanics," *Int. J. Rock Mech. Min. Sci.*, vol. 7, no. 1, pp. 77–121, 1970.

[25] E. Fumagalli, "Model Simulation of Rock Mechanics Problems," in *Rock Mechanics in Engineering Practice*, Chapter 11, K. Stagg and O.C. Zienkiewicz, Eds., Wiley, New York, 1968.

[26] S. C. Bandis, A. Lumsden, and N. Barton, "Fundamentals of Rock Joint Deformation.pdf," *Int. J. Rock Mech. Min. Sci. Geomech.*, vol. 20, no. 6, pp. 249–268, 1983.

[27] K. F. Evans, T. Kohl, L. Rybach, and R. J. Hopkirk, "The effects of fracture normal compliance on the long term circulation behaviour of a hot dry rock reservoir: a parameter study using the new fully-coupled code fracture," *Transacations Geotherm. Resour. Counc.*, G. Mata, Eds., vol. 16, pp. 449–456, San Diego, CA, Oct 4 - 7, 1992.

[28] C. Zangerl, K. F. Evans, E. Eberhardt, and S. Loew, "Normal stiffness of fractures in granitic rock: A compilation of laboratory and in-situ experiments," *Int. J. Rock Mech. Min. Sci.*, vol. 45, no. 8, pp. 1500–1507, 2008.

[29] J. Rutqvist, J. Noorishad, C. Tsang, and O. Stephansson, "Determination of fracture storativity in hard rocks using high-pressure injection testing," *Water Resour. Res.*, vol. 34,

no. 10, pp. 2551–2560, 1998.

[30] R. Jung, "Hydraulic in situ investigations of an artificial fracture in the Falkenberg granite," *Int. J. Rock Mech. Min. Sci.*, vol. 26, no. 3–4, pp. 301–308, 1989.

[31] A. Makurat, N. Barton, L. Tunbridge, and G. Vik, "The measurement of the mechanical and hydraulic properties of rock joints at different scales in the Stripa project," in *Proceedings of the International Symposium on Rock Joints*, N. Barton and O. Stephansson, Eds., pp. 541–548, Loen, Norway, June 4 - 6, 1990.

[32] H. R. Pratt, H. S. Swolfs, W. F. Brace, A. D. Black, and J. W. Handin, "Elastic and transport properties of an in-situ jointed granite," *Int J Rock Mech Min Sci*, vol. 14, pp. 34–45, 1977.

[33] J. B. Walsh and M. A. Grosenbaugh, "A new model for analyzing the effect of fractures on compressibility," *J Geophys Res*, vol. 84, no. B7, pp. 3532–3536, 1979.

[34] J. Zhao and E. T. Brown, "Hydro-thermo-mechanical properties of joints in the Carnmenellis Granite," *Q J Eng Geol*, vol. 25, pp. 279–290, 1992.

[35] J. E. Gale, "The effects of fracture type (induced versus natural) on the stress-fracture closure-fracture permeability relationships," in *Proceedings of 23rd US Symposium on Rock Mechanics*, Berkeley, California, pp. 290 - 298, August 25 - 27, 1982.

[36] M. Bart, M. Sibai, and J. F. Shao, "Modelling of hydromechanical behaviour of rock joints under normal stress," in *Proceedings of EUROCK2000,* Aachen, Germany, pp. 591–596.

[37] Z. Sun, C. Gerrad, and O. Stephansson, "Rock joints compliance tests for compression and shear loads," *Int J Rock Mech Min Sci*, vol. 22, no. 4, pp. 197–213, 1985.

[38] P. N. Sundaram, D. J. Watkins, and W. E. Ralph, "Laboratory investigations of coupled stress-deformation-hydraulic flow in a natural rock fracture," in *Proceedings of the 28th US Symposium of Rock Mechanics*, pp. 585 - 592, Tucson, Arizona, June 29 - July 1, 1987.

[39] J. E. Gale, "Comparison of coupled fracture deformation and fluid flow models with direct measurements of fracture pore structure and stress-flow porosities," in *Proceedings of the 28th US Symposium on Rock Mechanics*, pp. 1213–1222, Tucson, Arizona, June 29 - July 1, 1987.

[40] T. W. Schrauf and D. D. Evans, "Laboratory studies of gas flow through a single natural fracture," *Water Resour. Res.*, vol. 22, no. 7, pp. 1038–1050, 1986.

[41] K. G. Raven and J. E. Gale, "Water flow in a natural rock fracture as a function of stress and sample size," *Int. J. Rock. Mech. Min. Sci.*, vol. 22, no. 4, pp. 251–261, 1985.

[42] G. M. Elliott, E. T. Brown, P. I. Boodt, and J. A. Hudson, "Hydromechanical behaviour of joints in the Carnmenellis Granite, S.W. England," in *Proceedings of the International Symposium on Fundamentals of Rock Joints*, pp. 249 - 257, Bjorkliden, Sweden, Sept 15 - 20, 1985.

[43] E. Detournay, "Hydraulic conductivity of closed rock fracture: An experimental and analytical study," in *Proceeding of the 13th Canadian Rock Mechanics Symposium*, pp. 168 - 173, 1980.

[44]   C. Jiang, G. F. Zhao, M. Z. Gao, and Y. X. Zhao, "A trial of 3D printing on rock dynamics," in *Proceedings of the 2nd International Conference on Rock Dynamics and Applications*, H. Li, J. Zhang and J. Zhao, Eds., pp. 123 - 128, Suzhou, China, May 18 - 19, 2016.

[45]   Q. Jiang, X. Feng, L. Song, Y. Gong, H. Zheng, and J. Cui, "Modeling rock specimens through 3D printing: Tentative experiments and prospects," *Acta Mech. Sin.*, vol. 32, no. 1, pp. 101–111, 2016.

[46]   C. Jiang, G. F. Zhao, J. B. Zhu, Y. X. Zhao, and L. Shen, "Investigation of dynamic crack coalescence using a gypsum-like 3D printing material," *Rock Mech. Rock Eng.*, vol. 49, no. 10, pp. 3983–3998, 2016.

[47]   S. Osinga, G. Zambrano-Narvaez, and R. . Chalaturnyk, "Study of geomechanical properties of 3D printed sandstone analogue," in *Proceedings of the 49th US Rock Mechanics / Geomechanics Symposium,* ARMA 15-547, San Francisco, California, June 28 - July 1, 2015.

[48]   J. Rohde and H. Feng, "Analysis of the variability of unconfined compression tests of rock," *Rock Mech. Rock Eng.*, vol. 23, pp. 231–236, 1990.

[49]   Itasca, "PFC 3D Ver 4.0 Manual." Itasca Consulting Group, Inc, Minneapolis, MN.

[50]   S. H. Nguyen, A. I. Chemenda, and J. Ambre, "Influence of the loading conditions on the mechanical response of granular materials as constrained from experimental tests on synthetic rock analoguematerial," *Int. J. Rock Mech. Min. Sci.*, vol. 48, no. 1, pp. 103–115, 2011.

[51]   T. Zhou and J. B. Zhu, "Application of 3D printing and micro-CT scan to rock dynamics," in *Proceedings of the 2nd International Conference on Rock Dynamics and Applications*, H. Li, J. Zhang and J. Zhao, Eds., pp. 247 - 252, Suzhou, China, May 18 - 19, 2016.

[52]   L. Huang, R. R. Stewart, N. Dyaur, and J. Baez-Franceschi, "3D-printed rock models: Elastic properties and the effects of penny-shaped inclusions with fluid substitution," *Geophysics*, vol. 81, no. 6, pp. D669–D677, 2016.

[53]   "Standard Terminology for Additive Manufacturing Technologies," *ASTM F2792-12a*, West Conshohocken, PA*, 2012.

[54]   H. Seitz, W. Rieder, S. Irsen, B. Leukers, and C. Tille, "Three-dimensional printing of porous ceramic scaffolds for bone tissue engineering," *J. Biomed. Mater. Res. - Part B Appl. Biomater.*, vol. 74, no. 2, pp. 782–788, 2005.

[55]   T. Grimm, *User's Guide to Rapid Prototyping*, First. Dearborn, Michigan: Society of Manufacturing Engineers, *Rapid Prototyping Association of SME*, 2004.

[56]   D. Vogler, S. D. C. Walsh, E. Dombrovski, and M. A. Perras, "A comparison of tensile failure in 3D-printed and natural sandstone," *Eng. Geol.*, vol. 226, July 2016, pp. 221 - 235, 2017.

[57]   P. Patirupanusara, W. Suwanpreuk, T. Rubkumintara, and J. Suwanprateeb, "Effect of binder content on the material properties of polymethyl methacrylate fabricated by three dimensional printing technique," *J. Mater. Process. Technol.*, vol. 207, no. 1–3, pp. 40–45,

2008.

[58] R. H. Worden and S. Morad, "Quartz Cementation in Oil Field Sandstones: A Review of the Key Controversies," R.H. Worden and S. Morad, Eds., *in Quartz Cementation in Sandstones: International Association of Sedimentologists Special Publication.*, no. 29, pp. 1–20, Blackwell Science, Oxford, 2000.

[59] S. Boggs, *Principles of Sedimentology and Stratigraphy*, Fourth Edi. New Jersey: Pearson Education Inc., 2006.

[60] J. P. Kruth, L. Froyen, J. Van Vaerenbergh, P. Mercelis, M. Rombouts, and B. Lauwers, "Selective laser melting of iron-based powder," *J. Mater. Process. Technol.*, vol. 149, no. 1–3, pp. 616–622, 2004.

[61] A. Budding, T. H. J. Vaneker, and A. Winnubst, "Open source powder based rapid prototyping machine for ceramics," *Procedia CIRP*, vol. 6, pp. 533–538, 2013.

[62] A. Budding and T. H. J. Vaneker, "New strategies for powder compaction in powder-based rapid prototyping techniques," *Procedia CIRP*, vol. 6, pp. 527–532, 2013.

[63] M. Lanzetta and E. Sachs, "Improved surface finish in 3D printing using bimodal powder distribution," *Rapid Prototyp. J.*, vol. 9, no. 3, pp. 157–166, 2003.

[64] K. Lu, M. Hiser, and W. Wu, "Effect of particle size on three dimensional printed mesh structures," *Powder Technol.*, vol. 192, no. 2, pp. 178–183, 2009.

[65] "Occupational Exposure to Furfuryl Alcohol." U.S. Department of Health, Education and Welfare, p. 71, 1979.

[66] A. Rathi and M. Chanda, "Kinetics of Solution Polymerisation of Furfuryl Alcohol," *Appl. Polym.*, vol. 18, no. 5, pp. 1541–1548, 1974.

[67] E. M. Wewerka, "Investigation of the Polymerization of Furfuryl Alcohol with gel permeation chromatography," *J. Appl. Poly. Sci.*, vol. 12, pp. 1671–1681, 1968.

[68] M. Muthukumar, D. Mohan, and M. Rajendran, "Optimization of mix proportions of mineral aggregates using Box Behnken design of experiments," *Cem. Concr. Compos.*, vol. 25, pp. 751–758, 2003.

[69] A. Gandini, in *Comprehensive Polymer Science,* S. Aggrawal and S. Russo, Eds., Suppl., vol. 1, pp. 527 - 573, Oxford, UK: Pergamon Press, 1992.

[70] A. Gandini and M. Belgacem, "The Polymeric Materials Encyclopedia." CRC Press.

[71] A. Gandini, "The behaviour of furan derivatives in polymerization reactions," *Polym. Chem.*, vol. 25, pp. 47–96, 1977.

[72] M. Choura, N. M. Belgacem, and A. Gandini, "Acid-Catalyzed Polycondensation of Furfuryl Alcohol: Mechanisms of Chromophore Formation and Cross-Linking," *Macromolecules*, vol. 29, pp. 3839–3850, 1996.

[73] W. McKillip, "Chemistry of Furan Polymers," in *ACS Symp. Ser.*, vol. 385, pp. 408–423, 1989.

[74] C. R. Schmitt, "Polyfuryl Alcohol Resins," *Polym.-Plast. Technol. Eng.*, vol. 3, no. 2, p. 121, 1974.

[75] G. E. Maciel, I. S. Chuang, and G. E. Myers, "Carbon-13 NMR study of curing in furfuryl alcohol resins," *Macromolecules*, vol. 17, no. 5, pp. 1087–1090, 1984.

[76] A. Dunlop and F. Peters, *The Furans*. New York, New York: Reinhold Publishing Corp., 1953.

[77] M. Principe, R. Martínez, P. Ortiz, and J. Rieumont, "The polymerization of furfuryl alcohol with p-toluenesulfonic acid: photocross-linkeable feature of the polymer," *Polímeros*, vol. 10, no. 1, pp. 08–14, 2000.

[78] N. Herold, T. Dietrich, W. Grigsby, R. Franich, A. Winkler, B. Buchelt and A. Pfriem, "Effect of Maleic Anhydride Content and Ethanol Dilution on the Polymerization of Furfuryl Alcohol in Wood Veneer Studied by Differential Scanning Calorimetry," *BioResources*, vol. 8, no. 1, pp. 1064–1075, 2013.

[79] S. S. Kelley, R. a. Young, R. M. Rammon, and R. H. Gillespie, "Bond Formation By Wood Surface Reactions Part Iv Analysis of Furfuryl Alcohol, Tannin and Maleic Acid Bridging Agents," *J. Wood Chem. Technol.*, vol. 2, no. 3, pp. 317–342, 1982.

[80] M. Muthukumar and D. Mohan, "Studies on furan polymer concrete," *J. Polym. Res.*, vol. 12, no. 3, pp. 231–241, 2005.

[81] G. K. Solovjov, V. P. Trambovetsky, and D. Kruger, "Furan resin polymer concrete in the Commonwealth of Independent States (CIS)," *ACI Mater. J.*, vol. 91, pp. 158–160, 1994.

[82] N. I. S. Hussein, M. N. Ayof, N. I. M. Sokri, and M. Engineering, "Mechanical Properties and Loss on Ignition of Phenolic and Furan Resin Bonded Sand Casting," vol. 1, no. 3, pp. 223–227, 2013.

[83] M. Vaezi and C. K. Chua, "Effects of layer thickness and binder saturation level parameters on 3D printing process," *Int. J. Adv. Manuf. Technol.*, vol. 53, no. 1–4, pp. 275–284, 2011.

[84] C. B. Gaefke, E. C. Botelho, N. G. Ferreira, and M. C. Rezende, "Effect of Furfuryl Alcohol Addition on the Cure of Furfuryl Alcohol Resin Used in the Glassy Carbon Manufacture," *J. Appl. Polym. Sci.*, vol. 106, no. 2274–2281, 2007.

[85] "Standard Test Methods for Compressive Strength and Elastic Moduli of Intact Rock Core Specimens under Varying States of Stress and Temperatures," *ASTM D7012-14*, pp. 1–9, 2014.

[86] G. Binning, H. Rohrer, C. Gerber, and E. Weibel, "Surface studies by scanning tunneling microscopy," *Phys. Rev. Lett.*, vol. 49, no. 1, pp. 57–61, 1982.

[87] "Scanning Probe Microscopy Training Notebook, Version 3.0" *Digital Instruments Veeco Metrology Group*, 2000.

[88] "Nano and More" Image [Online]. Available: https://www.nanoandmore.com/USA/search.html?list_words=usc, accessed September 10, 2017.

[89] K. M. Mussert, W. P. Vellinga, A. Bakker, and S. van der Zwaag, "A nano-indentation study on the mechanical behaviour of the matrix material in an AA6061 - Al_2O_3 MMC," *J. Mater. Sci.*, vol. 7, pp. 789–794, 2002.

[90] I. N. Sneddon, "The relation between load and penetration in the axisymmetric boussinesq problem for a punch of arbitrary profile," *Int. J. Eng. Sci.*, vol. 3, no. 1, pp. 47–57, 1965.

[91] W. C. Oliver and G. M. Pharr, "An improved technique for determining hardness and elastic modulus using load and displacement sensing indentation experiments," *J. Mater. Res.*, vol. 7, no. 6, pp. 1564–1583, 1992.

[92] B. Tang, a H. W. Ngan, and J. B. Pethica, "A method to quantitatively measure the elastic modulus of materials in nanometer scale using atomic force microscopy.," *Nanotechnology*, vol. 19, no. 49, p. 495713, 2008.

[93] D. Hoffman, "Measuring the Elastic Modulus of Polymers using the Atomic Force Microscope," Michigan Technological University, 2010.

[94] D. Tranchida, S. Piccarolo, and M. Soliman, "Nanoscale mechanical characterization of polymers by AFM nanoindentations: Criticalr approach to the elastic characterization," *Macromolecules*, vol. 39, no. 13, pp. 4547–4556, 2006.

[95] J. Jiang, W. Wang, H. Shen, J. Wang, and J. Cao, "Characterization of silica particles modified with γ-methacryloxypropyltrimethoxysilane," *Appl. Surf. Sci.*, vol. 397, pp. 104–111, 2017.

[96] H. Feng, H. T. N. Le, S. Wang, and M. H. Zhang, "Effects of silanes and silane derivatives on cement hydration and mechanical properties of mortars," *Constr. Build. Mater.*, vol. 129, pp. 48–60, 2016.

[97] "Standard Test Method for Splitting Tensile Strength of Intact Rock Core Specimens", *ASTM D3967-08,* West Conshohocken, PA*, pp. 20–23, 2008.

[98] L. Ma and J. J. K. Daemen, "Strain rate dependent strength and stress-strain characteristics of a welded tuff," *Bull. Eng. Geol. Environ.*, vol. 65, no. 3, pp. 221–230, 2006.

[99] J. R. Rumble, Ed., *CRC Handbook of Chemistry and Physics*, 98th ed. Boca Raton, FL: CRC Press/Taylor & Francis, 2017.

[100] "Standard Test Method for Adhesion or Cohesion Strength of Thermal Spray Coatings", *ASTM C633-13,* West Conshohocken, PA, 2017.

[101] W. A. Deer, R. A. Howie, and J. Zussman, *An Introduction to the Rock Forming Minerals*, 2nd Edition, Longman Scientific & Technical, Essex, UK, 1966.

[102] J. McKillip William, "Chemistry of Furan Polymers," in *Adhesives from Renewable Resources*, 1989, pp. 408–423.

[103] D. R. Lide, *CRC Handbook of Chemistry and Physics*, 86th ed. Boca Raton, FL: CRC Press, Taylor and Francis Group, 2005.

[104] B. Mitchell, "Thingiverse #588985," [Online]. Available: http://www.thingiverse.com/thing:588985, accessed May 10, 2016.

[105] M. Kwasniewski, X. Li, T. Manabu, *True Triaxial Testing of Rocks*, vol. 4 of Geomechanics Research Series, CRC Press, Taylor and Francis Group, 2012.

[106] A. Fakhimi and B. Hemami, "Rock Uniaxial Compression Test and Axial Splitting," *Procedia Eng.*, vol. 191, pp. 623–630, 2017.

[107] W. Voigt, "Ueber die Beziehung zwischen den beiden Elasticitätsconstanten isotroper Körper," *Ann. Phys.*, vol. 274, pp. 573–587, 1889.

[108] A. Reuss, "Berechnung der Fließgrenze von Mischkristallen auf Grund der Plastizitätsbedingung für Einkristalle," *Zeitschrift für Angew. Math. und Mech.*, vol. 9, pp. 49–58, 1929.

[109] S. Nie and C. Basaran, "A micromechanical model for effective elastic properties of particulate composites with imperfect interfacial bonds," *Int. J. Solids Struct.*, vol. 42, pp. 4179–4191, 2005.

[110] J. D. Eshelby, "The Determination of the Elastic Field of an Ellipsoidal Inclusion, and Related Problems," *Proc. R. Soc. A Math. Phys. Eng. Sci.*, vol. 241, no. 1226, pp. 376–396, 1957.

[111] A. Gladkyy and R. Schwarze, "Comparison of different capillary bridge models for application in the discrete element method," *Granul. Matter*, vol. 16, pp. 911–920, 2014.

[112] B. Bhushan and V. N. Koinkar, "Nanoindentation hardness measurements using atomic force microscopy," *Appl. Phys. Lett.*, vol. 64, no. 13, pp. 1653–1655, 1994.

[113] M. Radmacher, M. Fritz, C. M. Kacher, J. P. Cleveland, and P. K. Hansma, "Measuring the viscoelastic properties of human platelets with the atomic force microscope.," *Biophys. J.*, vol. 70, no. 1, pp. 556–67, 1996.

[114] W. C. Oliver, "Measurement of hardness and elastic modulus by instrumented indentation : Advances in understanding and refinements to methodology," *J. Mat. Research,* vol. 19, no. 1, pp. 3 - 20, 2004.

[115] A. C. Fisher-Cripps, *Introduction to Contact Mechanics*, Mechanical Engineering Series, 2nd Edition, Springer Science and Business Media, New York, 2007.

[116] J. L. Meneve, J. F. Smith, N. M. Jennett, and S. R. J. Saunders, "Surface mechanical property testing by depth sensing indentation," *Appl. Surf. Sci.*, vol. 100–101, pp. 64–68, 1996.

[117] N. A. Voronin, "Determining the elastic modulus of a hard coating from the loading curve in indentation," *Russ. Eng. Res.*, vol. 37, no. 2, pp. 97–102, 2017.

[118] J. M. Song, Y. L. Shen, C. W. Su, Y. S. Lai, and Y. T. Chiu, "Strain Rate Dependance on Nanoindentation Responses of Interfacial Intermetallic Compounds in Electronic Solder Joints with Cu and Ag Substrates," *Mater. Trans.*, vol. 50, no. 5, pp. 1231–1234, 2009.

[119] J. Jakes, R. Lakes, and D. Stone, "Broadband nanoindentation of glassy polymers: Part II. Viscoelasticity," *J. Mater. Res.*, vol. 27, no. 2, pp. 475–484, 2012.

[120] "Plastic Test Coupons Instruction Sheet 012-13283B", PASCO Scientific, [Online]: ftp://ftp.pasco.com/Support/Documents/English//AP/AP-8222/012-13283B%20AP-8222%20TXT.pdf, accessed September 15, 2017.

[121] "Torlon 4203 Datasheet", Drake Plastics, [Online]: http://drakeplastics.com/wp-content/uploads/2016/01/Torlon-4203L.pdf, accessed September 15, 2017.

[122] "Ketaspire Design Guide - PEEK", Drake Plastics, [Online]: http://drakeplastics.com/wp-content/uploads/2015/09/Ketaspire-Design-Guide.pdf, p. 7, accessed September 15, 2017.

[123] M. Dargahi, "Instrumented Indentation Testing," Service Contract Report from Anton-Paar, Montreal, Quebec, 2017.

[124] E. P. Plueddemann, *Silane Coupling Agents*, Chapter 1 "General Concepts", pp. 1 - 29, Springer, New York, New York, 1982.

[125] S. Amziane, V. Nozahic, and M. Sonebi, "Water Absoprtion of Plant Aggregate," in *Bio-aggregates Based Building Materails: State-of-the-Art of the RILEM Technical Committee 236-BBM*, S. Amziane and F. Collet, Eds. Dordrecht, Netherlands, p. 74, 2017.

[126] A. Basu, D. A. Mishra, and K. Roychowdhury, "Rock failure modes under uniaxial compression, Brazilian, and point load tests," *Bull. Eng. Geol. Environ.*, vol. 72, no. 3–4, pp. 457–475, 2013.

[127] D. O. Potyondy and P. a. Cundall, "A bonded-particle model for rock," *Int. J. Rock Mech. Min. Sci.*, vol. 41, no. 8 SPEC.ISS., pp. 1329–1364, 2004.

[128] P. H. S. W. Kulatilake, B. Malama, and J. Wang, "Physical and particle flow modeling of jointed rock block behavior under uniaxial loading," *Int. J. Rock Mech. Min. Sci.*, vol. 38, no. 5, pp. 641–657, 2001.

[129] T. Kazerani and J. Zhao, "Micromechanical parameters in bonded particle method for modelling of brittle material failure," *Interntional J. Numer. Anal. Methods Geomech.*, vol. 34, pp. 1877–1895, 2010.

[130] A. Lisjak, D. Figi, and G. Grasselli, "A review of discrete modeling techniques for fracturing processes in discontinuous rock masses," *J. Rock Mech. Geotech. Eng.*, vol. 6, pp. 301–314, 2014.

[131] N. Cho, C. D. Martin, and D. C. Sego, "A clumped particle model for rock," *Int. J. Rock Mech. Min. Sci.*, vol. 44, no. 7, pp. 997–1010, 2007.

[132] F. H. Kulhawy, "Stress deformation properties of rock and rock discontinuities," *Eng. Geol.*, vol. 9, no. 4, pp. 327–350, 1975.

[133] R. S. Rosso, "A comparison of joint stiffness measurements in direct shear triaxial compression, and In Situ," *Int. J. Rock Mech. Min. Sci. Geom. Abs.*, vol. 13, no. 6, pp. 167 - 172, 1976.

[134] G. Rong, G. Liu, D. Hou, and C.B. Zhou, "Effect of particle shape on mechanical behaviors of rocks: a numerical study using clumped particle model," *Scientific World Journal*, vol. 2013, p. 1 - 12, 2013.

[135] X. Ding, L. Zhang, H. Zhu, and Q. Zhang, "Effect of Model Scale and Particle Size Distribution on PFC3D Simulation Results," *Rock Mech. Rock Eng.*, vol. 47, no. 6, pp. 2139–2156, 2014.

[136] S. Q. Yang, Y. H. Huang, H. W. Jing, and X. R. Liu, "Discrete element modeling on fracture coalescence behavior of red sandstone containing two unparallel fissures under uniaxial compression," *Eng. Geol.*, vol. 178, pp. 28–48, 2014.

[137] Y. Zhou, S. C. Wu, W. Q. Wang, and J. F. Ding, "Research on meso mechanical parameters determining method of rock-soil material," in *Rock Mechanics: Achievements and Ambitions*, M. Cai, Ed. New York, New York, pp. 597–600, 2012.

Appendix

A-1 T-test of Young's Moduli from UCS Testing
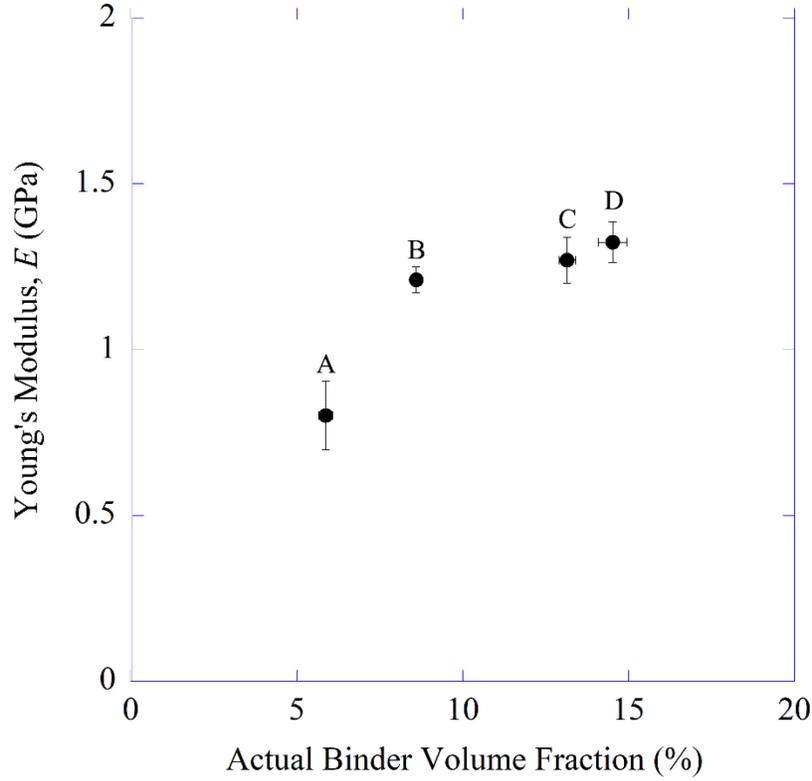
Figure A-1.1: Young's modulus, E, of 3D-printed sandstone versus actual binder volume fraction. $N = 9$ for 6 vol. %, $N = 19$ for 8 vol. %, $N = 20$ for 13 vol. % and $N = 19$ for 15 vol. %.

A two tail t-test was performed on the data set using:

$$t = \frac{\mu_1 - \mu_2}{\sqrt{\frac{\sigma_1^2}{N_1} + \frac{\sigma_2^2}{N_2}}} \qquad (19)$$

$$DOF = (N_1 - 1) + (N_2 - 1) \qquad (20)$$

where μ_i is the mean value of Young's modulus, σ_i is the standard deviation and N_i is the number of samples in the data set. The results of the t-test are shown below in Table A-3.1.

Table A-1.1: Data from two tail t-tests performed on the data from Figure A-3:1, where as binder volume fraction is increased, the probability that the Young's modulus is the same within 99 % becomes more likely.

Young's Modulus (GPa)	Standard Deviation (GPa)	Sample Size	DOF	t	t_{crit} ($\alpha = 0.01$)
A 0.81 B 1.21	A 0.104 B 0.039	9 19	26	11.42	2.78
B 1.21 C 1.27	B 0.039 C 0.069	19 20	37	3.36	2.70
C 1.27 D 1.32	C 0.069 D 0.061	20 18	36	2.36	2.78

A-2 Determination of E_r

For PMMA

$$\frac{1}{E_r} = \frac{(1 - v^2)}{E} + \frac{(1 - v_i^2)}{E_i}$$

$$\frac{1}{E_r} = \frac{(1 - (0.37)^2)}{3\ GPa} + \frac{(1 - (0.17)^2)}{137\ GPa}$$

$$\frac{1}{E_r} = 0.297$$

$$E_r = 3.37\ GPa$$

For indium

$$\frac{1}{E_r} = \frac{(1 - v^2)}{E} + \frac{(1 - v_i^2)}{E_i}$$

$$\frac{1}{E_r} = \frac{(1 - (0.45)^2)}{9.2\ GPa} + \frac{(1 - (0.17)^2)}{137\ GPa}$$

$$\frac{1}{E_r} = 0.0938$$

$$E_r = 10.7\ GPa$$

A-3 Determination of A and α

$$\text{Since } K = A\left(1 + \frac{\alpha}{E_r}\right)$$

$$E_r = \frac{\alpha}{\frac{K}{A} - 1}$$

$$\frac{E_r K}{A} - E_r = \alpha$$

Since $\alpha_{PMMA} = \alpha_{INDIUM}$

$$\frac{E_{r(PMMA)} K_{PMMA}}{A} - E_{r(PMMA)} = \frac{E_{r(INDIUM)} K_{INDIUM}}{A} - E_{r(INDIUM)}$$

$$\frac{(3.37\ GPa)(68.79\frac{V}{\mu m})}{A} - 3.37\ GPa = \frac{(10.7\ GPa)\left(55.95\frac{V}{\mu m}\right)}{A} - 10.7\ GPa$$

$$10.7\ GPa - 3.37\ GPa = \frac{(10.7\ GPa)\left(55.95\frac{V}{\mu m}\right)}{A} - \frac{(3.37\ GPa)(68.79\frac{V}{\mu m})}{A}$$

$$7.29\ GPa = \frac{\left(364.59\frac{GPa * V}{\mu m}\right)}{A}$$

$$A = 50.0\frac{V}{\mu m}$$

$$\frac{E_{r(PMMA)} K_{PMMA}}{A} - E_{r(PMMA)} = \alpha$$

$$\frac{(3.37\ GPa)\left(68.79\frac{V}{\mu m}\right)}{50.0\frac{V}{\mu m}} - 3.37\ GPa = \alpha$$

$$\alpha = 1.27\ GPa$$

A-4   PFC³ᴰ Additional Theory and Calibration Procedure

In PFC³ᴰ, many properties must be stipulated in order to accurately describe the mechanical behaviour of a rock mass. Normal stiffness, k_n, and shear stiffness, k_s, are defined in PFC³ᴰ as follows:

$$k_n := \begin{cases} 2tE_c, t = 1 & PFC^{2D}, \\ 4RE_c & PFC^{3D}, \end{cases} \tag{21}$$

$$k_s := \frac{k_n}{\left(\frac{k_n}{k_s}\right)} \tag{22}$$

$$k^{-n} := \frac{\bar{E}_c}{R^{(A)} + R^{(B)}} \tag{23}$$

$$k^{-s} := \frac{k^{-n}}{\left(\frac{k^{-n}}{k^{-s}}\right)} \tag{24}$$

where E_c and $\bar{E}_c$, are the Young's moduli of the grains and cement, respectively; R is the particle radius; and (k_n/k_s) and (k^{-n}/k^{-s}) are the ratios of normal to shear stiffness of the grains and cement, respectively [127].

Figure A-4.1 shows the placement of particles when using Eqs. 17- 20, above. However, due to the 3D-printed sandstone being adhered strictly through binder, there are no contact bonds in any simulations and there is usually a thickness or length associated with the joint (see Figure 4.3.2). Therefore, any PFC³ᴰ simulations for this thesis dealt strictly with parallel bonds. As a summation, Figure A-4.2 contains a flow chart showing the calibration procedure outlined by Itasca [49].

$$E_c = \begin{cases} \dfrac{k_n}{2t}, & t = 1, \ \text{PFC2D} \\[2ex] \dfrac{k_n}{2L} = \dfrac{k_n}{4R}, & \text{PFC3D} \end{cases}$$

grain behavior

$$\bar{E}_c = \bar{k}^n \left(R^{(A)} + R^{(B)} \right)$$

cement behavior
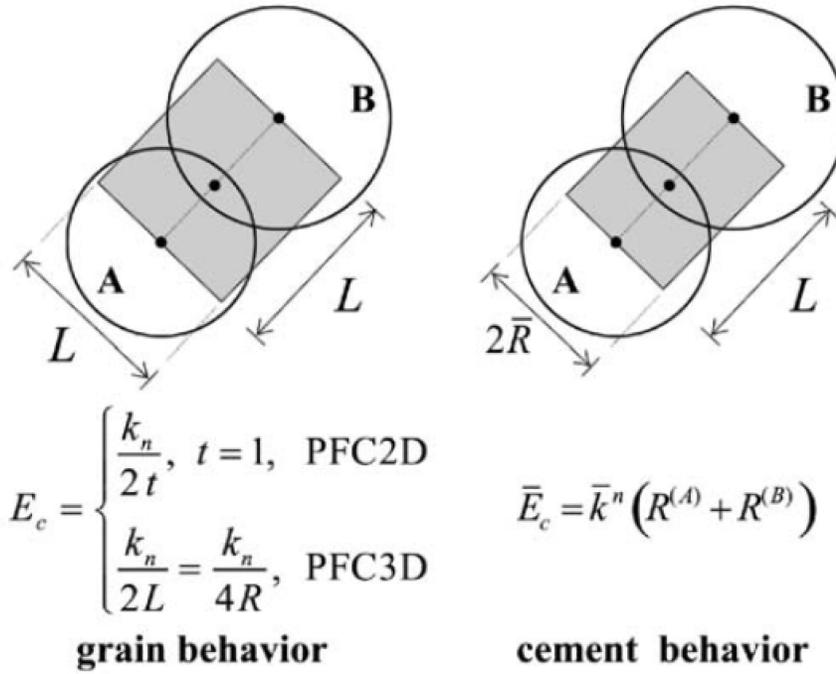
Figure A-4.1: Equivalent continuum material of a grain-cement system used in PFC^{3D}. Figure reprinted with permission from Potyondy et al. [127] © 2017 Elsevier.

Match the Young's Modulus by setting the material strengths to a large value (forcing the model material to behave elastically)

Vary E_c and $\bar{E}_c$ until Young's Modulus of the model is accurate

Match Poisson's Ratio by varying k_n/ks (and $\bar{k}_n/\bar{k}_s$ for a parallel-bonded material)

Calculate k_n and $\bar{k}_n$ by Eqs. 11 and 13 and the calibrated E_c and $\bar{E}_c$ values.

Divide k_n and $\bar{k}_n$ by k_n/ks and $\bar{k}_n/\bar{k}_s$ to determine k_s and $\bar{k}_s$, respectively.

Figure A-4.2: Calibration procedure outlined by Itasca [49] for use in PFC^{3D}